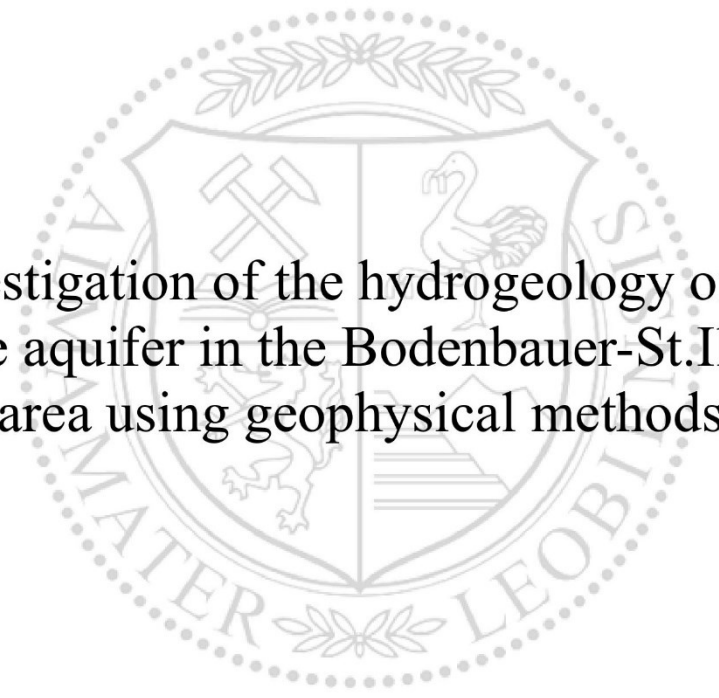




Chair of Energy Geosciences

Master's Thesis



Investigation of the hydrogeology of the
pore aquifer in the Bodenbauer-St. Ilgen
area using geophysical methods

Patrick Fachthaler, BSc

April 2024



MONTANUNIVERSITÄT LEOBEN
www.unileoben.ac.at

EIDESSTÄTTLICHE ERKLÄRUNG

Ich erkläre an Eides statt, dass ich diese Arbeit selbstständig verfasst, andere als die angegebenen Quellen und Hilfsmittel nicht benutzt, den Einsatz von generativen Methoden und Modellen der künstlichen Intelligenz vollständig und wahrheitsgetreu ausgewiesen habe, und mich auch sonst keiner unerlaubten Hilfsmittel bedient habe.

Ich erkläre, dass ich den Satzungsteil „Gute wissenschaftliche Praxis“ der Montanuniversität Leoben gelesen, verstanden und befolgt habe.

Weiters erkläre ich, dass die elektronische und gedruckte Version der eingereichten wissenschaftlichen Abschlussarbeit formal und inhaltlich identisch sind.

Datum 18.04.2024

Unterschrift Verfasser/in
Patrick Fachathaler

Acknowledgment

I would like to take this opportunity to thank all those who have contributed to the success of this thesis.

First and foremost, I would like to thank Univ.-Prof. Dipl.-Ing. Dr. mont. David Misch, who showed a great deal of patience during the thesis and helped with both technical knowledge as well as support during the fieldwork.

I would also like to thank Ao.Univ.-Prof. Dr.phil. Robert Scholger, who always had an open ear for me with his immense expertise, not only during the measurements, but also during the processing and interpretation of the data.

Furthermore, my thanks go to the ZWHS for the smooth cooperation, which was demonstrated both in the permitted use of their land and in the exchange of information.

In addition, many thanks to Dr. Chi Zhang, Dr. Michael Behm and Dr. David Kusnirak, who provided both equipment and active support during the measurements.

Finally, my biggest thanks go to my family, especially my mom Michaela, who supported me in every decision and made it possible for me to study at the University of Leoben and a heartfelt thanks to my girlfriend Nicole, who was always there for me during this important chapter of my life.

Abstract

The pore aquifer in the Bodenbauer-St. Ilgen area on the southern side of the Hochschwab Massif is of great significance for the water supply of the city of Graz and its neighboring municipalities. Hydrogeological investigations on the southern Hochschwab side in the 1970s and 1980s raised public interest in the potential of the water seeping into the subsoil in this area for the first time. The establishment of the Wasserverband Hochschwab Süd, nowadays known as the Zentral-Wasserversorgung Hochschwab Süd (ZWHS), laid the foundation for the development and utilization of this catchment area. Today, around 6.2 million m³/a, which correspond to around 195 l/s, are consumed by the surrounding communities. These hydrogeological investigations were carried out more than 40 years ago, which has increased the demand for further examination. The aim of this study was to identify the groundwater-bearing layers (Aquifer) in the Bodenbauer-St. Ilgen area, as well as the level of the groundwater table and the depth of the pre-Quaternary bedrock. Initially, two profiles were measured using geoelectrical resistivity tomography (ERT) during this thesis, which were later supplemented by two vertical electrical sounding (VES) profiles. The former profiles, designed to detect the water-bearing horizons in the Bodenbauer area, were positioned close to the seismic survey shot in the 1970s in order to ensure the best possible comparability. The results of the ERT verify the historical data along the first profile (hs01), as both a layered subsurface structure and an aquifer were detected. An answer to the previously unresolved question of a possible aquifer was found for profile hs02, which runs perpendicular to hs01, as the high resistivities indicate the presence of dry sediments and therefore not water-bearing layers. The depth soundings, positioned along the ERT profiles, were intended to determine the depth of the pre-Quaternary bedrock, but did not lead to the desired result, partly due to topographical constraints. The depth of the basin bedrock could not be determined either by the ERT or the VES for profile hs01. In the case of hs02, however, the possibility remains that the pre-Quaternary basement can be encountered at a depth of 100 m, due to the steeply dipping flanks. The results of these measurement campaigns generally agree well with those of the former investigations and can also answer previously unresolved questions, such as the presence and the distribution of groundwater-bearing layers.

Zusammenfassung

Die Landeshauptstadt Graz, sowie umliegende Gemeinden, beziehen einen Großteil ihres Wasserbedarfs vor allem von der Südseite des Hochschwabs und somit aus dem Porenaquifer im Bereich Bodenbauer-St. Ilgen. Aufgrund hydrogeologischer Untersuchungen auf der südlichen Hochschwabseite in den 1970er und 1980er Jahren wurde das Potential der dort in den Untergrund versickernden Wässer das erste Mal in das öffentliche Interesse gerückt. Mit der Gründung des Wasserverbandes Hochschwab Süd, heutzutage bekannt als Zentral-Wasserversorgung Hochschwab Süd (ZWHS), wurde der Grundstein für die Erschließung und Nutzung dieses Einzugsgebietes gelegt. Heute werden rund 6.2 Mio. m³/a, dies entspricht in etwa 195 l/s, von den umliegenden Gemeinden verbraucht. Diese durchgeführten hydrogeologischen Untersuchungen, welche sich hervorragend für Ergebnisvergleiche eignen, liegen bereits mehr als 40 Jahre zurück, wodurch der Bedarf an weiteren Untersuchungen drastisch an Relevanz gewonnen hat. Ziel dieser Studie war es, die grundwasserführenden Schichten (Aquifer) im Gebiet Bodenbauer-St. Ilgen, die Höhe des Grundwasserspiegels, als auch die Tiefe des prä-Quartären Grundgebirges zu ermitteln. Zunächst wurden im Zuge dieser Arbeit zwei Profile mittels Geoelektrischer Widerstandstomographie (ERT) gemessen, welche im Anschluss um zwei Tiefensondierungen (VES) ergänzt wurden. Die ersten beiden Profile, deren Ziel die Detektion der wasserführenden Horizonte im Bereich Bodenbauer war, wurden in der Nähe, der in den 1970er Jahren geschossenen Seismik positioniert, um eine möglichst gute Komparabilität mit dieser zu gewährleisten. Die Ergebnisse der ERT bestätigen die historischen Daten entlang des ersten Profils (hs01), da sowohl ein geschichteter Aufbau des Untergrundes als auch ein Aquifer in der Tiefe detektiert werden konnten. Für das Profil hs02, welches normal zu hs01 verläuft, wurde eine Antwort auf die bisher ungelöste Frage eines möglichen Aquifers gefunden, da es sich aufgrund der hohen gemessenen Widerstände um trockene Sedimente und nicht um wasserführende Schichten handelt. Die Tiefensondierungen, positioniert entlang der ERT-Profile, sollten die Ermittlung des prä-Quartären Beckenuntergrundes ermöglichen, führten jedoch, zum Teil aufgrund von topographischen Beschränkungen, nicht zu dem gewünschten Resultat. Die Tiefe des Beckenuntergrundes konnte sowohl durch die ERT als auch durch die Tiefensondierung für das Profil hs01 nicht ermittelt werden, wohingegen für hs02 die Möglichkeit besteht, dass der prä-Quartäre Untergrund, aufgrund der steil einfallenden Flanken, in einer Tiefe von 100 m anzutreffen ist. Die gewonnenen Ergebnisse dieser Messkampagnen stimmen im Allgemeinen gut mit jenen der bisherigen Untersuchungen überein und können zusätzlich bisher noch ungelöste Fragestellungen, wie das Vorhandensein und die Verteilung grundwasserführender Schichten beantworten.

Table of Contents

Acknowledgment	I
Abstract	II
Zusammenfassung.....	III
1. Introduction	1
2. Location of the study area	3
3. Geology	4
3.1. Juvavian nappes system.....	5
3.1.1. Mürzalpen nappe.....	5
3.2. Basin history.....	5
4. Hydrogeological setting of the Hochschwab Massif	7
4.1. Hydrogeology at the southern margin.....	7
4.2. Hydrogeology at the northern margin.....	8
5. Historical data of the survey area.....	11
5.1. Hydrogeological mapping	11
5.2. Existing boreholes.....	12
5.3. Groundwater monitoring.....	15
5.4. Geoelectric survey	16
5.5. Seismic survey.....	18
6. Measuring procedure and methods	21
6.1. Basic principles.....	21
6.2. Electrical properties of the natural environment.....	22
6.3. Electrical Resistivity Tomography (ERT).....	23
6.3.1. Data Acquisition Systems.....	23
6.3.2. Measurement of resistivity and apparent resistivity	24
6.3.3. Pseudosections.....	25
6.3.4. Array Configurations	26
6.3.5. Array Comparison.....	31
6.4. Vertical Electrical Sounding (VES)	36
6.5. Global Navigation Satellite System (GNSS)	37
7. Inversion.....	38
7.1. Inversion software	39
7.2.1. Res2DInv	39

7.2.2. Res1D.....	39
8. Geographic Information System (GIS)	40
8.1. Quantum GIS (QGIS).....	40
9. Fieldwork and Data Processing.....	41
9.1. Permissions	41
9.2. Measurement conditions.....	42
9.3. Measurement devices	42
9.3.1. ERT device	42
9.3.2. VES device	43
9.4. Measurement setup and procedure.....	43
9.4.1. Electrical Resistivity Tomography (ERT).....	43
9.4.2. Vertical electrical sounding (VES).....	44
9.4.3. Topographical measurement.....	45
9.4.3. Profiles	45
9.5. Data Processing.....	47
9.5.1. ERT Data Processing.....	47
9.5.2. VES Data Processing	52
10. Results.....	54
10.1. Inversion - ERT	54
10.2. Hs01.....	56
10.3. Hs02.....	61
10.4. Inversion - VES	64
10.5. Hs01ves	65
10.6. Hs02ves	66
11. Discussion.....	68
11.1. Hs02 and groundwater-related borehole information.....	68
11.2. Hs01 (2022) and refraction seismic data (1971).....	69
11.3. Hs02 (2022) and refraction seismic data (1971).....	71
12. Summary and Conclusions	73
13. Outlook	75
14. References.....	76
15. Appendix	80
15.1. Refraction seismic	80
15.1.1. Line 1.....	80

15.1.2. Line 3.....	81
15.2. ERT.....	82
15.2.1. Apparent resistivity histograms.....	82
15.3. Vertical Electrical Sounding.....	84
15.3.1. Hs01ves.....	84
15.3.2. Hs02ves.....	85
15.4. Orthophotography.....	86
15.5. ERT Results.....	87
15.5.1. Dipole-Dipole array for hs01.....	87
15.5.2. Dipole-Dipole array for hs01 with the implementation of a fixed resistivity region....	87
15.5.3. Multiple Gradient array for hs01.....	88
15.5.4. Dipole-Dipole array for hs02.....	88
15.5.5. Combination of Dipole-Dipole and Pole-Dipole for hs01.....	89
15.5.6. Combination of Dipole-Dipole and Pole-Dipole for hs02.....	89

1. Introduction

Historically, water has always been one of the most important and "valuable" resources worldwide and even in times of climate change, new and constantly changing challenges arise with regard to demand, utilization and the necessary protection against contamination. Austria occupies a special position regarding water as a raw material, as there is still enough available despite the increasing demand in recent decades. The construction of the 2nd Vienna High Spring Pipeline dates back over 100 years (1910), clearly demonstrating the importance of the Hochschwab Massif in terms of water management. The karst waters from the northern part are relevant for the water supply of the city of Vienna, however, this is not the case for the city of Graz and neighboring municipalities, for which the southern side and thus the pore aquifer in the Bodenbauer-St. Ilgen area is of immense importance (Fabiani, 1980). It took another 50 years for the southern Hochschwab valleys to gain relevance, however, with more than 6 million cubic meters of drinking water per year, the region is indispensable for the surrounding towns (ZWHS, 2023).

Therefore, hydrogeological research, which is a specialized discipline at the intersection of the geological and hydrological sciences should be conducted regularly (Stadler and Benischke, 2009). To achieve a comprehensive understanding of the interaction between the geological substrate and the entire water cycle combining various sub-disciplines is vital. These include climatological-meteorological, geomorphological, in the Hochschwab mainly karst morphological, as well as pedological, hydrochemical, hydrobiological and vegetational aspects (Stadler and Benischke, 2009), but also geophysical methods, such as geoelectric, improve the understanding. The electrical resistivity, together with its reciprocal, the electrical conductivity, depend on a variety of influential variables, including water content, temperature, salinity, and mineralogy, such as clay mineral content. Based on these dependencies and the non-invasive or minimal intrusive character, geoelectric techniques such as Electrical Resistivity Tomography (ERT) are exceptionally well suited for hydrogeological applications (Revil et al., 2012). These include water level estimation, detection of hydrogeologic pathways, water content, water quality, salinity, and possible water contamination (Revil et al., 2012). ERT is a direct-current (DC) resistivity method capable of depicting physical properties of the subsurface by generating pulses using artificial sources (Revil et al., 2012; Dentith and Mudge, 2014).

The last measurements in the Buchberg-St. Ilgen area can be dated back for more than 50 years, resulting in an interest in and a need for more recent and up-to-date data sets. The height of the groundwater table in the vicinity of the Bodenbauer restaurant was detected at a depth of around 60 m based on the borehole data from the measurement campaign in the 1970s. During the winter

months, the groundwater level cannot be recorded. At the Zentral-Wasserversorgung Hochschwab Süd (ZWHS) headquarters, however, it is much better to monitor the groundwater, because the fluctuations in the water level can be measured throughout the year and the effects of snowmelt and other extreme weather events can be taken into account. The bedrock at borehole 1 (BI 1) near the Bodenbauer restaurant was initially expected at a depth of 60 m, however, this could not be verified based on the drilling data. At borehole 2 (BI 2) near the ZWHS, an increase in the Werfen Shales as part of the basin fill was observed at a depth of 100 m, although the actual pre-Quaternary bedrock was first detected at 202 m depth. Therefore, geoelectrical measurement methods, such as ERT, were used during this thesis to investigate the presence of groundwater-bearing layers and the associated question of the height of the groundwater table along two profiles. Furthermore, an attempt was made to determine the depth of the pre-Quaternary bedrock. For this purpose, two depth soundings were conducted along both profiles to enable a correlation between the ERT and the results of the VES. Additionally, a further motivation of this thesis was to process the historical data and compare it with the newly acquired results using modern measurement methods and to eliminate any possible inconsistencies or uncertainties.

2. Location of the study area

The study area is in the northernmost part of the province of Styria (Figure 1a), exactly located on the southern side of the Hochschwab mountain range. The Hochschwab Massif in general is best known for the water supply of the city of Vienna, but the significance of the drainage in the south is rather unknown. The Bodenbauer restaurant, acting as the starting point (Figure 1b), as well as the surrounding pasture and forest areas, owned either by the Central Water Supply Hochschwab - South (ZWHS) or the Pension Insurance Institution (PVA), are the investigation sites for the measurements.

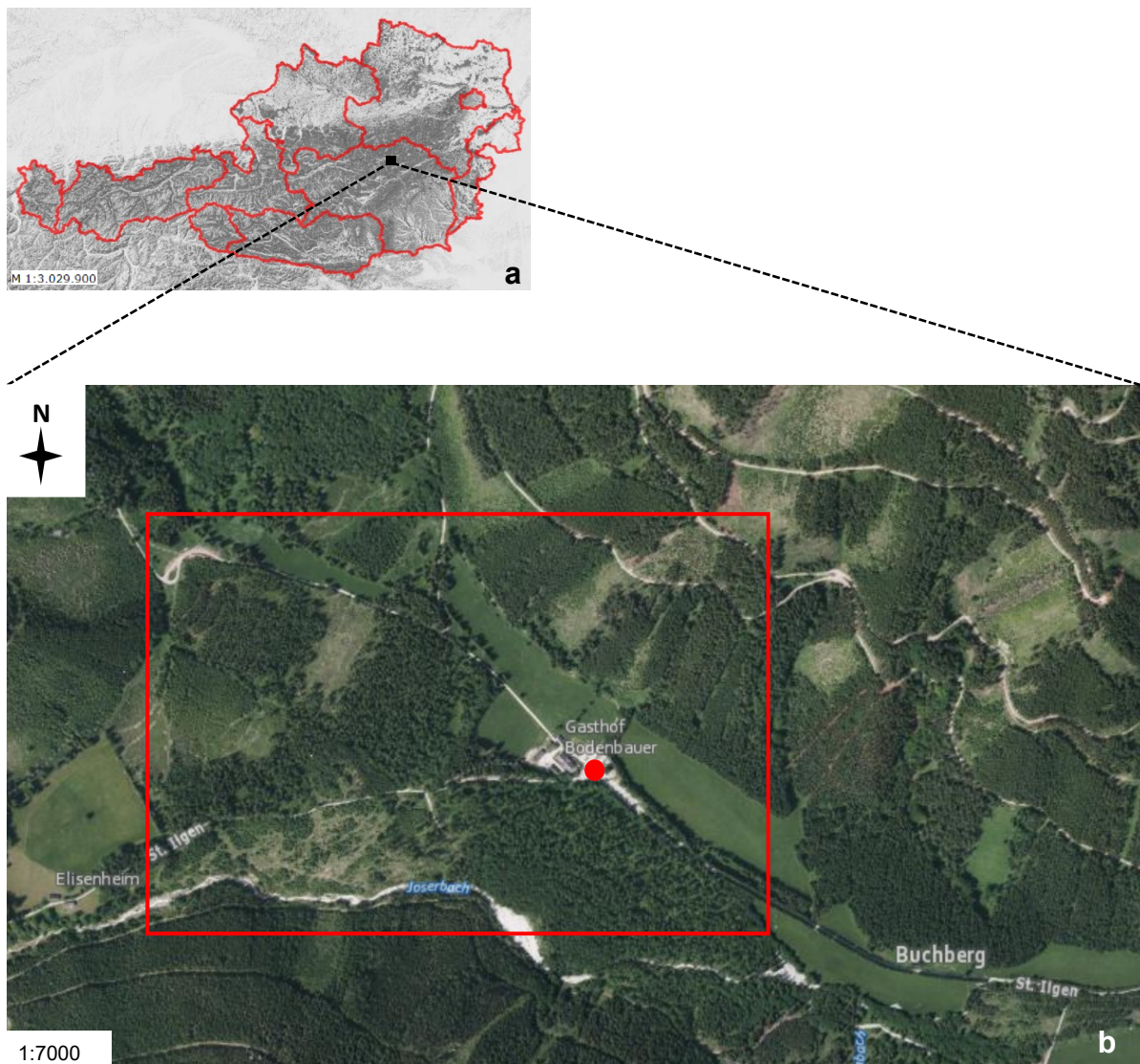


Figure 1: (a) Map of Austria https://www.geoland.at/webgisviewer/geoland/map/Geoland_Viewwer/Geoland 03.11.2022. (b) Orthophotography of the survey area. The red circle marks the Bodenbauer restaurant (WGS84 UTM 33N [m] – Northing: 5269600; Easting: 508500). The survey area is indicated by red rectangle <https://gis.stmk.gv.at/wgportal/atlasmobile/map/Basiskarten/Basiskarte> 03.11.2022.

3. Geology

The Upper Austroalpine forms the tectonically highest unit of the Eastern Alpine and consists of six nappes systems, one of them being the Northern Calcareous Alps (Schmid et al., 2004). These form a fold and thrust belt with predominantly east-west trending fold axes. The tectonic subdivision from the footwall to the hanging wall is divided into the Bajuavian nappes, the Tyrolian nappes, and the Juvavian nappes (Bryda et al., 2013), with the measurement area located in the latter. The tectonically highest of these units, the Juvavian, is exclusively represented by the Mürzalpen nappe in the map sheet 102 Aflenz - Kurort (Figure 2) (Kristan-Tollmann and Tollmann, 1962). The Juvavian nappes system is beside the Werfen Shales as a base, comprised of three Triassic-formed, thick carbonate platforms (Gutensteiner dolomite, Steinalm- and Wetterstein-limestone/dolomite and Dachstein carbonate platform) (Missoni and Gawlick, 2011a). The Juvavian blanket structure was deformed during the subsequent Eoalpine and Mesoalpine orogeny and was finally reactivated by the extrusion of the Eastern Alpine units into the Pannonian region from the Upper Paleogene to the lower Miocene (Linzer et al., 2002).

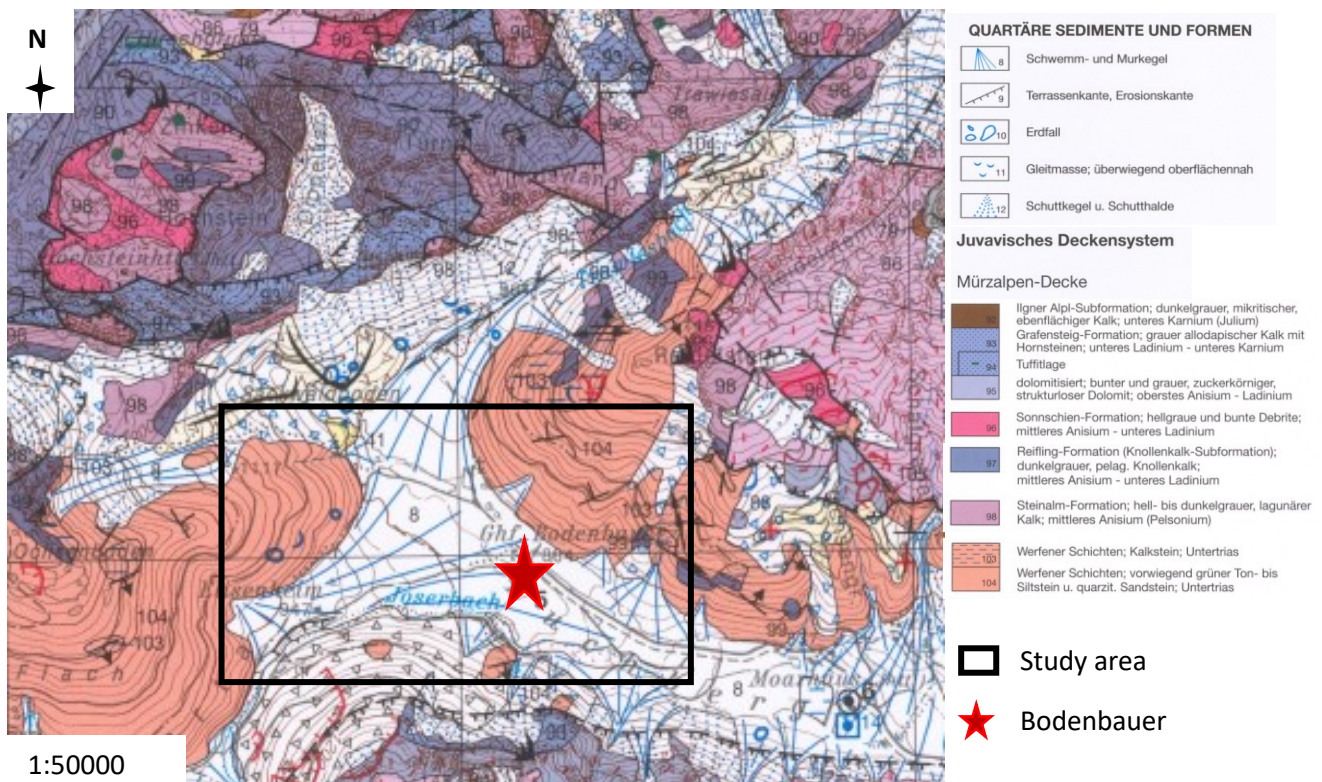


Figure 2: Detailed section of the geological map relevant to the survey (Number 102 - Aflenz Kurort) The survey area is framed by a black rectangle containing the Bodenbauer restaurant, the orientation point for the measurements, which is marked by a red star. (modified after the Geological Survey of Austria, 2023).

3.1. Juvavian nappes system

The tectonically highest floor in the Northern Calcareous Alps differs from the underlying Tirolian nappes by an intensive thermal overprinting and metamorphism, which probably occurred already before the Upper Jurassic (Gawlick et al., 1994a).

3.1.1. Mürzalpen nappe

The Mürzalpen nappe, tectonically the highest unit of the map sheet, was thrust onto the Tirolikum in the Upper Jurassic. The massive carbonate platforms, formed as deposits in the Middle and Upper Triassic, were subjected to tectonic and climatically (sea level fluctuations) induced interruptions during their formation (Bryda et al., 2013). Simultaneously with the 1000 m thick Steinalm and Wetterstein limestones, slope, and basin sediments were deposited. The rocks of the Gutenstein Formation are tectonically located beneath the Steinalm-Wettersteinkalk Formation, with the former being in the hanging wall of the Werfen Shales (Bryda et al., 2013). The Werfen strata, formed during the Middle Triassic, is the geologically oldest part and dips shallowly to the north below the Wetterstein limestones of the main Hochschwab ridge (Decker and Reiter, 2001).

3.2. Basin history

The Hochschwab Massif experienced massive effects on its shape, and hydrogeological and morphological aspects during the last ice age (Würm glaciation). Due to a drop in the snowline, glaciation started already below 1400 m, and mighty valley glaciers formed especially on the southern side of the Massif (Fabiani et al., 1980). The Buchberg-St. Ilgen area extends over 44.8 km², of which about 40 % (~ 17.8 km²) are 1400 m above sea level (ZWHS, 2023). Moraine slopes and moraine bends, as well as tongue basins, characterize the glacier ends (Fabiani et al., 1980). Relevant to the study area is the glacial over-deepening of the valleys. The striking transition between plateaus and valleys allowed the glaciers to expand almost unimpeded, resulting in a tremendous scouring force. The maximum over-deepening of the valleys occurred in areas where the softer, less resistant Werfen Shales are exposed (Fabiani et al., 1980). The southern side of the Hochschwab syncline is characterized by an alternating sequence of U-shaped basins (Buchberg region) and tongue basins (St. Ilgen-Innerzwain area). These deep valleys are partly below the pre-flood level or the karst water level. Loose sediment thicknesses of up to 200 m are present in these erosional basins. They represent excellent pore aquifers with high storativity. More homogeneous water pathways are existent, as well as a corresponding good filtering effect of the penetrating karst water due to the pore aquifer behavior (Fabiani, 1980; Fabiani et al., 1980). Due to the steep dipping of the walls after the retreat of the glaciers, as well as the formation of

alluvial cones as a result of landslides blocking the valley, all surface waters are forced to percolate and, consequently, an enrichment of the groundwater occurs (Fabiani, 1980). Sediment permeability decreases with depth, reducing the pore space relevant for storage volume (Fabiani et al., 1980). The Buchberg basin covers an area of 2 km², as well as a cubature of loose material of up to 300 million m³. In the Buchberg area, the loose sediment fill reaches an extension in width of up to 500 m and a thickness of up to 200 m. However, the thickness decreases to as little as 20 m due to the harder valley bed during the formation of the basin towards the valley entrance. The sedimentary materials in the Buchberg basin are alternating sequences of coarse clastic and fine clastic calcareous sediments (Fabiani, 1980).

4. Hydrogeological setting of the Hochschwab Massif

A comprehensive spring survey covering the whole Hochschwab Massif was conducted in the summer of 1960. A total of 380 spring discharges underwent study, of which 235 discharges had their electrical conductivity, as a parameter for overall mineralization, and the water temperature, determined, as well as the flow rate which was either estimated or measured (Stadler and Benischke, 2009).

4.1. Hydrogeology at the southern margin

In the south, the hydrological situation is characterized by the following three groups of rocks in terms of water flow and water balance. Heavily fissured limestones and dolomites enable rapid infiltration and drainage of rainwater. The eastern part of the study area is characterized by dolomites, whereas in the north and in the west, around the Sackwaldboden and the Trawies Valley, limestones are increasingly responsible for the infiltration and drainage of precipitation water (Meidl et al., 1980). Quaternary debris deposits of different grain sizes act as effective pore aquifers due to their considerable thickness. Strong groundwater level fluctuations are subject to the influence of precipitation and karst waters (Bauer, 2010). Werfen Shales, which occur as a largely impermeable aquitard/aquiclude, serve as a dewatering subsoil. The yield of the individual springs in the St. Ilgen Valley can be classified as low, based on several spring surveys, as most of them, if measurable, percolate away at the latest when they reach the valley debris masses and participate in the underground drainage (Schmied, 2010). Consequently, there is no surface drainage in the entire upper St. Ilgen Valley. A portion of the groundwater emerges seasonally at the partly productive Kammerhof spring, which is responsible for the formation of the basis of the Ilgenerbach (Fabiani, 1980; Meidl et al., 1980; Bauer, 2010). Almost all spring streams are forced to infiltrate due to the thick cone of debris and subsequently recharge the groundwater. The direction of drainage, which results from the geology and morphology, is displayed in Figure 3a. Most of the springs in the Buchberg area are contact springs discharging from the limestone debris deposits. An overview of the springs in the Buchberg area and their discharge volume is displayed in Figure 3b (Fabiani, 1980). Karst water have been considered the potential source of the rivers and streams south of the Buchberg valley and in the area of Innerzwain, but the increased tritium content and conductivity of the water imply a lesser impact (Fabiani, 1980; Stadler and Benischke, 2009). The increased tritium content indicates a longer residence time in the subsurface, whereas karst waters experience a relatively short retention period. Elevated sulfate, calcium, and magnesium concentrations are the result of prolonged flow through a carbonate debris body (Schmied et al., 1980). Nevertheless, both karst- and precipitation water feed the over 200 m thick

body of loose sediments, which, in addition to its excellent retention capacity, also contributes to filtration, resulting in two advantages in the indirect use of karst water compared to direct utilization. These include firstly a lower risk of contamination and secondly the elimination of supply uncertainties due to varying water quantities (Bauer, 2010). The water supply of several Styrian municipalities, including the state capital Graz, is provided by one of the two vertical filter well systems of the Moarhof well intake (indicated with a red cross in Figures 3a and 3b), and which is regulated to 17.28 m³/day. The transport pipeline (red arrow in Figure 4a) with a total length of 68 km supplies the drinking water from the ZWHS to the networks of the drinking water providers or is used to enrich the groundwater, i.e. in Friesach (Bauer and Lieb, 2011)

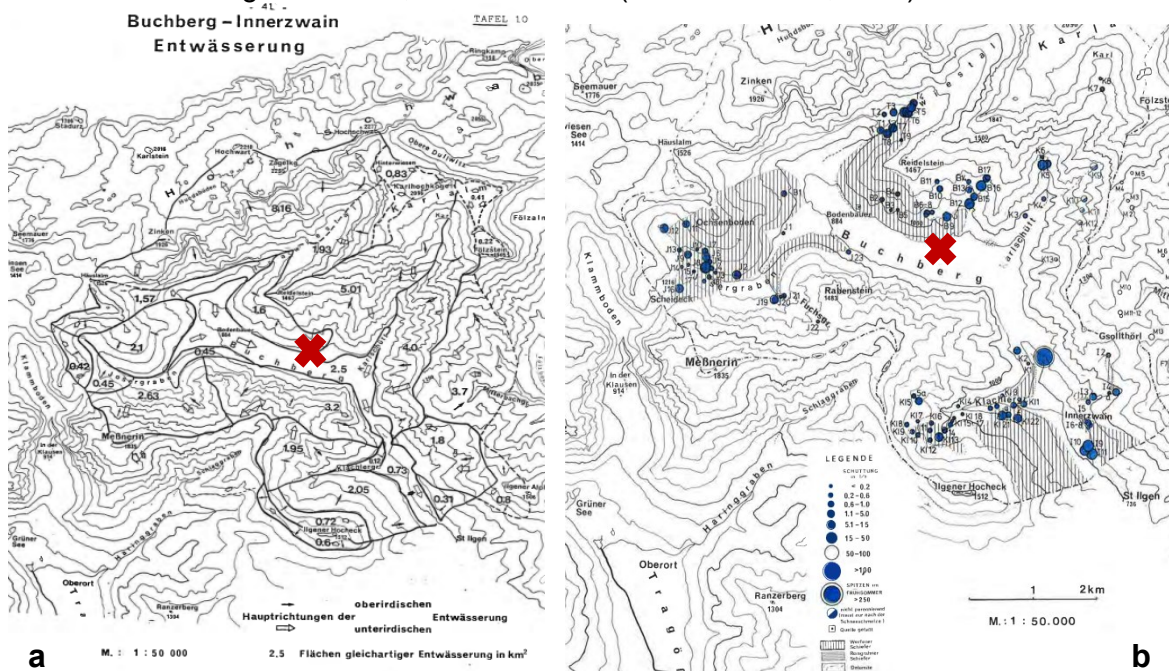


Figure 3: (a) Drainage type and direction in the Buchberg valley (modified after Fabiani, 1980). (b) Overview of the springs in the survey area and their discharge volume (modified after Fabiani, 1980). The red cross indicates the Moarhof well intake.

4.2. Hydrogeology at the northern margin

The main plateau of the Hochschwab Massif is characterized by intensive karstification, recognizable by various features such as up to 7000 dolines and 600 caves (Plan and Decker, 2006). A uranium tracer test confirms the drainage direction of the Kläffer spring in E -W direction (Figure 4b), correlatable with predominant karst features of the plateau and the existing topography (Bauer et al., 2016). The annual precipitation reaches up to 2200 mm/year, which is significantly above the Austrian average of 800 mm/year. (Kuschnig, 2009). In the northern part of the Hochschwab Massif, responsible for approx. 60 % of Vienna's drinking water supply, there are some of the most important springs, namely the Kläffer spring, the Brunngraben spring, the Seisenstein spring, and the Pfannbauern spring (high retention time). The former of the four

sources is the largest spring in the Eastern Alps, originating from a N-S oriented strike-slip fault and with a maximum discharge, measured during a thunderstorm event, of 34 m³/s and an annual average discharge of 13 m³/s (Bauer et al., 2016). In detail, the Kläffer spring consists of several water sources at different altitudes, some of which are only activated during periods of enhanced discharge. However, all these springs draw their water from the same karst water aquifer (Nachtnebel et al., 2012). This hydrological divergence, which results in more productive springs in the N, is caused by the impermeable Werfen Shales at the base of the carbonate rocks being higher in the S than in the N. A great deal of the precipitation water flows towards the north due to the north-oriented dip of the Werfen Shales (Bauer and Lieb, 2011). Especially during heavy rainfall events and snowmelt, the short retention time of the Kläffer spring, as well as the associated springs, is problematic, as it cannot be filtered properly. A discharge directly into the Salza, if required, is possible (Bauer, 2009). Increasing prosperity and the growing importance of hygiene made the construction of a second mountain spring pipeline essential, as the first (Rax,

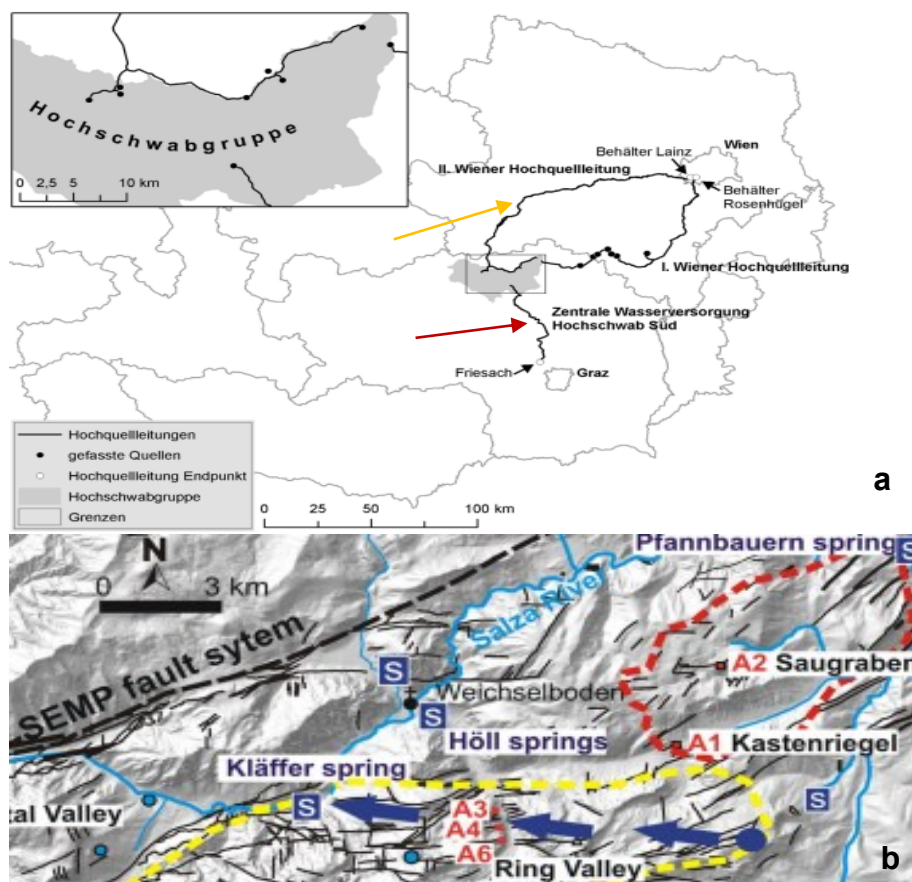


Figure 4: (a) Distribution of water from the Hochschwab, both towards the south and in the direction of Vienna. The red arrow displays the pipeline from the ZWHS and the yellow arrow shows the 2nd MSP (modified after Bauer and Lieb, 2011) (b) Flow direction (blue arrows) towards the Kläffer spring determined by a uranium tracer test (modified after Bauer et al., 2016). The blue arrows indicate the flow direction, and the blue circle marks the feed-in point for the tracer test.

Schneeberg) was overestimated in terms of yield. Based on the quantity of water on the northern slopes of the Hochschwab mountain, the 2nd Vienna Mountain Spring Pipeline (MSP) was built. This pipeline, running parallel to the Salzatal (Figure 4a), supplies 217,000 m³ of water per day to the south of Vienna over a total length of 180 km (Stadt Wien, 2023). Table 1 provides an overview of the core data of the two "sources" belonging to the Hochschwab Massif, which are relevant for the water supply of the respective catchment areas.

Table 1: Statistical data for a comparison of the 2nd MSP and the ZWHS (modified after Stadt Wien (Wasserversorgung in Wien 2001 bis 2021 - Offizielle Statistik der Stadt Wien., 2023), Bauer and Lieb, 2011)

Source	Commissioning	Power Ø [m ³ /day]	Length [km]	Flow time [hours]
2. MSP	1910	210.000	180	36
ZWHS	1993	172.800	68	-

Abbreviations: MSP = Mountain spring pipeline; ZWHS = Central water supply Hochschwab – South.

5. Historical data of the survey area

The Hochschwab Massif, due to its enormous importance for the water supply of Vienna, as well as the valleys south of the mountain group, including the Buchberg-St. Ilgen valley, whose relevance for the water supply of the city of Graz, along with Bruck an der Mur and other municipalities, have repeatedly come into the interest of various surveys. The initial aim of the investigations in the 1970s was to estimate the potential of the fracture waters, with the main objective being shortly shifted towards the recording of the groundwater supply and the water balance. The investigations carried out comprise geological and hydrogeological mapping, spring surveys, the drilling of investigation boreholes, precipitation measurements, geophysical tests, and the examination of soil samples (Fabiani, 1980).

5.1. Hydrogeological mapping

In the former investigations, a major objective was to estimate the relevance of the individual layers or formations for the water balance, respectively the re- and discharge pathways.

The Werfen Shales, situated in the footwall, are of utmost hydrogeological importance in the St. Ilgen Valley regarding their water-retaining properties. The main occurrence of these layers is as a water-stagnant bedrock. Figure 5a contains a map of the investigation area at that time, in which profile 2 corresponds approximately to the profile Hochschwab-Süd01 (hs01) of the geoelectrical investigation of this thesis. The basin fill (Figure 5b) consists mostly of alternating gravel and sand deposits, and the Werfen Shales as bedrock in the footwall, which however, reach the surface in the NW part of the profile (Fabiani, 1980). The Werfen Shales dip at about 30° to the north, submerge up to 300 m below the valley floor at Innerzwain, and return to the surface at Moarhof. The subsurface drainage is ultimately due to the tectonically induced shape. The Wetterstein limestones and Dachstein limestones are classified as more permeable rocks due to their higher degree of karstification. Although they account for a large part of the rock mass of the Hochschwab group, they are of minor importance in the Buchberg study area (Fabiani, 1980). The valley fillings, comprised of various unconsolidated sediments, are among the well-draining formations in the basin, being mainly decisive for the water balance and the associated subsurface drainage. However, as mentioned before, these sand and gravel layers reach a maximum thickness of up to 200 m at a valley width of 400-500 m (Fabiani, 1980). The surrounding debris cones and trenches result in an almost complete closure of the Buchberg basin, forcing surface water to percolate and ultimately to recharge the groundwater. Therefore, both the precipitation water and the surface water of the numerous creeks and streams infiltrate into these

unconsolidated sediments and respectively the groundwater. In addition, this results in a storage as well as filter function for any pollutants and contaminants (Fabiani, 1980).

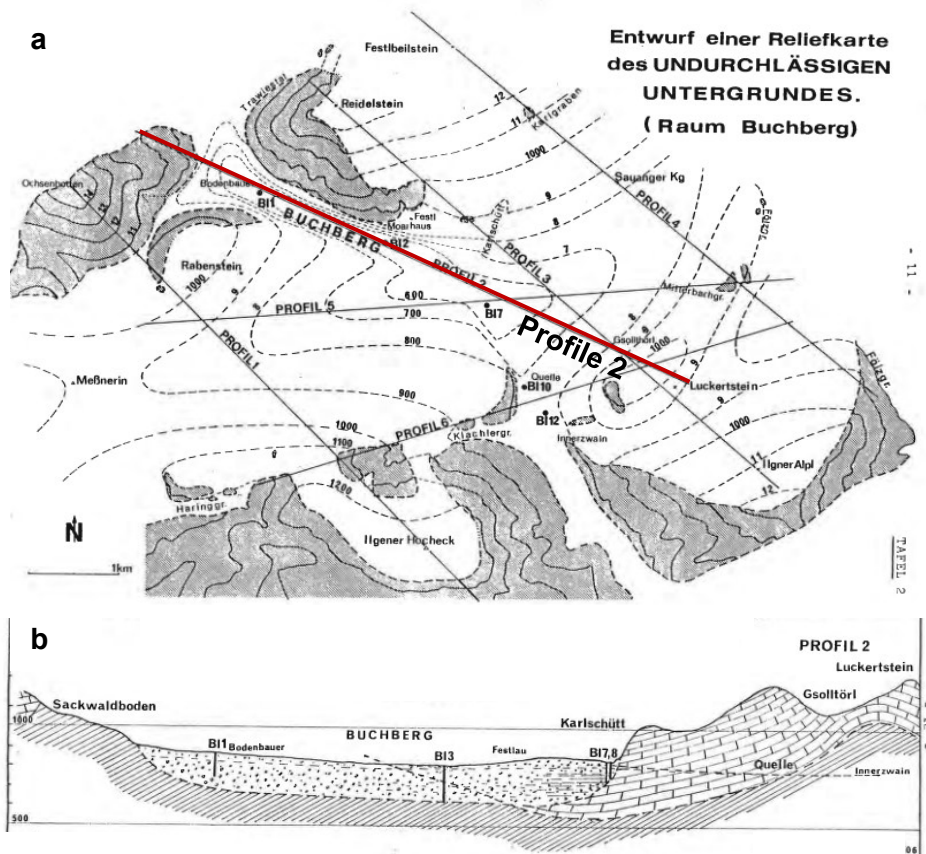


Figure 5: (a) Overview of the study area in 1980, with the relevant profile in red (modified after Fabiani 1980). (b) Profile from 1980 relevant for the recent investigations (Fabiani 1980).

5.2. Existing boreholes

A total of twelve boreholes were drilled for two distinctive and different purposes. The boreholes 1, 2, 3, 9, 10 and 11 were drilled for general survey purposes and were completed in the early 1970s. The remaining boreholes were drilled in the late 1970s for exploration further south of the investigation area. Borehole BI1 (highlighted as a red circle in Figure 6) was the first exploratory borehole in the entire Hochschwab region (Fabiani et al., 1980). Prior to the start of the drilling, the water table was expected at a depth of 6-7 m, while the bedrock was anticipated at a depth of 60 m. Therefore, the maximum target depth of the drilling campaign was set to 75 m. Contrary to expectations, the bedrock was not encountered at this depth, so additionally 50 m were drilled. The borehole profile (Figure 7) clearly reveals alternating bedding of sandy banks, gravel layers, and thin-bedded silty layers (Fabiani et al., 1980). At a depth of about 30 m, coarser material,

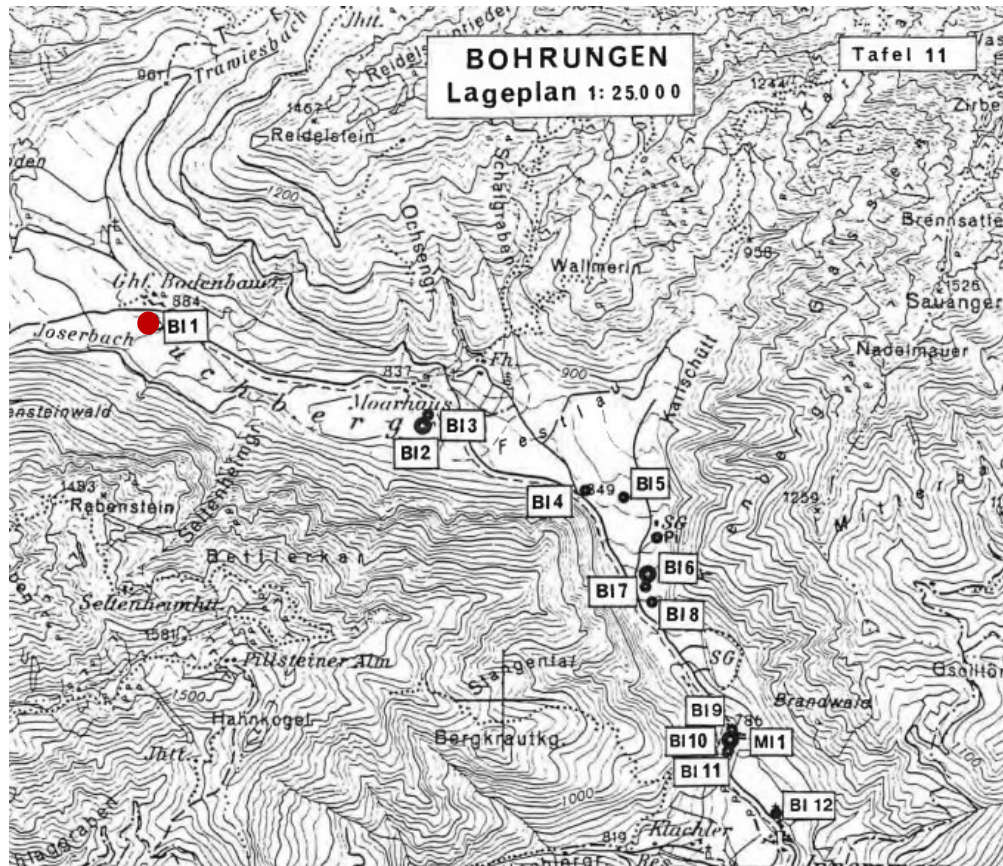


Figure 6: Map of the exploratory drillings (modified after Fabiani, 1980). The red circle indicates the position of the first borehole BI 1.

sourced from the surrounding debris cones, mixes into the succession. The exploratory boreholes BI2 and BI3 are located at the southeastern end of the Buchberg Valley (Moarhof), whereby BI2 is an investigatory well with a diameter of 900 mm. An alternating bedding of coarser and finer gravels, as well as isolated conglomerate layers is recognizable in BI2. Borehole BI3 has been drilled to reach the impermeable bedrock, consequently placed in a depression 50 m deeper than BI1. This borehole also shows a sandy-gravelly alternating bedding with silty intercalations, extending to a depth of 193 m. The Werfen Shales were detected for the first time at a depth of about 100 m, assuming material or debris supply from the valley background and at 202 m, the pre-Quaternary bedrock, again the Werfen Shales, was eventually encountered. A schematic and five times exaggerated geological map is shown in Figure 8, in which it is again indicated that BI1 does not reach the basin bottom, whereas BI3 was drilled deep enough to encounter the Werfen Shales. Based on these findings and the observed surface morphology, the basin floor was interpolated (Figure 8), leading to the conclusion that it would probably not be reached until a final depth of about 200 m at the location of BI1. A short transport route of the material has resulted in

the formation of the 200 m thick sand-gravel complex in the Buchberg basin, getting coarser towards the end of the valley and towards the bedrock. (Fabiani et al., 1980).

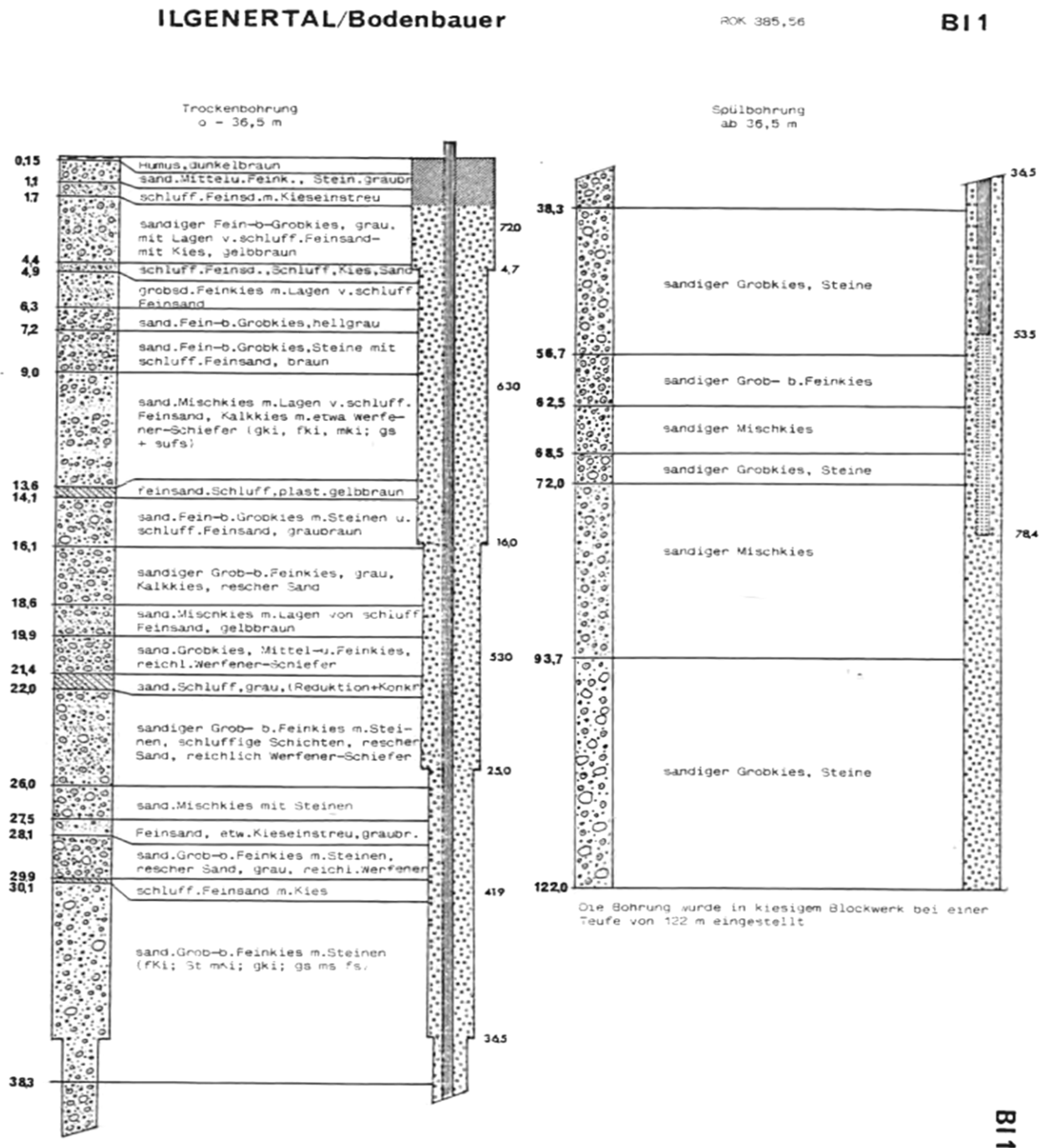


Figure 7: Borehole profile B11 of the drilling performed closest to the recent study area (Fabiani, 1980).

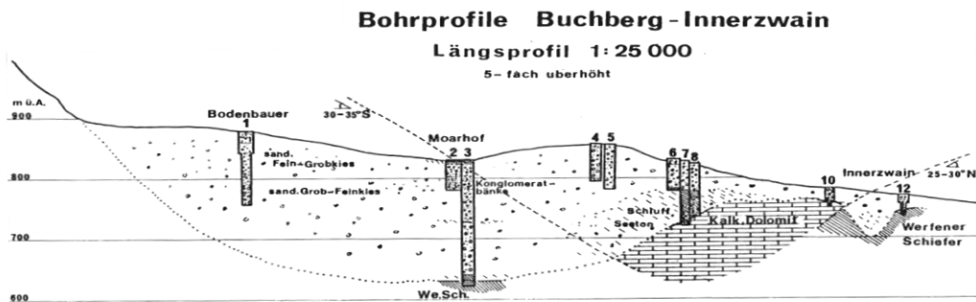


Figure 8: Geological profile across the Buchberg-Innerzwain area. (Fabiani, 1980).

5.3. Groundwater monitoring

For groundwater monitoring purposes, two potential level observation stations existed in the Ilgen Valley back then, with one being located at BI2 (Fabiani et al., 1980). Nowadays, level observations are feasible at almost all boreholes. The groundwater level at BI1 is only measurable or traceable to a depth of 70 m due to the accumulation of mud. If the water level drops in the fall and winter months, BI1 falls dry (Fabiani, 1980). The collected measurements show that in the Ilgen Valley, as well as in almost all valleys south of the Hochschwab, the extent of the natural level fluctuations in the hinterland appears to be much stronger than in the vicinity of the groundwater discharge at the end of the valley. Figure 9 illustrates the hydrograph of the

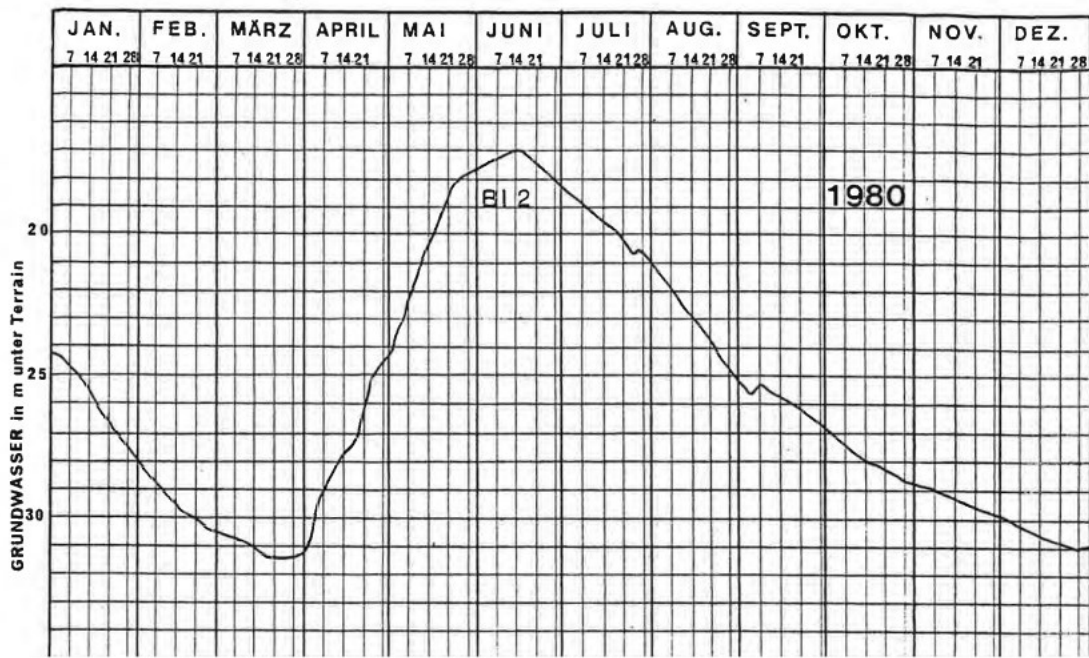


Figure 9: Variation of the groundwater level measured in BI2 (Moarhof) with seasonal high and low periods (Fabiani, 1980).

groundwater level for BI2 in 1980 (Fabiani, 1980). The influence of snowmelt is clearly visible, shown by a maximum of the hydrograph in June and July. Compared to other southern Hochschwab valleys, the maximum is shifted back by one or a maximum of two months, because of the delayed snowmelt influenced by high regions in the Ilgen Valley. Due to the thick overburden, precipitation only affects the groundwater level in the valley during extreme weather or heavy precipitation events. Maximum water levels were measured mostly one week later in BI10, which is located 1.4 km away from BI2 (Fabian, 1980). In 1975, on behalf of today's ZWHS, geothermal investigations were carried out to provide information about the temperature curve with increasing depth and to identify any water-bearing, porous horizons. In addition, these results were intended to determine a mean temperature gradient (Fabiani et al., 1980). The groundwater level was encountered at a depth of 24.92 m using a highly sensitive temperature probe in BI 2 as part of a geothermal investigation campaign. A possible decrease in temperature with depth is due to the influence of colder meltwater (Fabiani et al., 1980).

5.4. Geoelectric survey

In the survey from 1980, the southern St. Ilgen Valley was investigated, whereas the exact location of the geoelectrical surveys is nowadays hard to determine since there is no exact position of the profiles on the map (Figure 10). However, it was roughly situated between boreholes BI4 and BI12 (Innerzwain - Karlschütt). The project objectives back then were to verify the subsurface conditions determined in the drillings, to identify the top of the aquifer, and to locate the Werfen Shales underlying the Quaternary basin fillings (Schmid et al., 1980).

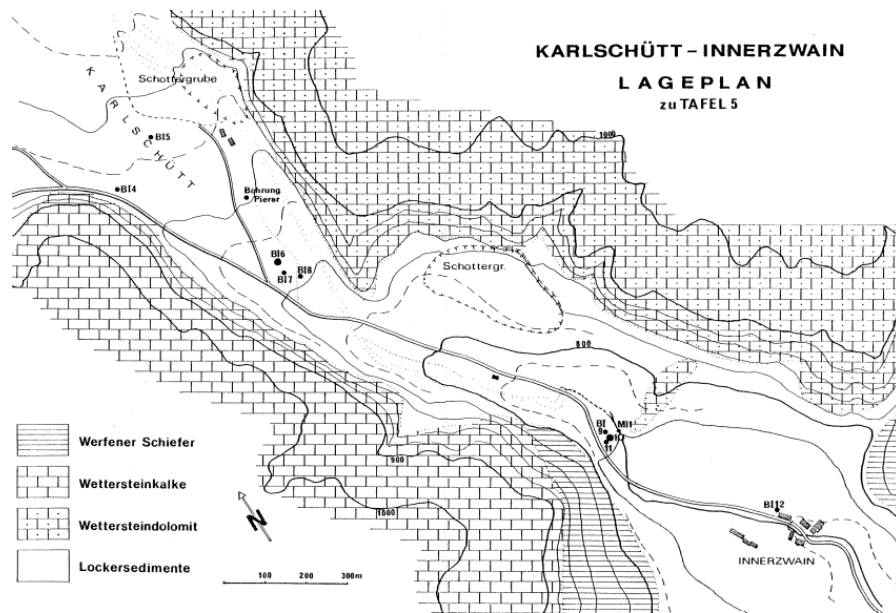


Figure 10: Map showing the location of the geoelectric survey in 1980 (Schmid et al., 1980).

The survey was conducted with the “Terrameter”, a resistivity measurement apparatus from the Swedish company ABEM, which was operated at 4 Hz AC and could produce results to a maximum penetration depth of 200 m. Rainy conditions, causing a soaking of the ground, improved the overall circumstances and the survey duration considerably. A Schlumberger array was chosen for the depth sounding, where the potential electrodes are spaced closely together to keep the dipole spacing small (*distance “a”*) and the current electrodes successively move further apart to increase the penetration depth (Schmid et al., 1980). Nine profiles with a total length of almost 3000 m were measured, of which four longitudinal profiles are relatively parallel to the valley axis and the remaining five profiles run perpendicular to it. The maximum electrode spacing “AB” was 400 m, implying a penetration depth of 120 m to 150 m. This penetration depth is partly due to the electrode spacing, but also, especially, for the transverse profiles, due to the narrowness of the valley caused by possible reflections from the steeply dipping rocks to the east and west of the site (Schmid et al., 1980). Multi-layer cases posed significant problems in the interpretation process until the mid-1970s due to the use of theoretical-sounding curves. However, this project relied on a computer program for interpretation purposes. Hence, for the previously determined number of layers, the apparent resistivities are assigned to the respective depths and subsequently, the true resistivities are calculated. The deviation of the two resistivities is observed in order to adjust the layer model if necessary (Schmid et al., 1980).

The survey has taken place in the south and southwest of the Bodenbauer area, nevertheless, some findings are extremely relevant, especially regarding the assignment of the individual resistivities to the respective layers. The procedures for the investigation at that time were vertical electrical soundings directly at known and existing boreholes, in which drill cores were already evaluated and through which the layer structure at the explicit position was already identified (Schmid et al. 1980). If drilled deep enough, the resistivities interpreted in the sounding curves were assigned to the layer packages. Table 2 shows the respective resistivity ranges for the encountered formations (Schmid et al. 1980). Based on the results in Table 2, clear demarcations between the individual mean values can be seen. The lacustrine clays and the weathered Werfen Shales show similar readings but could be explicitly identified due to their spatial separation in the field. Considering the standard deviation, it is also obvious that significant overlapping areas can occur, for example in the case of the weathered limestone and the Werfen Shales. However, assisted by data from monitoring wells, these layers were differentiated.

Furthermore, due to the high standard deviation of the values, there might be an overlap with the resistivities of the water-bearing gravels, which, however, could also be excluded by profile correlations. The relatively large standard deviation is due to large inhomogeneities within the individual layer packages, as well as a too-small-scale subdivision of the, at that time, new computer interpretation program (Schmid et al., 1980).

Table 2: Overview of the measured resistivities and the corresponding lithologies (Schmid et al., 1980).

Lithology	Resistivity
Dry gravel	2197 ± 1570 Ωm
Groundwater-bearing gravel	581 ± 247 Ωm
Lacustrine clay	206 ± 75 Ωm
Karstified limestone	1302 ± 992 Ωm
Impervious limestone	19080 ± 14295 Ωm
Weathered Werfen Shale	188 ± 45 Ωm
Werfen Shale	926 ± 704 Ωm

5.5. Seismic survey

A refraction seismic survey in 1971 (Figure 11) was designed to determine the relief of the pre-Quaternary basement, the thickness of the individual strata, and to gather information on the lithology, which would serve as a supplement to the surface mapping. Several complicating factors hindered the accomplishment of the objectives, mainly due to the narrowing of the valley, which significantly reduced the variation of the profile placement (Schmid et al., 1980). Furthermore, the influence of the rocks on the steep flanks, which led to strong impulses and reflections, posed a problem. This phenomenon could not be eliminated, due to the unknown thickness of the Quaternary basin fill. Longer profile sections were required, which again, were more easily affected by the influence of the flanks. The inhomogeneous composition of the valley fill, manifesting itself in a wide dispersion of velocities, presented another issue (Niesner, 1971).

The profiles, 8 km long in total, were predetermined by the existing morphology and the shape of the valley. The main profiles run almost parallel to the valley axis and are complemented by profiles running perpendicular to it. An attempt was also made to lay the profiles in such a way as to enable an exchange of information with the planned boreholes. Overall, 9 profiles were shot, of which only two are relevant for this thesis, and their location is shown in Figure 11. A certain part of Line 1 is appropriate (Shot points 18-20, 4, 11-12), as well as Line 3 (Shot points 1-5). The amount of

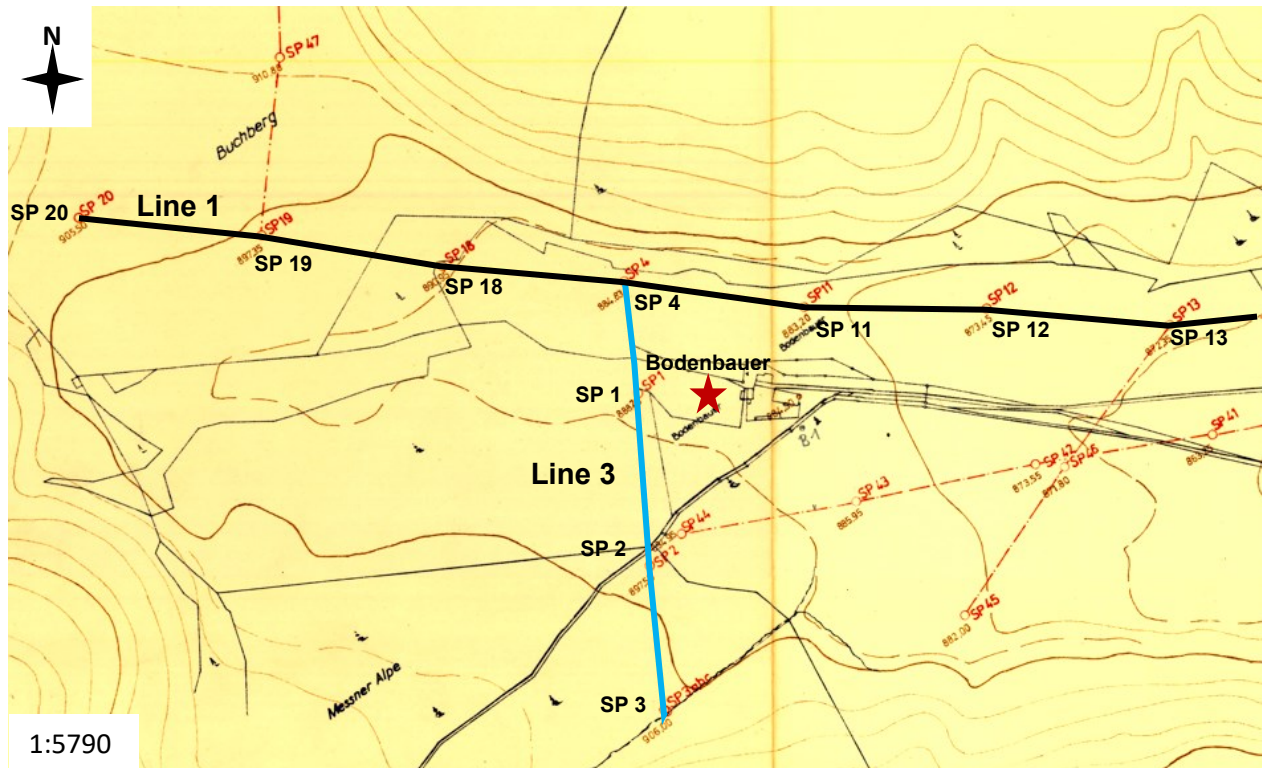


Figure 11: Overview map illustrating the exact location of the relevant seismic profiles from 1971. Line 1 (black) runs almost parallel to hs01, and Line 3 (blue) runs almost parallel to hs02 (modified after Niesner, 1971) The location of the Bodenbauer restaurant is indicated by a red star. Abbreviations: SP = Shot point.

energy required was strongly dependent on the degree of consolidation of the weathering layer, therefore in the vicinity of the Bodenbauer restaurant, more energy was required to obtain technically accurate readings. The distance between two shot points is 220 m and the geophone spacing is 20 m. Part of the layouts were shot with triple overlap in order to reach the bedrock, which is characterized by high velocities, relatively safe (Niesner, 1971).

The seismic measurements and data analysis in the study area showed a 3-layer case in most parts, in a few even a situation with 4-layers. The uppermost horizon (V1), revealing a certain thickness, displays velocities between 350 and 500 m/s and is composed of unconsolidated rock. The velocity variation in the second horizon (V2) is more pronounced compared to the uppermost horizon, although it can be attributed to a zonal arrangement, indicating either a lithologic change or a shift in the catchment area (Niesner, 1971). One of the areas comprises velocities between 800 and 1300 m/s, which could indicate dry Quaternary strata. The second interval between 1500 and 2000 m/s may already indicate groundwater-bearing gravels or the presence of strongly consolidated sediments. The third (V3) and fourth (V4) horizons represent the pre-Quaternary basement, with velocities of either 2500-3000 m/s or 4000-6000 m/s, respectively. The basement, consisting of Werfen Shales, limestones, and dolomites, with the former spanning the lower velocity range and the latter the higher range (Niesner, 1971).

Line 1 (Appendix 16.1):

From the Sackwaldboden in the north of the profile to the Bodenbauer restaurant (shot points 20-11), velocities of 400-500 m/s are encountered in the uppermost layer and its thickness increases from the southeast, SP 4, from 9 m to the northwest to 15 m. The situation is more difficult considering the second horizon since both the velocities (1300 to 1900 m/s) and the thicknesses vary even at short distances. In particular, the thickness decreases abruptly at SP 18 from 24 m to 18 m and later to 12 m (Niesner, 1971). Fabiani et al. (1980) assume an entanglement of the Quaternary strata in this area. In the V3 horizon, velocities between 2700 and 3200 m/s are encountered, indicating the Werfen Shales and thus a possible bedrock. Partly even higher velocities of up to 6000 m/s were measured, possibly explained by calcareous and dolomitic intercalations. In addition, a geological fault traverses the profile, which already affects the deeper refractors between shot points 4 to 11. Strongly fluctuating velocities in the V2 horizon between shot points 11 and 14 are possibly due to a debris cone (Niesner, 1971).

Line 3 (Appendix 16.1):

Line 3, which runs approximately parallel to profile Hochschwab-Süd02 (hs02) of this thesis, was shot before the actual measurement program and yielded essential information about velocities and velocity ratios. Within the Quaternary, lateral velocity variations occur. Velocities averaging about 500 m/s are found in 8-12 m thick unconsolidated strata, which is underlain by a refractor, that still belongs to the dry gravels according to the measured velocities of about 1000-1100 m/s. (Niesner, 1971). Subjacent to this horizon is possibly the groundwater bearing gravel zone (Aquifer) recognizable by the velocities of 1500-1800m/s, where local maximum velocities of up to 2200 m/s are encountered as well. Another interpretational approach beside the groundwater-bearing Quaternary would be more strongly consolidated sandy and loamy gravels. Generally, a determination of the depth of the bedrock turned out to be very difficult due to the irregular relief. Pulses originating from the NE were recorded, which could be indications of a very steeply dipping valley flank around shot point 4. The velocities of the basin bed indicate a heterogeneous structure consisting of Werfen Shales and limestones (Niesner, 1971).

6. Measuring procedure and methods

The theoretical background of the methods applied in this study and their underlying physical principles are described in more detail in the following chapter.

6.1. Basic principles

The fundamental law (Equation 1a) underlying geoelectric is Ohm's Law (Revil et al., 2012). The voltage U [Volt] is responsible for the movement of the charges and the current I [Ampere] describes the flow rate of charge carriers per second, where the direction of flow depends on the charge itself, as positive particles move from a higher to a lower potential (Dentith and Mudge, 2014). The electric flow is maintained until the energy source is switched off. If there is a resistance R [Ohm] encountered along the flow of the charge carriers, a restraint of motion occurs. This resistance is partly related to the geometry and partly to the internal properties of the material (Loke, 2021). An increase of the cross-section reduces the resistance, whereas enlarging the length leads to a rise in resistance (Loke, 2021). However, an effective statement about the ability of a material to prevent electric charge from flowing is only possible after removing the geometric effect in order to obtain a comparability to the unit cube of the material. This is the resistivity ρ (Equation 1b) of the material (Dentith and Mudge, 2014). The reciprocal of the resistivity, the electrical conductivity σ [Siemens per meter] describes the effortlessness with which the electric current advances (Dentith and Mudge, 2014). Equation 1d shows that small potential differences occur along a body due to low resistivities. Conductivities of 10^{-8} S/m and smaller are typical for insulators. Conductors, on the other hand, have conductivities greater than or equal to 10^5 S/m, whereas semiconductors and electrolytes are in between these boundary values. Fundamentally, conductors have loosely bound electrons, allowing current to flow easily when applying an external field. The more energy required to move the electrons, the lower the conductivity or the higher the

Current $I = \text{Voltage } U / \text{Resistance } R$	(a)
$\rho \text{ [}\Omega\text{m]} = R \text{ [Ohm]} * k_{\text{geom}} \text{ [m]}$	(b)
$k_{\text{geom}} = \text{Cross-sectional area} / \text{Length} = [\pi r^2 / l]$ in the case of a cylindrical specimen	(c)
$V = I * \rho / k_{\text{geom}}$	(d)

Equation 1: (a) Ohms law. (b) Resistivity of a material. (c) Geometrical correction factor. (d) Ohms law modified. (modified after Dentith and Mudge, 2014)

resistivity. The temperature also has a profound influence, since the energy of the electrons is increased allowing them to move with more ease (Dentith and Mudge, 2014).

6.2. Electrical properties of the natural environment

The conductivity within the rock originates either from a connected pore space via the present fluids or is based on the conductive minerals in the matrix (Revil et al., 2012). The fluids covering the pore space are massively responsible for the electrical properties in porous rocks. The massive heterogeneity, as well as the associated problem of scale sensitivity and representative sampling, characterize the electrical properties in rocks and minerals (Dentith and Mudge, 2014). The largest measured conductivity in repeated measurements is considered as the representative resistivity. Figure 12 provides an overview of the wide range of resistivities in different rocks and minerals (Loke, 2021). Most rock-forming minerals possess conductivities between 10^5 and $10^{-8} \Omega\text{m}$ and are regarded as semiconductors. Silicate and carbonate minerals are examples for insulators. Water as a pore content is a good conductor compared to air and ice, although a distinction between pure water as a poor conductor and "impure" water, whose conductivity increases with increasing salinity or higher concentration of dissolved ions must be made. The water level frequently provides a contrast in conductivity compared to the unsaturated zone. In general, conductivity is not representative for rock interpretation and the resistivities are mostly between those of groundwater and rock-forming minerals (Revil et al., 2012). The greater the porosity, the

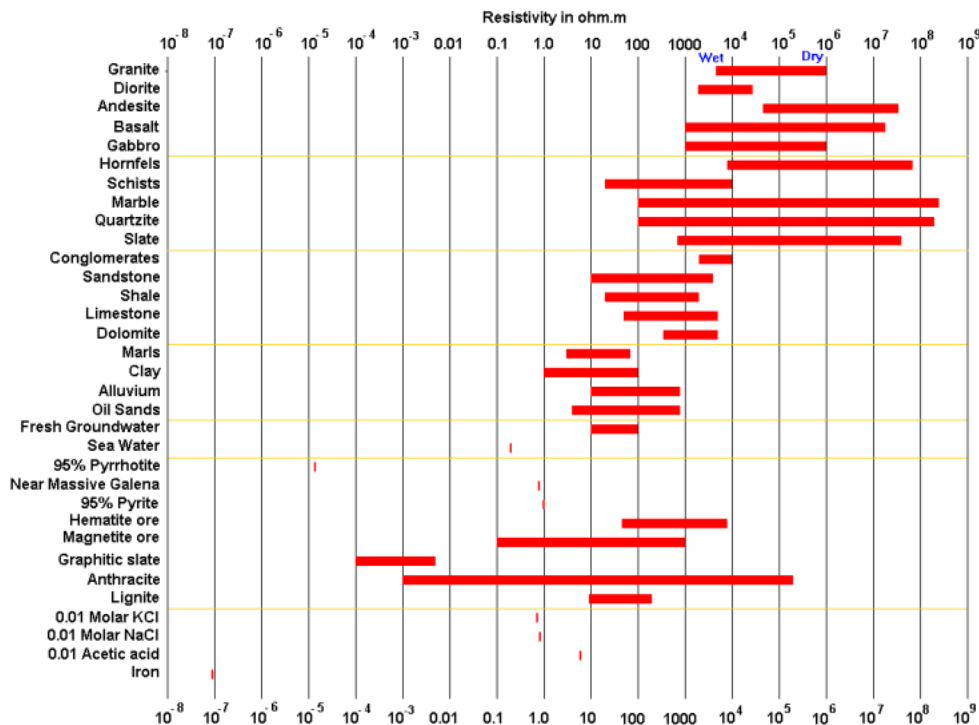


Figure 12: Resistivity ranges for selected rocks and minerals (Loke, 2021).

closer the conductivity resembles that of groundwater. Clayey minerals, especially moist ones, or as a proportion of other aggregates are particularly conductive. Sedimentary rocks also exhibit high conductivity due to high porosity and high humidity levels, whereas a decrease in porosity and permeability increases the resistivity. The weathering processes lead to an increase in porosity and permeability, but on the contrary clay mineralization might have the opposite reaction (Revil et al., 2012). Lithological interpretations based on conductivity are difficult, as in most cases it is the reaction of the pore contents that is determined, and not the rock-forming minerals, responsible for the geology (Dentith and Mudge, 2014).

6.3. Electrical Resistivity Tomography (ERT)

ERT was primarily developed for high-resolution imaging of the shallow subsurface to enable water- or soil clean-up monitoring. The basic principle is based on a large number of measurements of the distribution of the subsurface resistivity by using four electrodes in a certain arrangement. Subsequently, the true resistivity is derived from these recordings as a product of the inversion process (Daily et al., 2005; Loke, 2021). These measurements are either made in-situ on the ground, in boreholes, or as a combination. ERT has quickly emerged as a viable method to identify various deposits and subsurface liquids (Daily et al., 2005).

6.3.1. Data Acquisition Systems

Geoelectric measurements require a current source to generate their own electric field and electrodes for ground contact. The active source is most commonly a battery or a generator and the electrodes, oftentimes basic metal sticks, are hammered into the ground (Dentith and Mudge, 2014). However, this can lead to problems with highly resistive layers on the surface. Four electrodes (Figure 13), including two for injecting a known current into the subsurface (by convention named A and B) and two for measuring the potential difference of the current flow in the subsurface (by convention named M and N), are required (Loke, 2021). Ohm's law connects the current and the measured voltage via the impedance in the frequency domain. The latter is

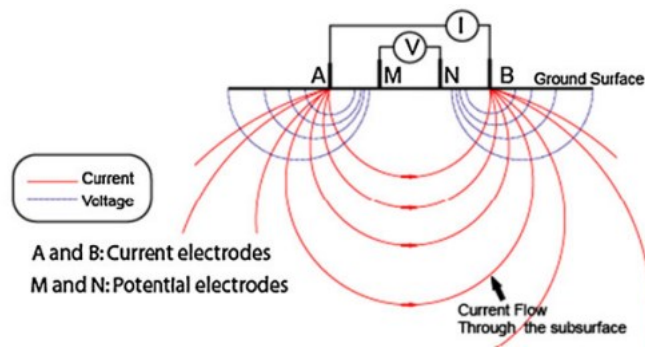


Figure 13: Measurement setup with four electrodes, showing A and B as current electrodes and M and N as potential electrodes (Revil et al. 2012).

the quotient of the apparent electrical resistivity and a geometric factor corresponding to the array of electrodes (Dentith and Mudge, 2014). In the time-domain, magnitude, and chargeability are linked via voltage and current (Kemna, 2000). A major challenge is the determination of countless impedance values, obtained by various combinations of electrode arrays. The Pole-Pole array, where two electrodes are at an "infinite" distance with one of them being used to inject the current and the other one as the voltage reference pole (Loke, 2021). The two remaining electrodes are used in a variety of different layouts, as the measurements can also be reversed making the measurement reciprocal, which yields an identical result unless non-linear effects are ubiquitous (Daily et al., 2005). Other relevant arrays are the Pole-Dipole, the Wenner-Alpha, and the Multiple Gradient arrays, which are described in more detail in Chapter 6.3.4. along with their advantages and disadvantages. However, the costs of set-up and electrode installation can be limiting factors. Physical restrictions such as surface conditions (asphalt, concrete, etc.), prevent the installation of surface electrodes, as well as buildings along the profile, make the placement of remote electrodes difficult (Daily et al., 2005).

6.3.2. Measurement of resistivity and apparent resistivity

Equation 1d describes the true electric resistivity in the case of a homogeneous subsurface. However, since this does not correspond to the real underground and additionally inhomogeneities disturb the electric field, a deviation of the potential compared to that of an ideal homogeneous space arises (Daily et al., 2005; Revil et al., 2012). The measured resistivity is then referred to as the apparent resistivity since the electrical homogeneous half-space is used as the basis for the equation. This apparent resistivity depends on the electrode array and the distribution of the true resistivity in the subsurface (Cheng et al., 1990; Dentith and Mudge, 2014). The conversion of the apparent resistivities into true resistivities is a major challenge and will be described in more detail in Chapter 7. The measurement of subsurface electrical properties depends on the electrode geometry and position, as well as the distance of the electrodes from the target. Consequently, the electrodes measure the parameters of a certain range (Dentith and Mudge, 2014; Loke, 2021). By varying the positions of the individual electrodes, such as along a profile, measurement data from different depths and ranges can be acquired. The influence of deeper anomalies and structures may be diversified by the distance between the current electrodes (Dentith and Mudge, 2014). Usually the greater the distance between the electrodes, the greater the penetration depth will be. Figure 14 depicts that at a penetration depth of $AB/2$, 50 % of the current will flow above this depth (Robinson and Coruh, 1988). A pseudo-depth can be assigned to each measured value based on the electrode geometry and the electrode spacing. The measurements along a profile with variable electrode spacing are suitable for creating a pseudosection (Loke, 2021). The lateral

resolving capability depends mainly on the distance between the potential electrodes (Dentith and Mudge, 2014). A large number of electrodes and a multi-channel receiver system allow precise measurements of a wide range of data, eliminating the need to relocate the electrodes after each measurement and thus saving an immense amount of time (Griffiths and Barker, 1993). Instead, only the distance between the electrodes and their relative position in the profile, as well as the position of the entire array, is changed due to the link between the electrodes and the recorder channels (Dentith and Mudge, 2014).

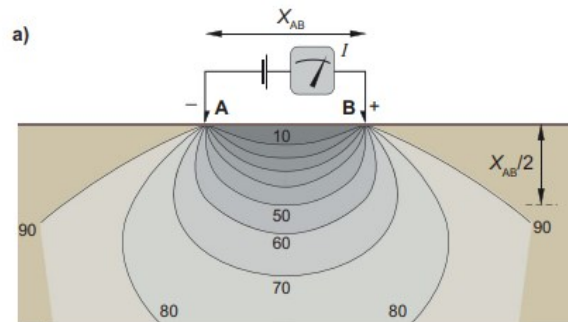


Figure 14: Proportion of the current that flows to a certain depth. 50% of the current reaches a penetration depth of $AB/2$ (Dentith and Mudge, 2014).

6.3.3. Pseudosections

Pseudosections are excellent for a quick check-up of the data integrity, as the apparent resistivities are depicted. Given their rapid availability, the data quality check process can be performed in the field and any errors, whether technical or measurement-related, can be detected, and treated in time and on site (Dahlin and Zhou, 2006). Experienced geophysicists can make an initial assessment of the data quality and identify outliers. Constant and continuous fluctuations of the apparent resistivity in the pseudosections suggest a good measurement result. Additionally, a first rough estimation of the structure of the investigation area is already possible by looking at the preliminary outcome (Dentith and Mudge, 2014). However, this estimation must be addressed cautiously, as the individual arrays have different sensitivity functions, making the structures recognizable only after the inversion has been completed. Furthermore, prior to the inversion, the data may be revised by removing clearly recognizable outliers during data editing, thus not falsifying the inversion result itself (Dahlin and Zhou, 2006). Figure 15 depicts the generation of a pseudosection, where the measured resistivities or conductivities of the respective dipole spacings are plotted at the intersection in depth. The angle, at which the point in the pseudosection is created, is dependent on the electrode configuration itself. Deeper points of the pseudosections result from larger dipole spacings and values from equal dipole spacings plot on the same line.

The lateral offset corresponds to the displacement of the current and potential dipoles along the profile (Dentith and Mudge, 2014). Sometimes the source geometry is not reproduced in the pseudosections, which results in a "V-shaped structure", known as "pants-legs". This is caused by the occurrence of electrical anomalies below the current and potential electrodes, influencing the outcome. The recording of the values at points that extend diagonally downwards leads to the two pants-legs. They can also be formed by resistivity contrasts due to a geological contact whereby one side of the pant-leg has an extremely high resistivity and the other a much lower one (Dentith and Mudge, 2014). The limitation of the resolving capacity of pseudosections is caused by deviations from the linear profile, as well as the location of the electrodes in relation to the occurrence of the anomaly. Nevertheless, pseudosections do not provide a true representation of the electrical structure of the subsurface. It is merely a mathematical abstraction that needs further modeling and interpretation to convert it into true depths of the subsurface (Oldenburg and Li, 1994; Dentith and Mudge, 2014).

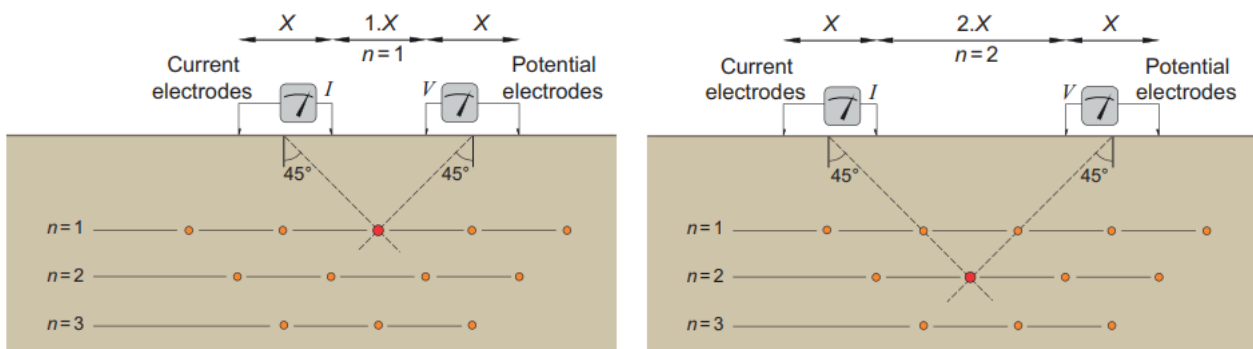


Figure 15: Creation of a pseudosection for distinct spacings between current and potential electrodes (Dentith and Mudge, 2014).

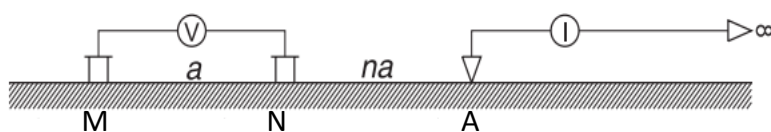
6.3.4. Array Configurations

Geoelectric methods, such as the ones relying on direct current, are ideal for acquiring data quickly, efficiently, and inexpensively. Electric resistivity tomography applications, commonly performed at the surface, use a variety of electrode arrangements (Dahlin and Zhou, 2004). The vertical and lateral resolving ability, the penetration depth, the ease of handling, as well as the data processing and the signal-to-noise ratio are some of the most important criteria considered when selecting the appropriate electrode configuration (Dentith and Mudge, 2014). Different arrays have several advantages and disadvantages, all with the primary goal of measuring the lateral and horizontal changes in resistivity and subsequently displaying them in pseudosections (Dahlin and Zhou, 2004). Based on a dense set of data, an accurate reconstruction of the subsurface has already been modeled in the past by many geophysicists (Shima, 1992; Li and Oldenburg, 1992). Significantly more time is needed to measure a large amount of data. Therefore, measurement teams often resort to data density reduction in order to save time and

consequently money. Nevertheless, by using multichannel data loggers, which are capable of simultaneously sampling numerous data points at each current injection into the ground, data density is not compromised, and the measurement time is faster (Dahlin and Zhou, 2006). Several electrode configurations have been used since the 1950s, differing mainly in the arrangement of the potential electrodes and the current electrodes, as well as their distance between them. The spacing between electrodes is declared by the letter "a", as well as by the letter "n" whenever the length "a" is being multiplied (Dahlin and Zhou, 2004). The measurements for this thesis were conducted using the following electrode configurations. Dipole-Dipole, Pole-Dipole, Wenner-Alpha and Multiple Gradient, along with different combinations of the various arrays in order to maximize their advantages and reduce their drawbacks, were used.

Pole-Dipole

One of the most used configurations is the Pole-Dipole array, in which typically one current electrode is located at an "infinite" distance from the other electrodes to provide greater depth of penetration. The separation between the potential electrodes, as shown in Figure 16, is abbreviated by the letter "a". A multiple of "a" ($n \cdot a$) is the distance between the receiver electrodes and one of the two current electrodes. These three electrodes are positioned along a linear profile. The 2nd remaining transmitter electrode is located at a greater distance, at least " $10 \cdot a$ ", differs from the linear profile and is laid out at a right angle to the profile (Zonge et al., 2005). This ensures an equally good penetration depth over the entire profile and minimizes electromagnetic coupling. The measured parameters include the current I as well as the voltage V and the apparent resistivity ρ_a . The penetration depth, enhanced by the transmitter electrode at an infinite distance, is larger than " $2.5 \cdot a$ " for a transmitter-receiver distance of $n=6$. The lateral resolution, however, is limited to " $a/2$ " (Zonge et al., 2005). In general, Pole-Dipole arrays are, despite the moderate anomaly effects, used to generate images with good spatial resolution and a high penetration depth. When



$$\rho_a = (V/I) \pi n(n+1) (n+2)$$

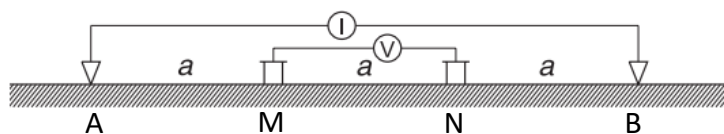
- Receiver Dipole spacing = a
- Receiver dipole and current electrode spacing = n times a
- Penetration depth $> 2.5a$
- Lateral resolution $\sim a/2$

Figure 16: Visualization of a Pole-Dipole array with the respective characteristics (modified after Zonge et al., 2015). (Abbreviations: A, B = Current electrodes; M, N = Potential electrodes; ρ_a = apparent resistivity; V = Voltage; I = Current; a = Dipole spacing).

compared to Dipole-Dipole arrays, more cable is required due to the positioning of the remote electrode (Zonge et al., 2005). The disadvantage of using a remote electrode is the accessibility of the site, as a certain range is needed for the placement and an increased noise level may occur (Dahlin and Zhou, 2004).

Wenner-Alpha

A more robust electrode setup is the Wenner-Alpha array. In this case, the distance between the potential electrodes (M and N) equals “a” and the current electrodes (A and B), both placed outside the receivers, are also at a distance “a” from the corresponding (Figure 17), thereby resulting in a uniform spacing between the four individual electrodes (Zonge et al., 2005). Similar to the Pole-Dipole array before, current I, voltage V, and apparent resistivity ρ_a are obtained. The penetration depth is approximately “AB/8” and the inter-electrode spacing is constant, resulting in a lateral resolution that depends on the size of the individual electrode separation. The narrower the distances, the better the resolution. Wenner-Alpha array, qualitatively like the Schlumberger electrode set-up, has the major advantage of being able to determine the depths quite accurately. In addition, this array is less susceptible to noise thus resulting in a better signal-to-noise ratio. Nevertheless, the spatial resolution is significantly worse compared to the Pole-Dipole and the following Dipole-Dipole array, resulting in a slightly poorer image quality (Dahlin and Zhou, 2004). The sensitivity function of the Wenner-Alpha array is shown in Figure 20, illustrating clearly that vertical structures will be less well resolved due to the low lateral sensitivity (Dahlin and Zhou, 2006). Findings summarized by Zonge et al. (2005) suggest that the Wenner array is not well suited for vertical electrical soundings, however, this method is vital for covering vast regions (Loke, 2021).



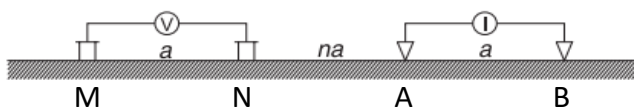
$$\rho_a = (V/I) 2\pi a$$

- Receiver Dipole spacing = a
- Transmitter electrodes placed outside the receiver electrodes
- Transmitter -Receiver spacing = a
- Penetration depth $\sim AB/8$

Figure 17: Set-up of a Wenner array with the respective key features (modified after Zonge et al., 2004). (Abbreviations: A, B = Current electrodes; M, N = Potential electrodes; ρ_a = apparent resistivity; V = Voltage; I = Current; a = Dipole spacing).

Dipole-Dipole

Another frequently used electrode configurations in geoelectrical exploration is the Dipole-Dipole electrode configuration. The spacing between the two current electrodes and the two potential electrodes is constant and is again denoted by the letter "a" (Zonge et al., 2005). However, the distance between the current electrodes and the receiver electrodes is a multiple of "a" ($n \cdot a$) and these two electrode pairs are placed along a linear profile. The apparent resistivity is denoted by ρ_a and is shown in Figure 18 for the Dipole-Dipole array case. The term " $\pi n(n+1)(n+2)$ " of Figure 18 is the geometric factor specifically associated with the Dipole-Dipole array. The parameters measured and subsequently calculated include the current I , the voltage V , and the apparent electrical resistivity ρ_a . The penetration depth for $n=6$ is approximately " $2a$ " and the lateral resolution corresponds roughly to " $a/2$ " (Zonge et al., 2005). Dipole-Dipole arrays have the same symmetrical electrode configurations for both standard and reciprocal measurements, resulting in an excellent data quality control capability. Concerning the quality of the inversion results, Dipole-Dipole measurements are comparable to Pole-Dipole recordings, especially in resolving the positions of vertical and inclined structures (Zonge et al., 2005). Narrower vertical structures can be better resolved due to the higher lateral resolving power of the Dipole-Dipole array, as shown in Figure 20. The higher the factor "n", the better the resolution. Nevertheless, a greater separation of the two dipoles from each other also results in a lower sensitivity in the in-between region, whereas the sensitivity at the end of the profile, however, is quite strong (Dahlin and Zhou, 2006). Another advantage is the relatively high anomaly effect. Disadvantages are the limited depth resolution, much better with other arrays and the relatively high proneness to random noise (Dahlin and Zhou, 2004). Overall, the horizontal resolution and the penetration depth are qualitatively good. Additionally, the lateral and vertical resolution can be improved by reducing the spacings "a", if interested in structures or information near the surface (Zonge et al., 2005). Nevertheless, it is a less robust array, that is more sensitive to complex three-dimensional structures and spacing errors (Zhou and Dahlin, 2003).



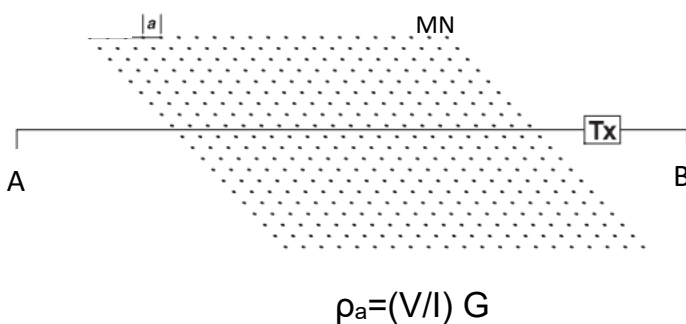
$$\rho_a = (V/I) \pi n(n+1)(n+2)$$

- Dipole spacing = a
- Distance between receiver and transmitter = n times a
- Penetration depth > 2a
- Lateral resolution ~ a/2

Figure 18: Illustration of a Dipole-Dipole array (modified after Zonge et al., 2014). (Abbreviations: A, B = Current electrodes; M, N = Potential electrodes; ρ_a = apparent resistivity; V = Voltage; I = Current; a = Dipole spacing).

Multiple Gradient Array

Multiple Gradient refers to a variety of current electrode positions being used with dipoles of different sizes (Dahlin and Zhou, 2006). The transmitter electrodes (A and B) in the Multiple Gradient array, which can be seen in Figure 19, are always placed outside the receiver electrodes (M and N) and especially in this case beyond the area in which the receiver electrodes may be positioned or activated. The distance between the receiver electrodes is also denoted by "a". Consequently, the receiver electrodes maintain their constant spacing and are moved within the transmitter dipole, which is placed along a linear profile. Usually, the size of the current electrode dipole is about three to four times the size of the study area (Zonge et al., 2005). Similar to the other arrays, current I, voltage V and apparent resistivity ρ_a are measured. The geometry factor G in this case depends on the position of the electrodes (Dahlin and Zhou, 2006). The maximum penetration depth is greater than "AB/8", but decreases as the transmitter electrodes are moved progressively closer to the current electrodes. The Multiple Gradient array is widely used for tasks where good lateral resolution is favored over depth resolution. Structures in the subsurface, which are aligned vertically to the individual transmitter dipoles, may also be resolved well. Based on the experiments and measurements of Dahlin and Zhou (2004), the Multiple Gradient array is capable of producing an image quality comparable to that obtained with Pole-Dipole and Dipole-Dipole. Pole-Dipole and Multiple Gradient arrays compare well, especially when the two receiver electrodes are adjacent to a transmitter electrode and the second electrode is more separated from them (Dahlin and Zhou, 2006). Furthermore, the Multiple Gradient arrays are well applicable for the usage of multichannel data acquisition systems as it resolves the image adequately (Dahlin and Zhou, 2004). In addition, a higher density of measurement results can be obtained at a comparatively higher speed (Dahlin and Zhou, 2006). Nevertheless, in the absence of a multielectrode system, Multiple Gradient arrays are time-consuming (Zonge et al., 2005).



- Dipole spacing = a
- Distance between receiver and transmitter = n times a
- Penetration depth > AB/8
- Lateral resolution ~ a/2

Figure 19: Multiple Gradient array geometry and the respective characteristics (modified after Zonge et al., 2014). (Abbreviations: A, B = Current electrodes; M, N = Potential electrodes; ρ_a = apparent resistivity; V = Voltage; I = Current; G = Geometry factor; a = Dipole spacing).

6.3.5. Array Comparison

The capabilities of the individual configurations differ in terms of spatial resolution, penetration depth, and the potential to cause artifacts in the model (Oldenburg and Li, 1999). According to Sasaki (1992), Pole-Dipole configurations are particularly convenient as a balance between resolution and signal strength, whereas Dipole-Dipole is particularly opportune for resolving more detailed geological features. Preferably, configurations providing sufficient data coverage and a high signal-to-noise ratio, while being able to represent the occurring anomalies as accurately as possible with the measured data, are used. Multi-channel systems or multi-electrode cables are particularly suitable for this purpose, in which a constant electrode spacing is provided and different configurations can be measured continuously with different dipole spacings and without any great loss of time. Oftentimes the choice of configurations is a compromise, in order to contribute to sufficient data coverage and time management. However, a multitude of measured readings might make the inversion process more tedious and challenging (LaBreque et al., 1996). Dahlin and Zhou (2004) evaluated ten different electrode configurations, including the four used for this thesis. As part of their research, the arrays were examined based on their efficiency, as well as the effect of the parameters “a” and “n” on resolution. Figure 20 depicts the sensitivities of the four relevant arrays, along with the spacing parameters “a” and “n”, which are adjustable based on the required penetration depth and spatial resolution. Commonly, larger distances between the electrodes provide a greater penetration depth, whereas smaller spacings can be decisive for a better horizontal resolution. Dahlin and Zhou (2004) tested their electrode configurations on synthetic man-made subsurface models with an initial spacing of 1 m and a maximum separation of 60 m. However, these spacings are considered subjective and can be adjusted for the individual

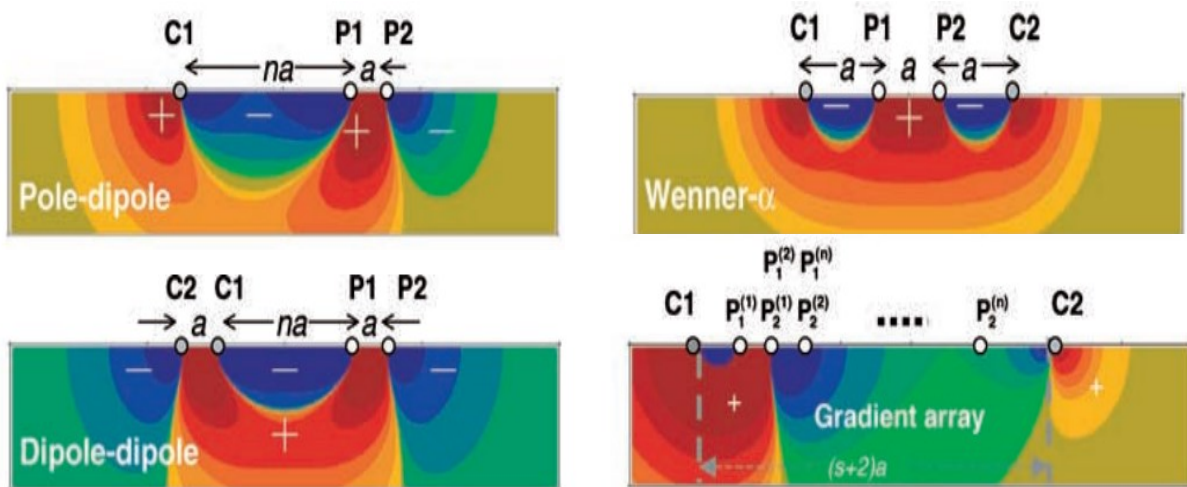


Figure 20: Schematic visualizations of the four used array configurations including their sensitivities (modified after Dahlin and Zhou, 2004). (Abbreviations: C = Current electrodes; P = Potential electrodes, a = Dipole spacing)

case and nonetheless reveal similar results. In addition to the electrode spacings, the properties of the subsurface also take a significant role in terms of penetration depth and resolution. More specifically, both the electrical properties and the geometry of a possible anomaly in the subsurface are influential. The anomaly effect, which should be at least larger than the background noise (Militer et al., 1979), is often used to assess the effectiveness of the resistivity measurements. Dahlin and Zhou (2004) have additionally discovered that the anomaly effect is strongly dependent on the geological model. Furthermore, by normal and reciprocal measurements of the individual measurement points, the correlation of the background noise with the observed potential of the array could be proven. According to Dahlin and Zhou (2004), Wenner-Alpha arrays are significantly less susceptible to random noise than Pole-Dipole, Dipole-Dipole, and Multiple Gradient arrays. The combined findings of the anomaly effects and noise contaminations indicate that Wenner-Alpha exhibits significantly better signal-to-noise ratios than the other configurations. Additionally, a further source of error is the three-dimensional behavior of the subsurface and its parameters, represented in this case only in 2D. Figure 21a illustrates a synthetic model (Dahlin and Zhou, 2004) of a conductive dyke ($50 \Omega\text{m}$) intruding into the high resistive bedrock ($1000 \Omega\text{m}$). The overburden is comprised of a coarse-grained sedimentary layer ($200 \Omega\text{m}$). The subsections (b) to (e) of Figure 21 depict the corresponding pseudosections of the

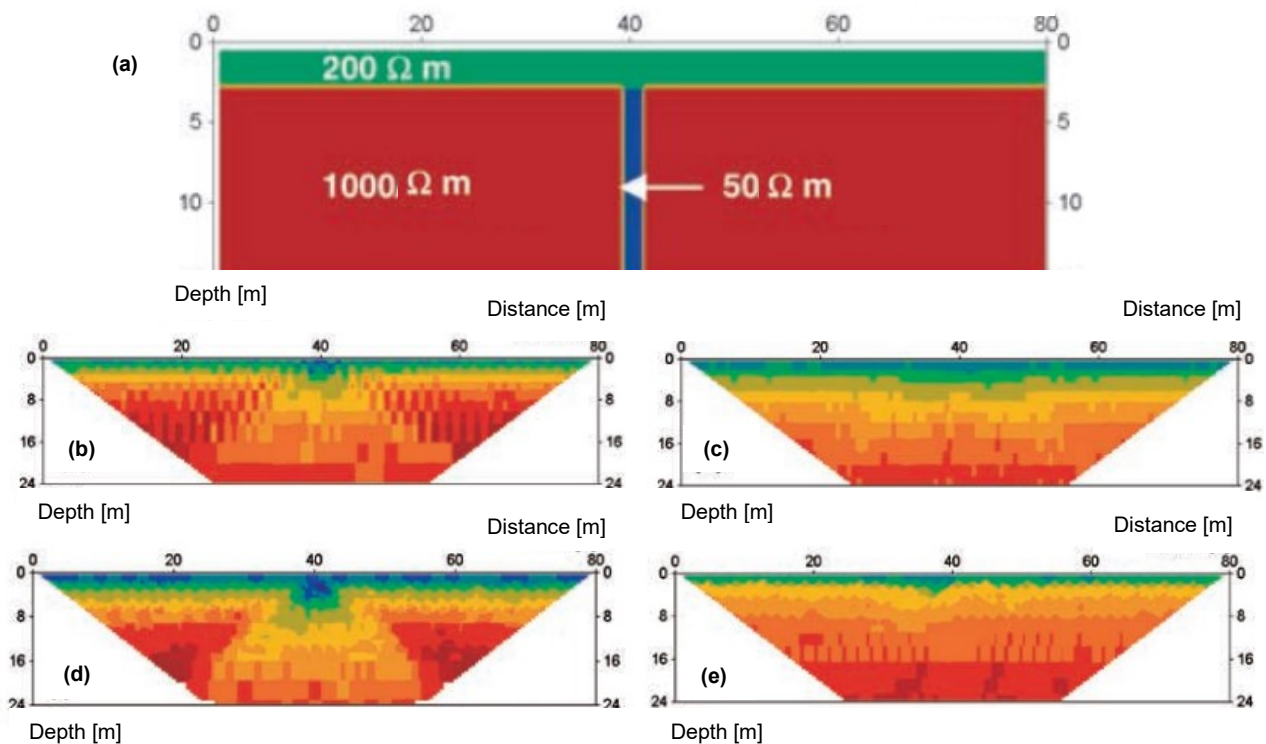


Figure 21: (a) Synthetic model of a dyke. (b) to (e) The pseudosections of the corresponding array configurations (b) Pole-Dipole array: (c) Wenner-Alpha array (d) Dipole-Dipole array (e) Multiple Gradient array (modified after Dahlin and Zhou, 2004)

apparent resistivities, obtained based on the model in (Figure 21a). Figure 22 shows the inverted results of the respective synthetic conductive dyke model, for which the robust L1-Norm has been used in order to generate these inversion models. The results obtained by the Dipole-Dipole configuration and those obtained by the Multiple Gradient arrays show better resolution and consequently a better image of the narrow conductive dyke. Similarly, the Pole-Dipole based result is relatively good and thus close to the previously discussed, also creating a clear and differentiated image of the dyke. In comparison, the Wenner-Alpha array generates a good image but produces noise both to the left and to the right of the narrow dyke. An Explanation might be the low signal-to-noise ratio for this specific synthetic model (Dahlin and Zhou, 2004). A second synthetically generated geologic model (Figure 23) represents a submerged river channel (200 Ωm) comprised of coarse-grained sediments. This synthetic buried river channel, reaching to a

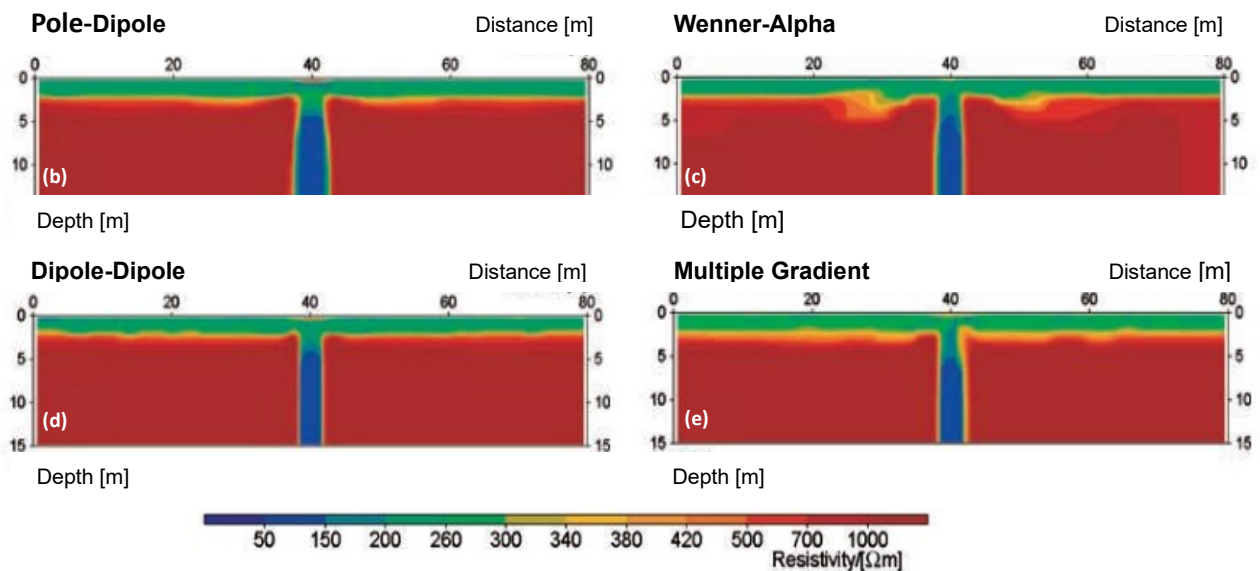


Figure 22: Models generated by the inversion of the different arrays. (b) Pole-Dipole array (c): Wenner-Alpha array (d): Dipole-Dipole array (e): Multiple Gradient array (modified after Dahlin and Zhou, 2004).

depth of 11 m, is situated in a low-resistivity environment (30 Ωm), indicating a clay-rich basement, overlain by a cover layer of silty material (70 Ωm). The models after the inversion process, using the L1-norm are displayed in Figures 23b to 23e. The results in this particular case are comparable to those in Figure 22, as both the Pole-Dipole and Multiple Gradient arrays show the highest resolution and produce the best image, in which the shape of the river channel is very well represented. The Dipole-Dipole array however compared to the other three arrays has a worse depth resolution, since a region with higher resistivities ($\sim 60 \Omega\text{m}$) around the river channel is created as an artifact during the inversion process. The trapezoidal shape of the river channel is not as accurately reproduced by the Wenner-Alpha array in comparison to the Dipole-Dipole, Multiple Gradient, or Pole-Dipole arrays. Even at relatively low noise levels and high signal-to-

noise ratios, the resolution of this electrode configuration is not able to reproduce the shape precisely (Dahlin and Zhou, 2004). A sequence of inclined blocks of sedimentary origin with different widths and alternating resistivities (100 Ωm and 300 Ωm , which is topped by a cover layer (200 Ωm), is represented in the model in Figure 24a. Figures 24b through 24e contain inversion results generated by using the less robust L2-Norm in this case. The images created with the robust L1-Norm were too blocky to resolve the dipping structures. Based on this geological

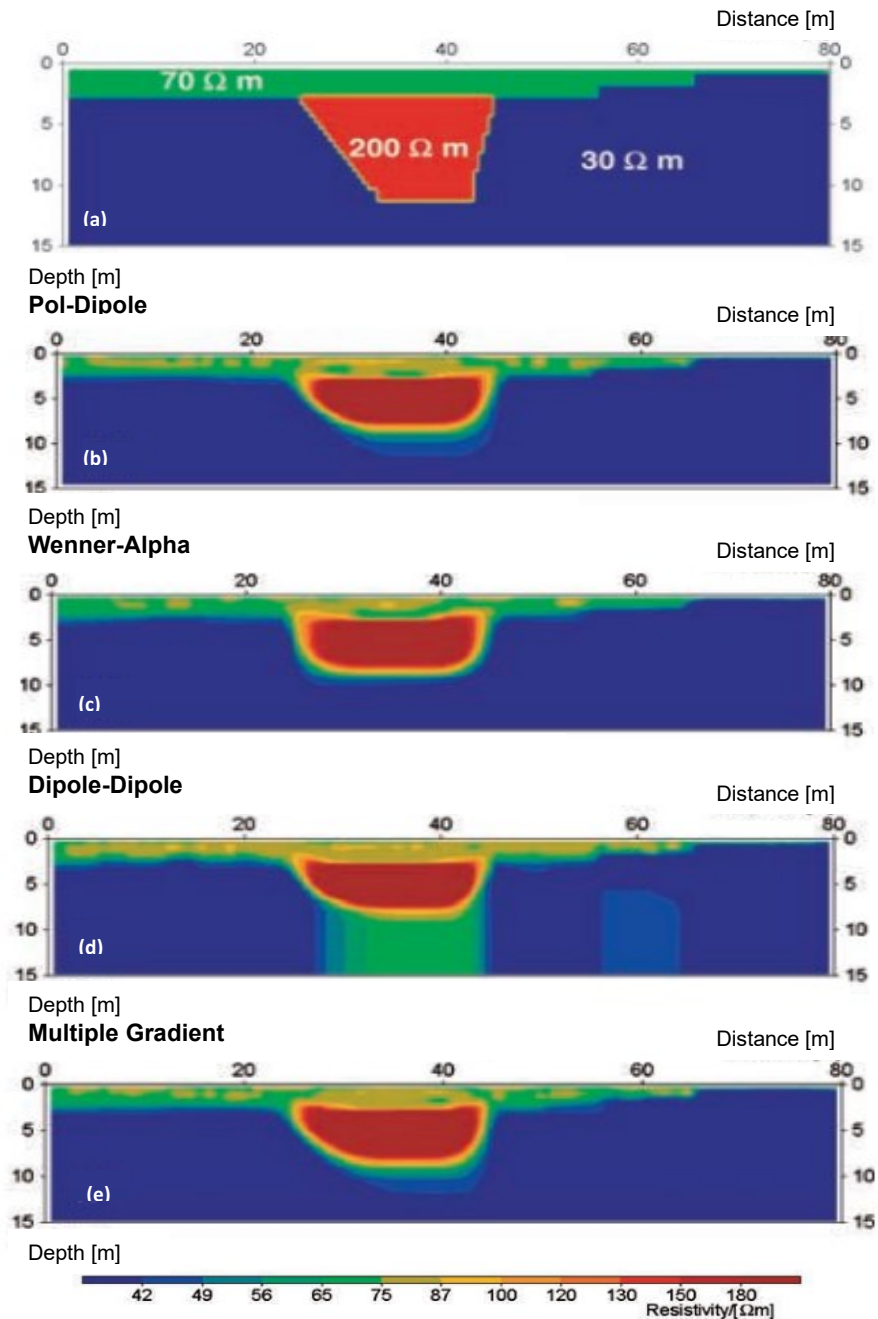


Figure 23: (a) Synthetic model of a river channel in a clay environment. (b) to (e): Inversion results (L1-Norm) of the respective arrays. (b) Pole-Dipole array (c): Wenner-Alpha array (d): Dipole-Dipole array (e): Multiple Gradient array (modified after Dahlin and Zhou, 2004).

example model and its inversion results, the Pole-Dipole and Dipole-Dipole arrays provide the best resolution of the structures, although minor artifacts due to the high noise levels are visible at lower depths. However, the Wenner-Alpha configuration produces a lower number of artifacts, due to the lower noise level. Nevertheless, the individual dipping structures are not resolved quite as well. Multiple Gradient arrays are between the previous ones in terms of resolution, better than Wenner-Alpha but not as good as Pole-Dipole or Dipole-Dipole. At a higher data density, the results of the latter and the Multiple Gradient arrays are converging (Dahlin and Zhou, 2004). The maximum penetration depth indicates the end of the zone (sensitive area) in which the structures in the subsurface can be efficiently resolved because of the available data. Beneath this depth, a good resolution is not possible anymore (Oldenburg and Li, 1999). According to Oldenburg and Li (1999), there are two possibilities to determine the penetration depth of a particular array, with both of them relying on different starting models. However, the software Res2DInv always assumes a homogeneous starting model. Nonetheless, by simple comparison, it is possible to recognize up to which depth structures can be resolved more accurately using a distinct array. All of this is described by the sensitive area and the poor-resolution area of the data, whereby the boundary between these two regions is the maximum penetration depth. Likewise, the section in

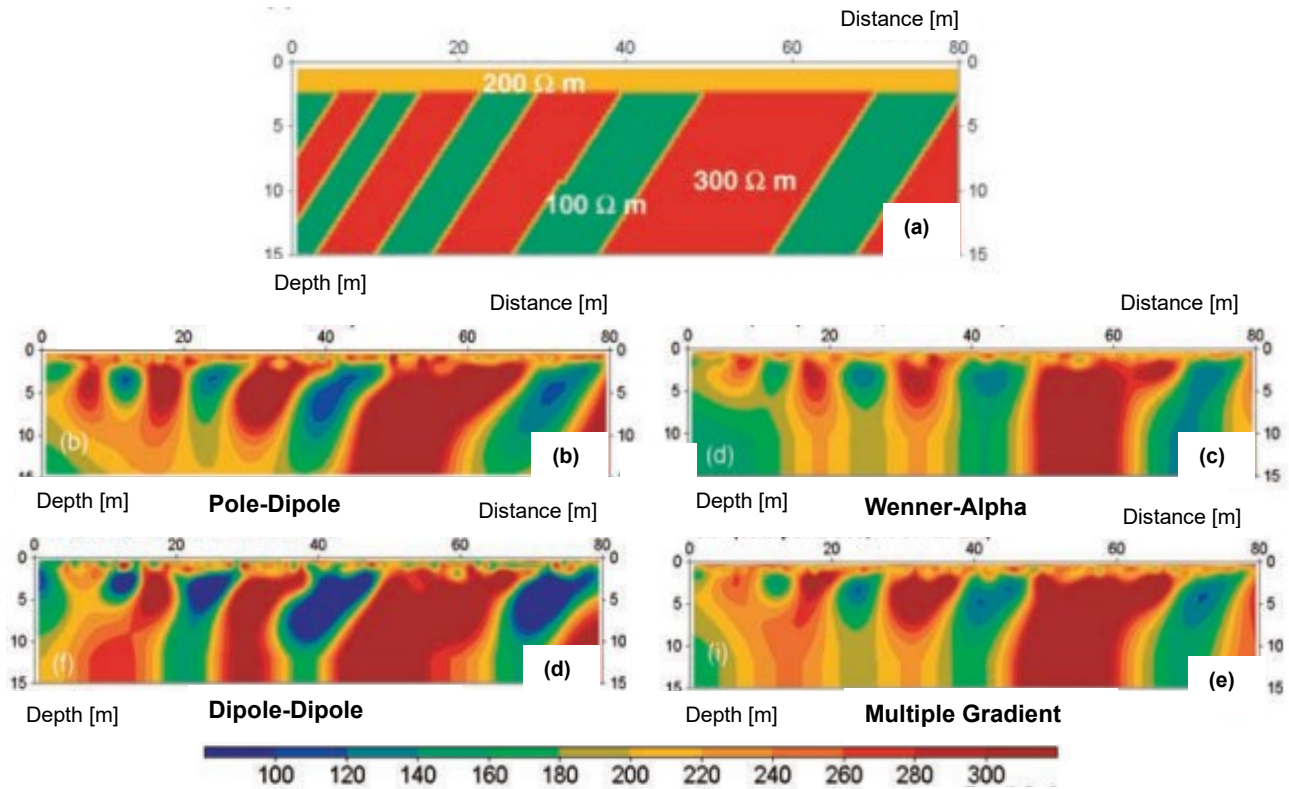


Figure 24: (a) Synthetic model of blocks of different thicknesses. (b) to (e): Models created using the L2-Norm for the four different arrays. (b) Pole-Dipole array: (c) Wenner-Alpha array (d): Dipole-Dipole array (e): Multiple Gradient array (modified after Dahlin and Zhou, 2004).

the lower left region of Figure 24 is significantly worse resolved than the lower right region, simply explained by the increasing thickness of the dipping structure (Dahlin and Zhou, 2004). The quality of the inversion result can be improved to a certain extent by combining the individual arrays or is at least as good as the result of the better-resolving arrays. Therefore, a combination of Wenner-Alpha and Dipole-Dipole or Dipole-Dipole and Pole-Dipole yields an image that is at least as good as that of the individual higher-resolving arrays. Based on the numerical analysis and the comparisons of the individual electrode configurations with each other by Dahlin and Zhou (2004), Pole-Dipole, Dipole-Dipole, and Multiple Gradient arrays are particularly suitable for measurements with multichannel instruments. Further, the selection of the appropriate array depends on the accessibility and the conditions of the survey area, the overall objective of the measurements, as well as the financial and logistical parameters. However, good parameters, such as high anomaly effect and high signal-to-noise ratio, achievable by Wenner-Alpha for example, do not guarantee a high-resolution image, as other limiting factors can have an immense impact on the resolution of the result (Dahlin and Zhou, 2004; Loke, 2021).

6.4. Vertical Electrical Sounding (VES)

Vertical electrical sounding is a one-dimensional resistivity surveying technique in which the central point of the electrode array remains fixed and only the electrode spacing increases. In the application of the VES, a horizontally structured subsurface is assumed, with the electrical properties only changing in vertical and not in horizontal direction. The main limitation of this measurement technique is the inability to detect lateral changes in electrical properties, which occur relatively frequently from a global perspective (Loke, 2021). The objective is to resolve the vertical variation of the subsurface electrical properties. Therefore, the measured parameters are usually plotted against the electrode separation or respectively the pseudo-depth (Dentith and Mudge, 2014). Focusing on deeper regions, basically all arrays are suitable for this purpose, however, the two most used arrays are Wenner and Schlumberger. In the former, the potential electrode spacing X_{MN} is changed at equal intervals between all electrodes around the center point, whereas in Schlumberger only the dipole of the current electrodes is enlarged. The magnitude of the dipole ranges from a few meters to several kilometers, depending on the target depth (Dentith and Mudge, 2014). Variations in the thickness and resistivity of the individual layer packages are the decisive parameters, as the electric current pursues the path of least resistance. The most common applications include the imaging of the layer structure and the investigation of the overburden (Pous et al., 1996).

6.5. Global Navigation Satellite System (GNSS)

The Global Navigation Satellite System, abbreviated GNSS, which includes satellite constellations such as Galileo (Europe), GPS (USA), GLONASS (Russia), and BeiDou (China), enables worldwide coverage (EUSPA, 2023). The system comprises a combination of numerous satellites, carrying signals from space and transferring both position and timing data to stationary GNSS receivers. This information is then used to establish the correct coordinates (IFACTA, 1999). Accuracy, integrity, continuity, and availability are the four main features that characterize the GNSS system. Exemplary for this are the exact difference between the measured and the real location, velocity, or time and an available tolerance limit for anomalous results (EUSPA, 2023).

7. Inversion

The primary premise of geophysical inversion is to find a model capable of producing the same response as the measured parameters in nature. This is an idealization of a subsurface section in which the model parameters correspond to the physical quantities derived from the measured data sets (Loke, 2021). The approximation of the synthetic data to the observed data is an iterative process in which a starting model is successively changed. The resistivity values, both apparent and model response, are often represented as logarithmic. The difference between observed data and model response is represented as the vector g (Equation 2a), where y is the data set observed

$$g=y-f \quad (a)$$

$$E=g^T g = \sum_{i=1}^n g_i^2 \quad (b)$$

$$J^T J \Delta q_i = J^T g \quad (c)$$

$$(J^T J + \lambda F) \Delta q_k = J^T g - \lambda F q_k \quad (d)$$

$$F = \alpha_x C_x^T C_x + \alpha_z C_z^T C_z \quad (e)$$

Equation 2: Individual steps required for the inversion equation (modified after Loke, 2021). Abbreviations: g =Difference between model response and observed data, y =Observed data; f =Model response; Δq = Model change vector; J =Jacobian matrix; λ =Damping factor; α =Weighting of the roughness; C =Roughness filter

and f is the model's response. In the least-squares optimization, which is also used by the software Res2DInv, a starting model is changed in such a way that the sum of the squared discrepancy vector is minimized (Equation 2b). For the reduction of these error values, the Gauss-Newton equation (Equation 2c) is applied (Lines and Treitel, 1984), where Δq is the model change vector and J is the Jacobian matrix. Oftentimes the classical least-squares equation alone, for example in the case of a badly chosen starting model, deviates seriously from the ideal model, and does not lead to a target-oriented result. In this case, a damping factor λ is introduced, which does not allow the values of Δq to become unrealistically large and thus limiting them (Loke, 2021). Nevertheless, even with this approach, especially in two-dimensional and three-dimensional applications where the number of model parameters can be enormous and therefore many cells must be present in the model, irregular and partly arbitrary distributions of high and low resistivity values can occur (Constable et al., 1987). A further modification step extends the Gauss-Newton least-squares equation by minimizing the spatial variation of the model variables. Equation 2d is described as a smoothness-constrained least-squares method. The parameters C_x and C_z represent the matrices of the roughness filters and α_x and α_z correspond to the respective weights of the roughness filters (Loke, 2021). By using this equation (Equation 2e), the squared spatial

changes are minimized. The result is a model with plain resistivity variations (Ellis and Oldenburg, 1994a).

7.1. Inversion software

7.2.1. Res2DInv

The publicly accessible software Res2DInv offers two inversion options by default, but different characteristics of the measured data can be emphasized or de-emphasized by subjectively changing the parameters (Loke and Dahlin, 2002; Loke, Acworth and Dahlin, 2003). Fundamentally, the more robust inversion (L1-Norm) is superior to the smoothness-constrained least-squares inversion (L2-Norm) since the L1-Norm seeks to create a model that minimizes the absolute values of the data misfit. Contrary to this, the L2-Norm attempts to generate a model that reduces the squares of the data misfit. Accordingly, the L2-Norm assigns considerably more weight to measurement points with a larger misfit, causing this inversion method to be more sensitive to outliers. A variety of experiments with synthetic and real data have shown that the robust L1-Norm is significantly less susceptible to random noise and therefore produces fewer artifacts within the inversion model (Dahlin and Zhou, 2004). The software calculates the deviations of the model parameters from the observed values based on Equation 2a - 2d. Rapid and accurate inversion results are produced, allowing visualization of the data. In this iterative process, several inversion results (four iterative approximations included in the free version of Res2DInv) are compared and a root-mean-square (RMS) error is calculated. By changing or decreasing the RMS error and several parameters, the inversion result can be further refined and a realistic subsurface model in accordance with observed geology can be produced (Loke, 2021).

7.2.2. Res1D

The program Res1D is a free software from the company Geotomo with which both inversion and forward modelling for electrical sounding surveys can be executed (Loke, 2001). The inversion method is a least-squares optimization (Lines and Treitel, 1984). The task of the inversion is to generate a 1D model with defined resistivities and thicknesses for the horizontal layers. These individual parameters result from the fit of the model response with the measured data. A starting model with predefined parameters is successively reduced to minimize the difference between measured and calculated data (Loke, 2001).

8. Geographic Information System (GIS)

Geographic Information Systems (GIS) are tools for storing, managing, and displaying spatial data as well as supporting spatial data analysis and interpretation (Maguire et al., 1991). The technology enables the possibility for geoscientific researchers to acquire precise geographic data with timely and spatial precision (Suluguru et al., 2019).

8.1. Quantum GIS (QGIS)

QGIS, developed in 2002, is an open-source geographic information system free to use compared to often expensive software packages such as ArcGIS. QGIS is suitable for the visualization of spatial patterns and their interconnection, as well as their analysis, allowing its use in various disciplines such as soil and water sciences, agriculture, urban planning, and many more (Flenniken et al., 2020). Compared to many other GIS software packages, QGIS is a voluntarily managed project that can be continuously improved by all participants (Flenniken et al., 2020).

9. Fieldwork and Data Processing

9.1. Permissions

The exact positions of the individual geophysical measurements and their profile locations in the survey area are displayed in Figure 29 in Chapter 9.4.3. Both the ERT and VES profiles are located on properties belonging to two different proprietors. The areas marked in red (Figure 25) represent the plots of land belonging to the ZWHS, whereas the remaining profile meters are on land owned by the PVA. Following a written request, both parties promised unconditional access to their sites, provided that non-invasive methods are used. Furthermore, the public paths, some of which had to be crossed with measurement instruments, are also unproblematic in terms of approval. Some of the PVA properties are used by local farmers as agricultural land to keep livestock. A possible measurement-related anomaly (see Chapter 10.2.) could be identified based on this information combined with further research and additional geophysical measurements.

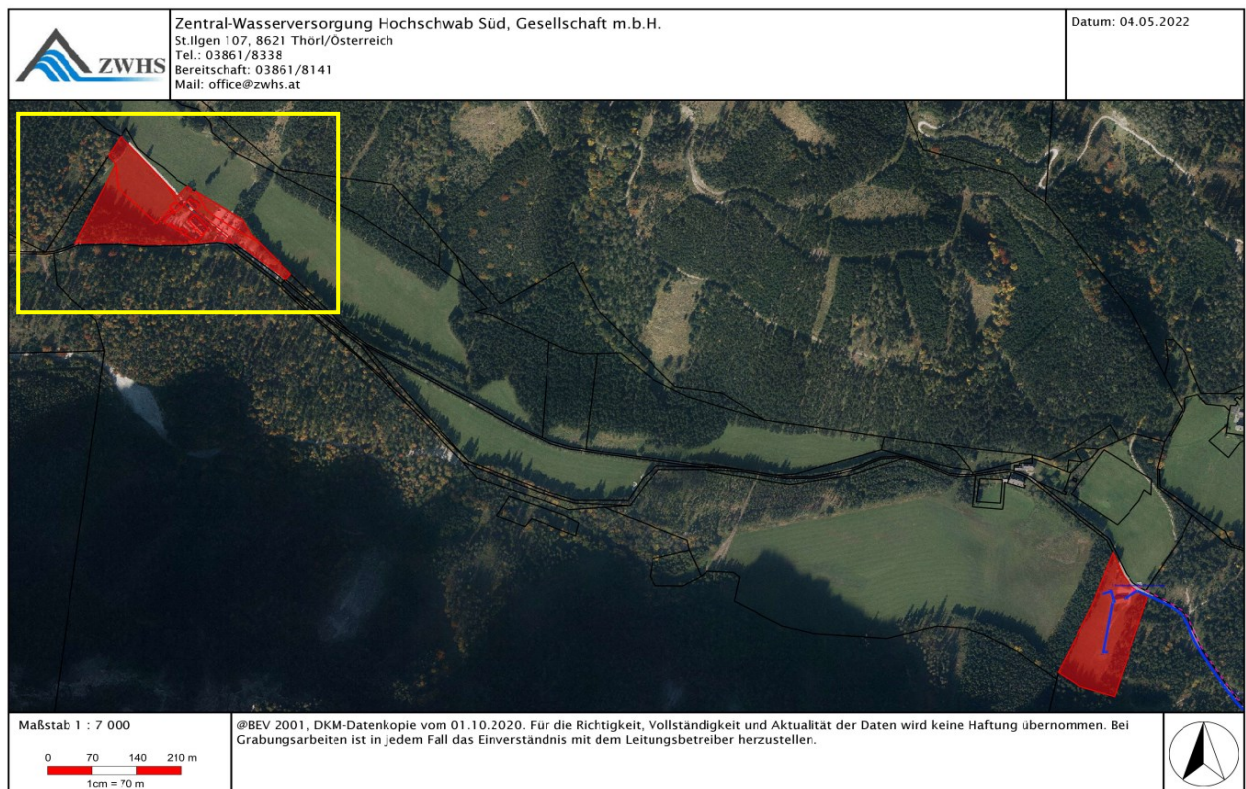


Figure 25: (a) PVA and ZWHS (red) are the two relevant proprietors in the study area. The yellow rectangle depicts the survey area (modified after ZWHS, 2022).

9.2. Measurement conditions

An initial inspection of the study area and the actual field measurements took place on different days. Table 3 provides an overview of the measurement conditions on the respective days of fieldwork. Despite the rapidly changing weather conditions, for which the Hochschwab is known, the measurement days were characterized by permanent dryness. Only the last 5 minutes of the depth sounding of the Hochschwab-Süd-Vertical electrical sounding01 (hs01ves) profile were interrupted by the onset of precipitation, which was not reflected in the results.

Table 3: All the measurement conditions related parameters.

Measurement date	Method	Measured profiles	Average Temp	Ground conditions
21.05.2022	ERT	hs01	23 °C	Dry ground
22.05.2022	ERT	hs02	20 °C	Dry ground
01.07.2022	VES	hs01ves, hs02ves	25 °C	Dry ground

Abbreviations: ERT = Electrical resistance tomography; VES = Vertical electrical sounding; hs01 = Hochschwab-Süd01, hs02 = Hochschwab-Süd02, hs01ves = Hochschwab-Süd-Vertical electrical sounding01; hs02ves = Hochschwab-Süd-Vertical electrical sounding02.

The contact between the spikes and the ground, verified by test measurements on the respective measurement days, was, despite the hot weather and dry conditions, good. It was only necessary to adjust one electrode due to its position on the dry gravel road.

9.3. Measurement devices

The GEODATA Group provided the equipment for the first two measurement days (ERT measurement), whereas VES measurements, on the other hand, were completed using equipment from the University of Leoben.

9.3.1. ERT device

The ARES II measuring device from the Czech company GF Instruments was used for the ERT. This multi-channel resistivity measuring device received its power supply from a generator. The measuring device under real conditions is shown in Figure 26a, with the explanation of the individual connections given in Figure 26b. Multielectrode cables and stainless-steel electrodes were laid out in the field and their precise position was measured as accurately as possible using GPS. A prefabricated set of electrode configurations from GEODATA Group, which includes Dipole-Dipole, Pole-Dipole, Wenner-Alpha and Multi-Gradient arrays has been used to measure the individual electrode configurations.

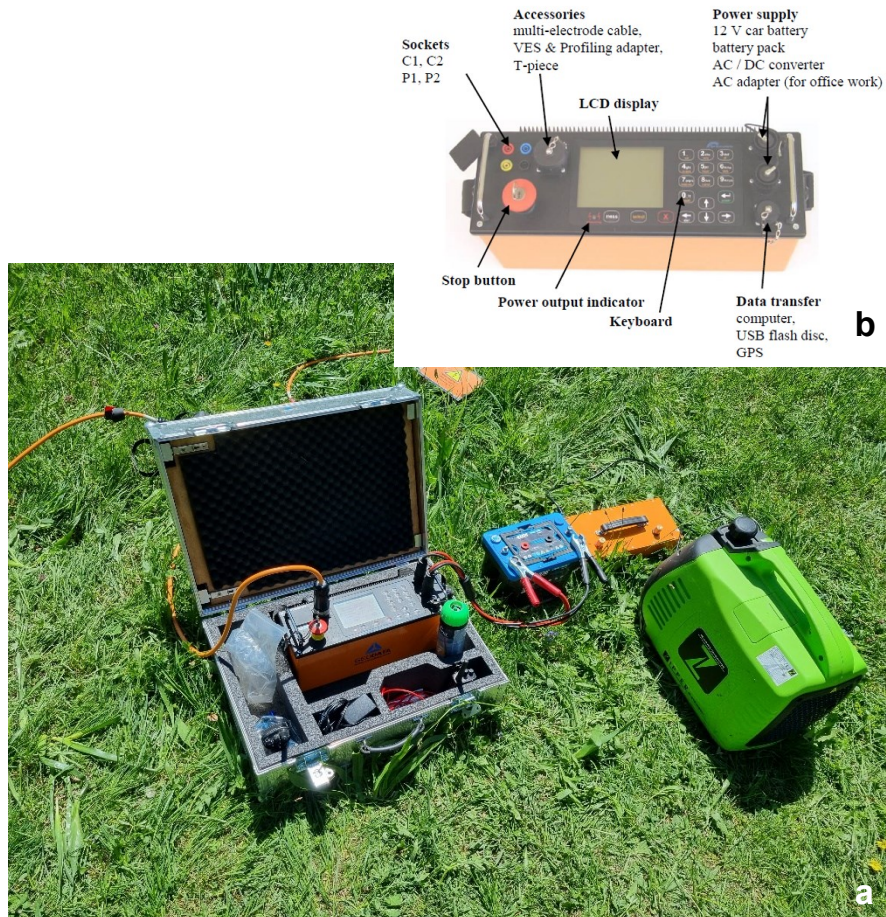


Figure 26: (a) ARES II during the fieldwork together with the power source. (b) Detailed explanation of the measurement unit (GF Instruments 2023).

9.3.2. VES device

The second resistivity measuring device is the STING R1 Earth Resistivity Meter from Advanced Geosciences Inc (AGI). This is a single-channel portable resistivity meter, powered by a 12V battery and the electrodes are stainless-steel electrodes. The deployment of the device in the field is shown in Figure 27a, together with the layout of the cables of profile (Figure 27b) Hochschwab-Süd-Vertical electrical sounding02 (hs02ves) in SW direction.

9.4. Measurement setup and procedure

9.4.1. Electrical Resistivity Tomography (ERT)

The first profile measured was hs01 (NW-SE oriented) followed by hs02 (SW-NE oriented) the next day. Measuring tapes were initially laid out on each respective day for both profiles and electrodes were hammered deep enough into the ground every 5.5 m in order to ensure good contact with the soil. Simultaneously, the cable strands were placed along the measuring tape for both profiles with a total length of 434.5 m. Once the spikes and cables had been positioned, an



Figure 27: (a) STING R1 under real conditions. (b) Beginning of the profile hs02ves in SW direction.

elastic band was used to secure them together. The individual cable harnesses were connected to each other as well as to the ARES II measuring device. The predefined measurement setup was started, after an initial testing of the contacts. This initial testing phase was necessary to determine whether sufficient current could penetrate into the ground. This procedure was repeated the following day for hs02.

9.4.2. Vertical electrical sounding (VES)

Starting with profile hs02ves, which runs parallel to hs02, the two VES profiles were both measured on the same day using the Schlumberger array. Initially, as with hs01ves, measuring tapes were again laid out for the first 50 m. The further course of the profiles had to be continued using GPS due to the required overall layout length of the measuring method. Difficulties were encountered in this case, particularly with hs02ves, as the morphology and topography led to a bend in the profile after 215 m in SW direction (highlighted in red in Figure 29). The total length of 464 m could not be reached in the NE direction either due to steep slopes. It is important to note that starting from a fixed central electrode, the electrodes are moved further apart in both directions along a straight line at the same relative distance



Figure 28: (a) Electrode layout for hs01ves in NW direction.

from each other. Appendix 15.3. shows the recording of the field measurement, in which the increase in the potential electrode distances and the current electrode distances are clearly visible. Profile hs01ves (Figure 28) was measured on the same day in the afternoon following the same procedure. However, the onset of minor precipitation during the last minutes of the measurement did not distort the result. The midpoints of the respective profiles are GPS point 17 for profile hs01ves and GPS point 8 for profile hs02ves (Figure 29).

9.4.3. Topographical measurement

A data collector from the company Trimble Geospatial was used in real-time kinematic (RTK) mode to determine the accurate position of the individual survey points. A major advantage offered by this mode is the data processing taking place directly in the field. In general, if a measurement is carried out in RTK mode, at least 5 satellites must be available. This turned out to be a minor problem in the Bodenbauer area, as some profile meters, especially for the hs02 and hs02ves profiles, are situated in the dense forest and additionally, the region itself is also known for poor satellite reception. Some of these GPS points had to be classified as unreliable, resulting in certain parts of the profiles being completed by interpolation between trustworthy measurement points. In general, however, the topography did not pose a major challenge.

9.4.3. Profiles

A total of four geoelectric profiles (2x ERT, 2x VES) were measured during this master's thesis, with an overview of the general data regarding the profiles provided in Table 4. The exact positions of the profiles are indicated in Figure 29. For each of the ERT profiles, 80 electrodes were deployed. The positions of the main profiles hs01 and hs02 are roughly comparable to the seismic profiles shot in 1971, which allows comparison, discussed in Chapter 11. The profiles hs01ves and hs02ves were selected in a manner such that they run approximately parallel to the main

Table 4: General information on all the profiles.

Name	Orientation	Total length [m]	Remarks	Colour coding
hs01	NW - SE	434.5	Remote electrode 181	yellow
hs02	SW - NE	434.5	Remote electrode 281	green
hs01ves	NW - SE	846		red 17-25 blue 2286-2291
hs02ves	SW - NE	836	Data usable up to GPS point 14	red 8-16 blue 2278-2285

Abbreviations: hs01 = Hochschwab-Süd01; hs02 = Hochschwab-Süd02; hs01ves = Hochschwab-Süd Vertical electrical sounding01; hoves02 = Hochschwab-Süd Vertical electrical sounding02; NW = North-West; SW = South-West; NE = North-East; SE = South-East.

profiles hs01 and hs02. The profiles were not superimposed on a geological map, as all profiles are located within the Quaternary sediments. The survey area is in the UTM 33N zone of the Universal Transverse Mercator (UTM) global coordinate system.



Figure 29: Position of the ERT profiles (hs01 in yellow and hs02 in green) and the VES profiles (hs01ves in red 17-25, blue 2286-2291 and hs02ves in red 8-16, blue 2278-2285). The remote electrodes for the Pole-Dipole measurements are in black. The Bodenbauer restaurant is marked with a brown dot. GPS points 15 and 16 (circled in red) depict the kink of the profile hs01ves.

9.5. Data Processing

9.5.1. ERT Data Processing

The main stages of data processing for the ERT measurements are described in the following.

Data quality

In the initial step, prior to loading the data into the software Res2DInv, the data is assessed for quality (Figure 30) and measurement errors (Table 5). A histogram (Figure 30) provides a better overview of the measured apparent resistivities. In this representation, the apparent resistivities are summarized in blocks of 100 Ωm each and plotted against their absolute abundances, in order to provide a quick overview of all resistivities. Figure 30a depicts the histogram of the Wenner-Alpha representation of profile hs01 and Figure 30b the diagram for Dipole-Dipole of profile hs02. In the histogram of profile hs01 (Figure 30a), it quickly emerges that most of the measured resistivities are between 500 and 700 Ωm , which corresponds well with the historical findings, in an initial quick interpretation step. Based on this preliminary data, water-bearing layers may also be present in the study area. Figure 30b, on the other hand, shows significantly higher resistivities on average, as most of them are in the range of 600 to 1000 Ωm and suggest a slightly different subsurface structure compared to hs01. The second stage of the quality analysis involved the

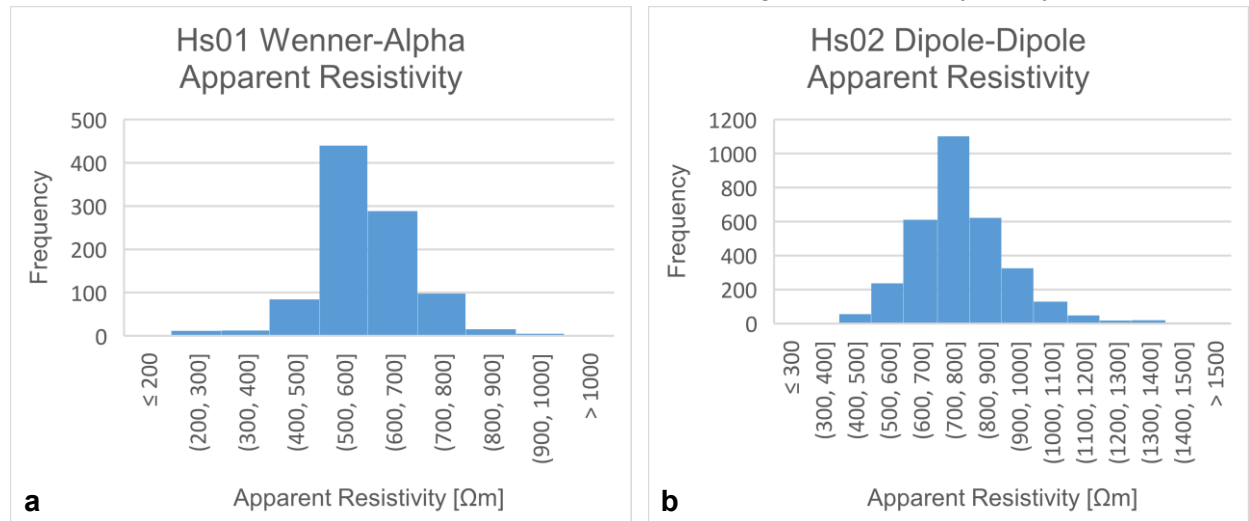


Figure 30: The measured apparent resistivities of (a) hs01 and (b) hs02 are compared to their corresponding frequencies.

inspection of the error of each individual measured value. Overall, the data quality is considered particularly good, which is evident from the ratio of measured values with a standard deviation $> 1\%$ in relation to the total number of data points (Table 5). For all arrays, except for the Multiple Gradient array, the ratio is less than 1% . Frequently with ERT, an increased number of errors $> 1\%$ can be recognized in the later, deeper measurement runs, which is presumably due to the larger electrode spacing. In these data sets, however, the standard deviations $> 1\%$ occur almost exclusively at the smallest electrode spacing.

Table 5: Comparison of the measurement errors of the individual arrays.

Standard deviation

	Hs01				Hs02			
	DD	WA	MGM	PD	DD	WA	MGM	PD
Total number of measurement points []	3194	954	3511	800	3194	962	3530	1624
Total number of measurement points with > 1% error	0	10	25	6	0	9	56	2
Ratio [%]	0	1,04	0,71	0,75	0	0,94	1,59	0,12

Abbreviations: *hs01* = Hochschwab-Süd01; *hs02* = Hochschwab-Süd02; *DD* = Dipole-Dipole; *WA* = Wenner-Alpha; *MGM* = Multiple Gradient; *PD* = Pole-Dipole.

Raw data analysis and evaluation

After the completion of the measurements and an initial quality assessment, the data is analyzed and processed in the following processing steps (Figure 31). This workflow is necessary to finally compare the measured apparent resistivities with the calculated resistivities in order to ensure the best possible statistical fit between the two as a basis to subsequently create a plausibly explainable geological model. The resulting model is a mathematical representation of the investigated subsurface, in which different physical model parameters, such as the measured apparent resistivities, are included. The software Res2DInv uses finite element- or finite difference methods, depending on the selected inversion technique, to approximate the calculated resistivities to the measured resistivities in several iteration steps until a certain error threshold is reached. Figure 31 displays the workflow for the ERT data from the evaluation of the raw data to the finished inversion result with an underlying and explainable geological model. After examining the raw data in a few initial inspection steps shortly after the measurement paired with the removal of any conspicuous outliers, the next task is to import these unfiltered data sets into the Res2DInv program.

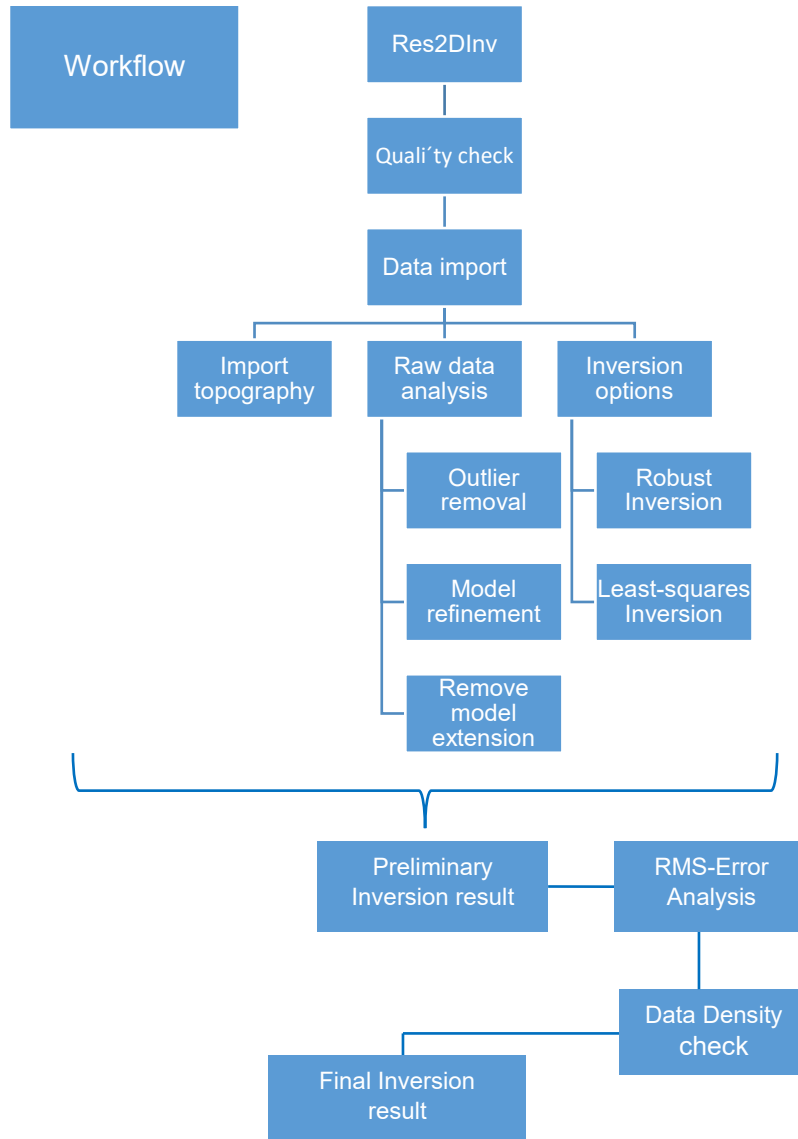


Figure 31: Evaluation workflow of geophysical profiles in Res2DInv.

In a second processing step within the software Res2DInv, the raw data is checked again for bad data points (outliers), subsequently resulting in the removal of them. There are many possible causes of poor readings, including insufficient contact between the electrodes and the dry surface, as well as moist ground conditions leading to a possible short circuit in the cable. Therefore, measured apparent resistivities either appear too high or too low in correlation with the neighboring data points and need to be removed from the data set. Figures 32a and 32b show the data window in which the bad measurement points are visualized and identified for the two profiles hs01 and hs02. The profile hs01 (Figure 32) measured with a Dipole-Dipole array has a few outliers (marked in red), which were subsequently removed from the data set. In addition, an "inverted V-shape" (pants-legs structure) is recognizable (highlighted in green), caused by an anomalous electrical

property that spreads diagonally into the depth due to the array geometry and which is discussed in more detail in Chapter 10.2. (Figure 43). Profile hs02, also plotted with the Dipole-Dipole array, reveals a nice data set with little to no bad data points that require removal (Figure 32b).

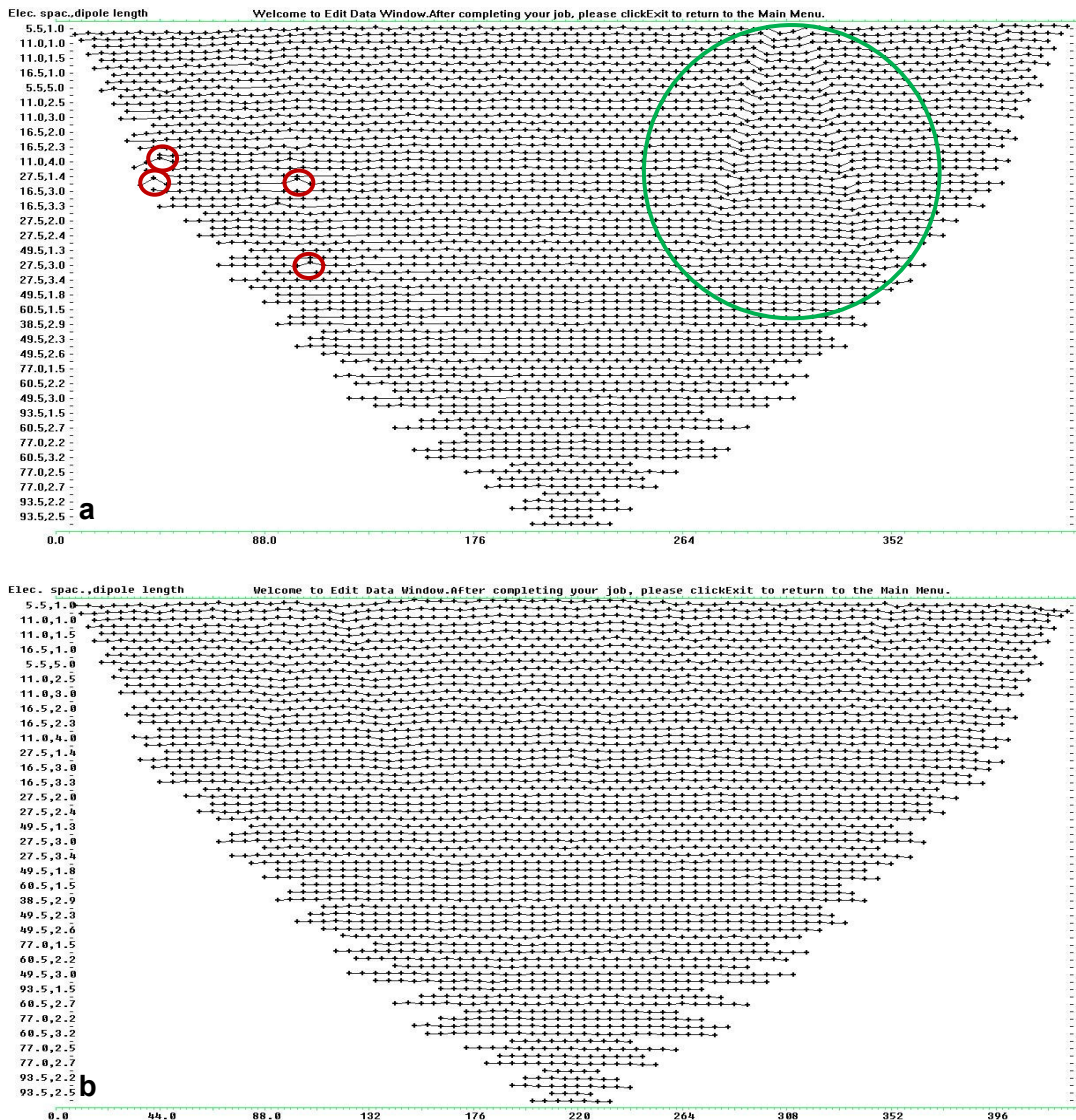


Figure 32: (a) Raw data of hs01 with anomalous data marked in red and green. (b) Raw data of hs02 shows nearly no outliers. Abbreviations: Elec.spac. = Electrode spacing.

Two further smaller processing steps are necessary prior to the selection of the inversion method. Firstly, during model refinement using the option "widths with half the unit spacing", the actual electrode spacing during the measurements is halved from 5.5 m to 2.75 m in order to generate a denser network. Therefore, the different resistivities close to the surface are easier to deal with. Additionally, this reduces the noise effects in the 1st and 2nd row of the data set. Furthermore, the option "use extended model" is set to "no" (Figure 33) so that the generation of information in

areas where no measured values are available, can be counteracted. The original trapezoidal shape would thus be transformed into a rectangular shape whose "new sections" would be filled with interpolated rather than measured data.

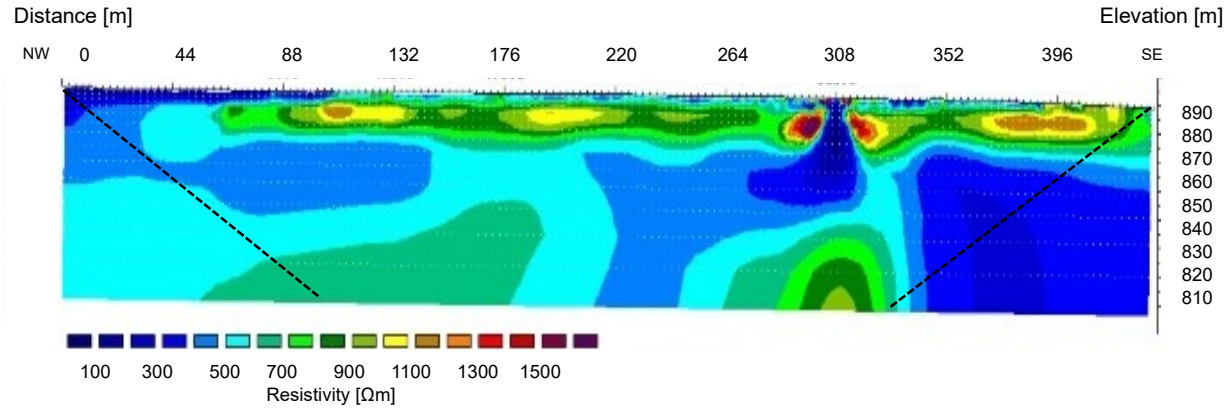


Figure 33: Profile hs01 without the trapezoidal shape (Black dashed line). In areas where no actual measured data points are available, interpolation processes are used, which can generate artifacts or potentially misleading results.

The topography of hs01 (Figure 34a) reveals a rise in the terrain towards the NW with a maximum difference of 8.1 m between electrode position 80 (434.5 m) and electrode position 0. Profile hs02 (Figure 34b), on the other hand, reflects a gradient of the terrain towards the SW with a peak difference of 19.1m. Nevertheless, the topography should not pose a major challenge but is still relevant for the comparison with the historical seismic data.

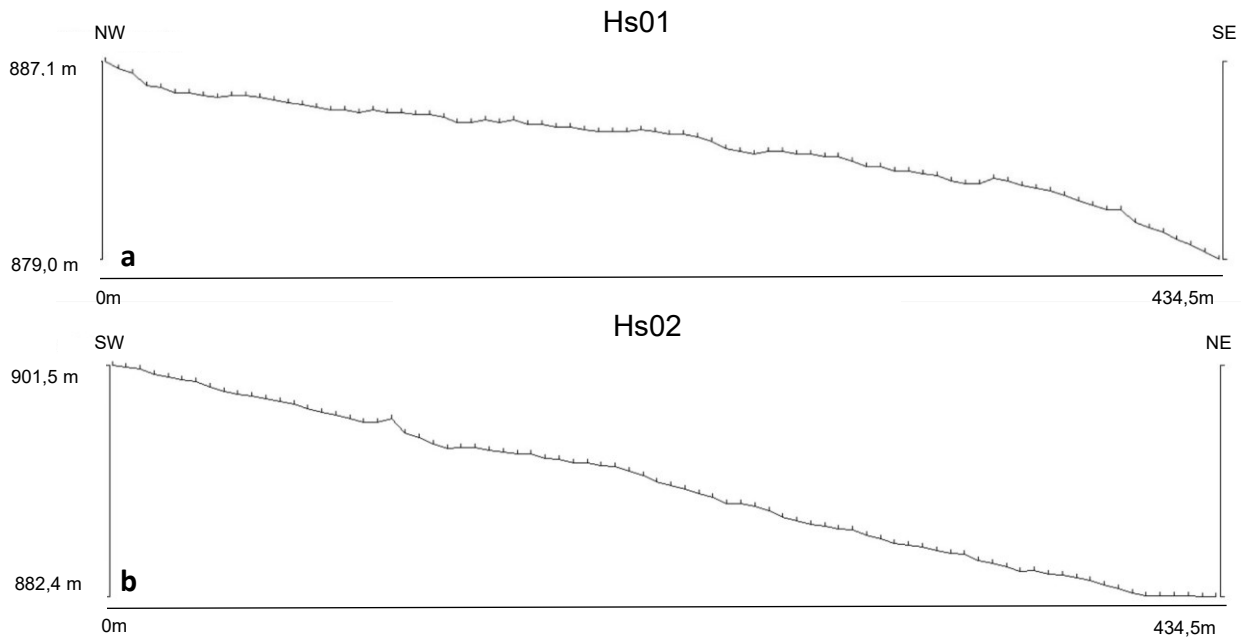


Figure 34: (a) The topography of hs01 is almost negligible. (b), whereas the topography of hs02 shows a maximum difference of nearly 20 m.

9.5.2. VES Data Processing

Raw data analysis and evaluation

The objective of the depth sounding was to determine the location of the bedrock at depth and to obtain an overview of the layer packages. After the measurements were completed, the data was further processed and analyzed in the following processing steps (Figure 35).

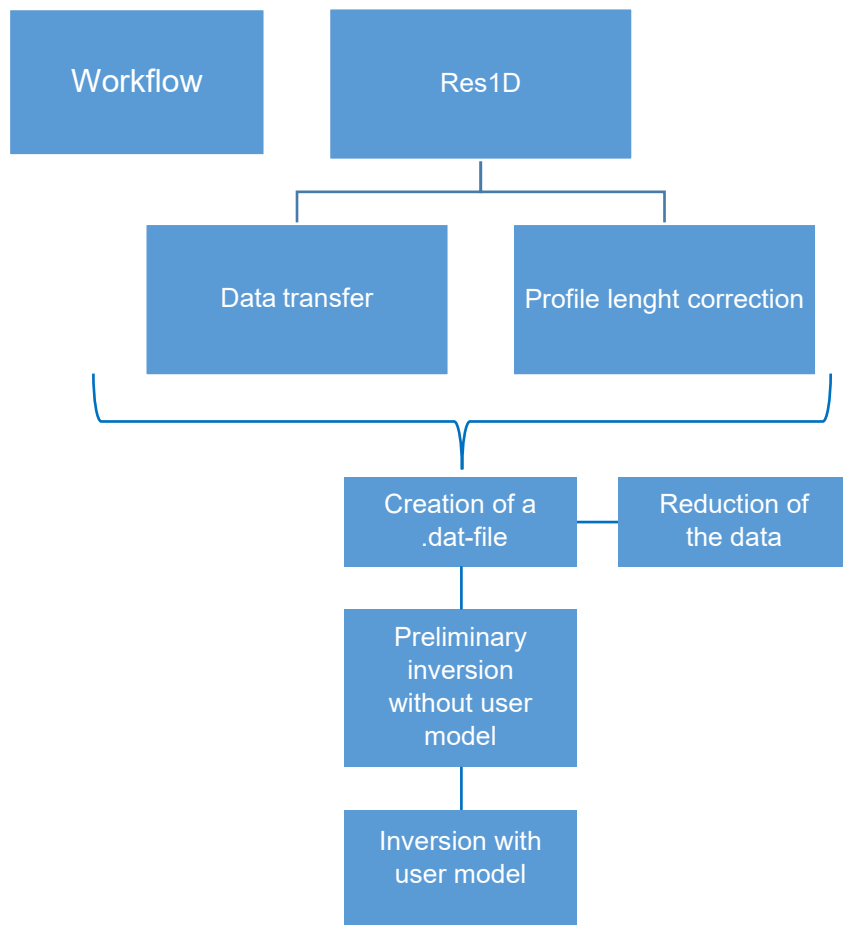


Figure 35: Evaluation workflow of geophysical profiles in Res1D.

The measured parameters, such as the current induced into the soil (Amperes and Milliampères) and the resulting measurable resistance (Ohm), were entered manually into a data sheet directly in the field after each individual measurement (Appendix 15.3.), which was then used to calculate the apparent electrical resistivity of the subsurface using the geometry factor for the Schlumberger array. An initial rough overview of the underground conditions encountered could thus be obtained directly in the field. Unfortunately, both profiles (hs01ves and hs02ves) could not be measured over the planned distance, as hs01ves was too densely covered with forest in the NW direction, which prevented a progression in a straight line, and hs02ves had to be shortened in both

directions due to the forest cover and the steepening topography. After appropriate correction for both profiles, the data records were converted into a .dat file, which is required for the software Res1D. The application of the Schlumberger arrangement provides two measurement results for each measurement point which must be reduced in order to use it in Res1D. Hence, it was divided into decades.

10. Results

The present work deals with the issue of the approximate depth at which the groundwater level in the Bodenbauer area can be expected, whether it has changed over the years since the last geophysical surveys, the structure of the basin fill, and if an aquifer is present in the hs02 cross-section. For this purpose, an ERT with different array configurations was performed and subsequently processed with various inversion methods in order to utilize the advantages of each. The aim of the VES was to obtain information about the actual thickness of the basin fill in the Bodenbauer area (hs01ves). For the cross-section hs02ves the determination of the bedrock depth, in a profile perpendicular to hs01, was a main target of the measurements. Furthermore, for profile hs01ves, the objective of reaching the bedrock could presumably not be achieved. Nevertheless, for hs02ves, it is open to interpretation whether the increased resistivity values already represent the bedrock, despite the shortened profile length and the therefore decreased penetration depth.

10.1. Inversion - ERT

The objective of the inversion is to determine a model in which the synthetic response matches the observed data in terms of parameters and settings to some degree of error (Dey and Morrison, 1979a; Silvester and Ferrari, 1990). The selection of the appropriate inversion method is largely based on the task and the available geological information. In principle, however, if the models created using the L1-Norm (robust) and L2-Norm (least-squares) match relatively well (Figure 36), the result should be good to display plausible geological data. The L2-Norm (Figure 36b) is relatively sensitive to outliers, as already mentioned in Chapter 7, whereas the L1-Norm (Figure 36a) is the more robust, which interpolates generously and therefore allows transitions between individual layers to be better identified. Nevertheless, not every small detail can be explained using the robust L1-Norm. Figures 36a and 36b are a comparison of the inversion results using the L1-Norm (Figure 36a) and the L2-Norm (Figure 36b) of profile hs01 measured with the Dipole-Dipole configuration. The L2-Norm is more sensitive to the abnormal data in the region of the "pants-leg" (marked in red), however, both methods provide relatively comparable results overall. The plausibility of the geological model must be considered too, during the selection of the appropriate iteration step. The Root-Mean-Square (RMS) error depicts the "success" of the inversion and delivers statistically the best result. Generally, where a flattening of the L-curve (Figure 37) occurs, the inversion should be terminated and the last iteration step carried out, should be selected as the most suitable. The geology could be falsified due to the creation of artifacts if the wrong iteration step is chosen. The area highlighted in red (Figure 37) indicates the flattening of the curve and identifies the iteration step that would be most appropriate for the inversion.

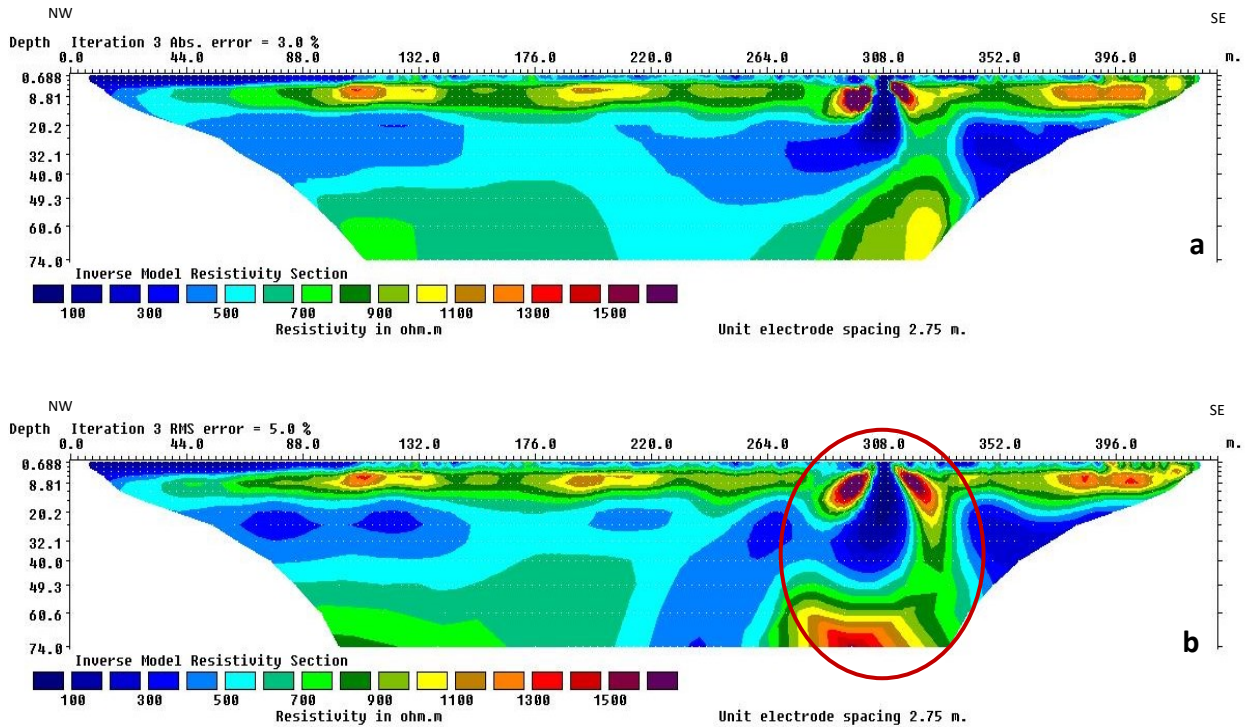


Figure 36: Comparison of the inversion results using (a) the more robust L1-Norm or (b) the more sensitive L2-Norm. The area circled in red indicates the clearly more sensitively resolved pants-leg using the L2-Norm.

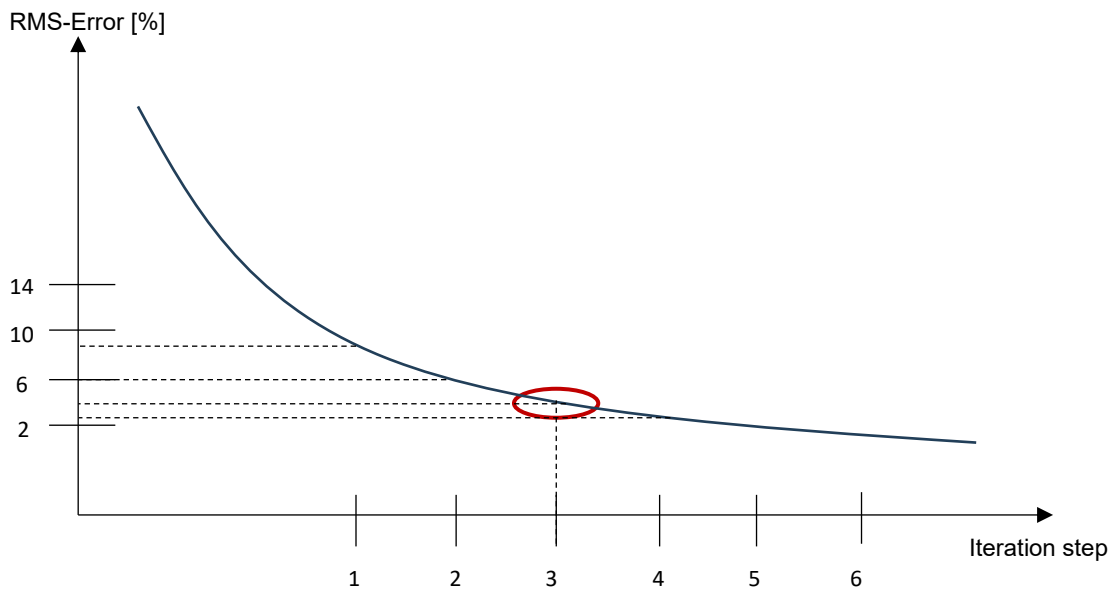


Figure 37: Correlation between the iteration steps and the RMS-Error in order to create a plausible geological model. The L-curve is shown for the inversion of hs01, and the red circle marks the last iteration step in which the reduction of the RMS error was sufficiently large.

RMS-Error Analysis

Figure 38 depicts the RMS statistics for the inversion of profile hs01. This statistic, displayed as a histogram, divides the data into different error classes from 0 to 180 %. If there is a lot of data in higher classes, either the measurement quality is questionable, or wrong parameters were

selected for the inversion. Certain threshold windows (Figure 38 in red) can be selected to filter out data that cannot be explained by the model. The inversion must be restarted in order to obtain a model with a better fit. It is particularly important to pay attention to the amount of data filtered out to prevent areas in the model with insufficient data density.

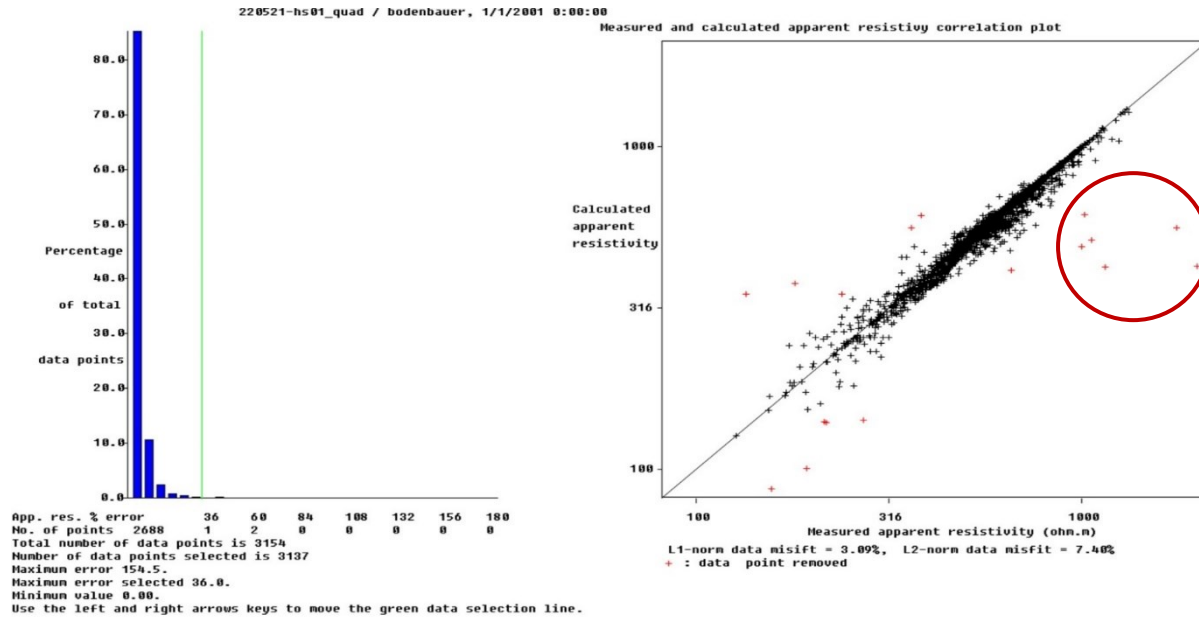


Figure 38: RMS-histogram of the inversion of the profile hs01. The area in red indicates data points that are removed within the next processing step, as these are too far away from the regression line.

10.2. Hs01

Profile hs01, like hs02, was measured with four different electrode arrays. The results of the individual configurations are relatively similar, as the interesting features are evident in all synthetic models, which is why the result of the Dipole-Dipole array is presented. In the third iteration step, the outcome of the inversion (Figure 39), which is used for the geological interpretation, was taken because the RMS error is already sufficiently low at 3% and it has not made a significant jump in a further step. Therefore, an additional iteration step would not be able to explain any resulting artifacts in a geologically meaningful way. The color scale runs linearly in steps of 100. In addition, the position of the first and last electrodes, together with the halved electrode spacing of 2.75 m are indicated in Figure 39. The elevation shown on the ordinate is the actual elevation and not a pseudo depth and the topography in the profile corresponds to the reality. The inversion provides a very nice and interpretable result. Generally, as already described by several authors (Fabiani et al., 1980; Schmid et al., 1980; Bauer and Lieb, 2011), a layered composition with, roughly divided, four different horizons is evident. A shallow conductive zone, followed by a bench with high resistivities, which is again underlain at a depth of 15 m (sea level 870 m) by another conductive layer with constant resistivity values. Finally, a high-resistivity layer is situated

underneath this horizon. In the NW of the profile, between 0 m and 80 m, a shallow layer with resistivities lower than the calcareous alpine groundwater was found, and which can be attributed, according to Schmid et al. (1980), to the lacustrine clays. Resistivities of this magnitude ($\pm 100 \Omega\text{m}$) only appear a second time at 308 m in Figure 39. The high-resistivity bench, starting at a depth of 885 m with an absolute thickness of 10-15 m, can be traced over almost the entire length of the profile and reaches resistivities of up to $1200 \Omega\text{m}$. The deposits are quaternary sediments, probably dry gravels. Based on the closely spaced isolines (marked by a black arrow) in the deeper part of this high-resistivity zone, a formation boundary can be expected, as the conductivities change rapidly at this point. The transition from the dry gravels to the more conductive, water-bearing gravels is anticipated at this depth. This 40 m thick layer with resistivity values between 300 and $600 \Omega\text{m}$ is the aquifer in this glacially shaped basin and corresponds lithologically to the water-bearing gravels according to Schmid et al. (1980). The area, circled in red in Figure 39, separates the conductive zones to the NW and SE of it and prevents communication between the two aquifers. This could be the result of the fault situated in this section according to the seismic results (Niesner, 1971). Another interesting area (marked with a red arrow) of the profile is between 370 m and 410 m at a depth of approx. 5 m, characterized by high resistivities ($>1000 \Omega\text{m}$). A comparison with the position of the profiles on an orthophoto (Appendix 15.4.) revealed forested ground at this position, therefore resulting in higher resistivities probably related to the dry forest soil.

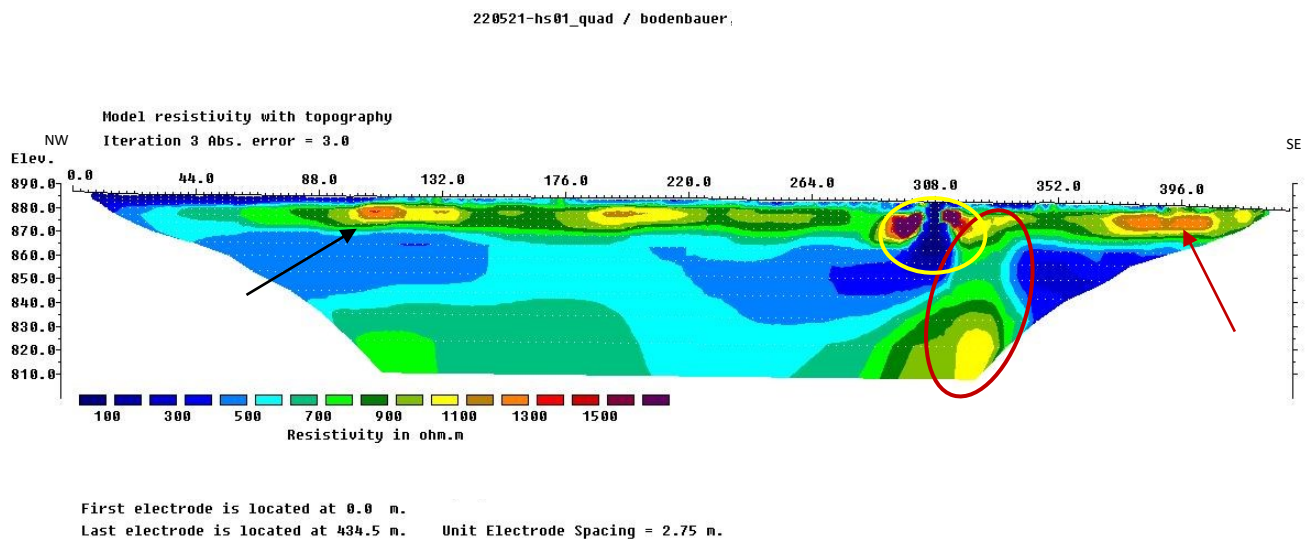


Figure 39: Inversion result of hs01 using the Dipole-Dipole array with some interesting features highlighted. The black arrow depicts the closely spaced isolines, indicating a layer boundary. The red arrow marks high resistivity values, which can be attributed to the dry forest floor. The area circled in red may indicate a fault at depth separating two aquifers. The yellow circle depicts the influence of the pants-leg.

The aforementioned "pants-leg" (yellow circle in Figure 39) is another phenomenon evident in this model. However, the origin of this result had to be clarified using another measurement method, namely geomagnetic, as it was suspected that it might have a non-geological origin. A new inspection of the study site led, at the edge of the study area near profile meters 300 to 315, to the discovery of a cattle drinking trough (Figure 40a) used to supply the seasonal livestock with water. Based on this visual information, a geomagnetic survey in NW-SE direction, was conducted over a length of 100 m, with a measuring distance of one meter. The result is a remanent magnetism, as only a monopole was detected, thus confirming the assumption of a metal pipe running in the shallow subsoil from the drinking trough in the direction of the well (Figure 40b) at the Bodenbauer restaurant. A possible trajectory of the pipe is indicated in Figure 40b as a black line. An additional conductivity measurement with a maximum penetration depth of 1.5 m was performed to get an impression of the conductivity of the pipe/body. The software Res2DInv provides the option of assigning an individually selectable resistivity to known anomalies, which are then placed at a specific depth at a precisely defined position with a cell of certain dimensions (schematically in Figure 41, circled in red in Figure 42). Figure 42 illustrates the result of the



Figure 40: (a) Cattle trough whose underground pipe creates an anomaly - front view. (b) View from behind the cattle trough to visualize the course of the pipe (black line).

inversion with a synthetic low-resistivity body (marked with a red circle) placed at the position of the "pants-leg", which was obtained from the raw data. The disappearance of the effect of the anomaly at depth (Altitude 880-840 m) is clearly visible compared to Figure 39. However, the most interesting result is the vanishing of the barrier or the effect of the fault, which separates the water-bearing gravel into two distinct parts (marked with a black circle in Figure 42). Separate compartments are not evident, and a uniform aquifer is present along the entire length of the profile.

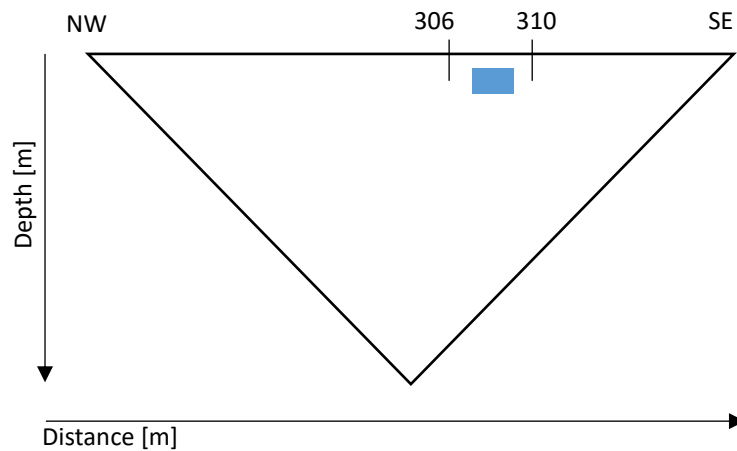


Figure 41: Exaggerated representation of the positioning of the low-resistivity body (blue rectangle). The resistivity of the "body" was set to 0.1 Ω m.

220521-hs01_quad / bodenbauer

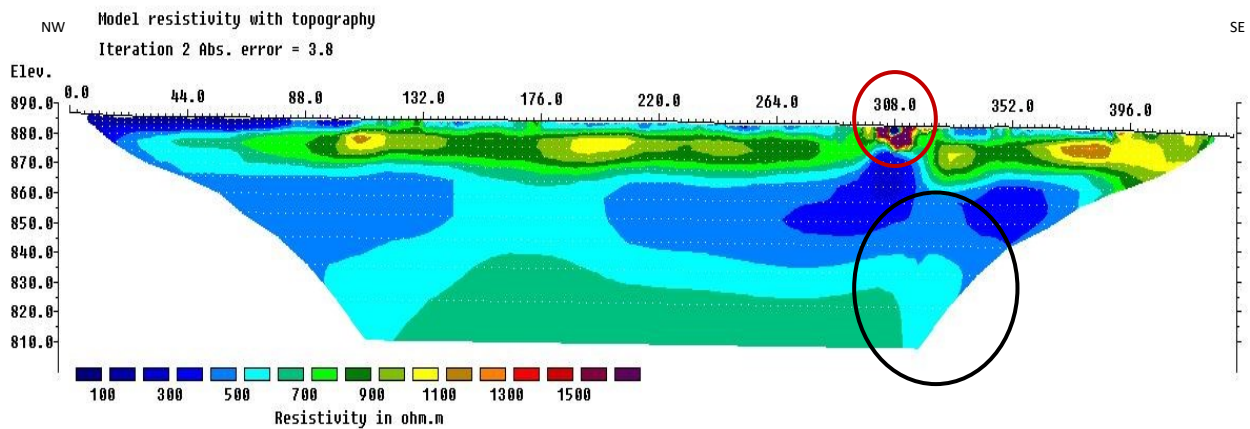


Figure 42: Inversion result of hs01 with a fixed anomaly placed at a predetermined position. The black circle outlines the no longer existing boundary between the two presumed aquifers and indicates a contiguous aquifer. The red circle marks the real position of the synthetically generated conductive body in profile hs01.

The aim of the survey conducted in this area was not only to identify the water-bearing layers and the height of the groundwater table but also to locate the depth of the pre-Quaternary bedrock. The software Res2DInv supports the combination of the results of different arrays and thus their advantages, which can subsequently be used to create a model via inversion. The result of a combined Pole-Dipole and Dipole-Dipole measurement (Figure 43) provides more depth information due to the Pole-Dipole array, paired with the high resolution of the Dipole-Dipole array, resulting in a good and plausible geological model. Although the model coincides quite accurately with the images (Figures 40 and 43) previously displayed, it contains more depth information extending to an altitude of 760 m. The layered nature of the basin remains apparent, as does the aquifer below a higher-ohmic bench. The difference to Figure 39 is the absence of the barrier that prevents the aquifers from interacting. This result is more consistent with the low-resistivity body placed in the raw data in Figure 42. However, the additional depth information indicates that the bedrock has not yet been encountered and the thickness of the basin fill exceeds 140m.

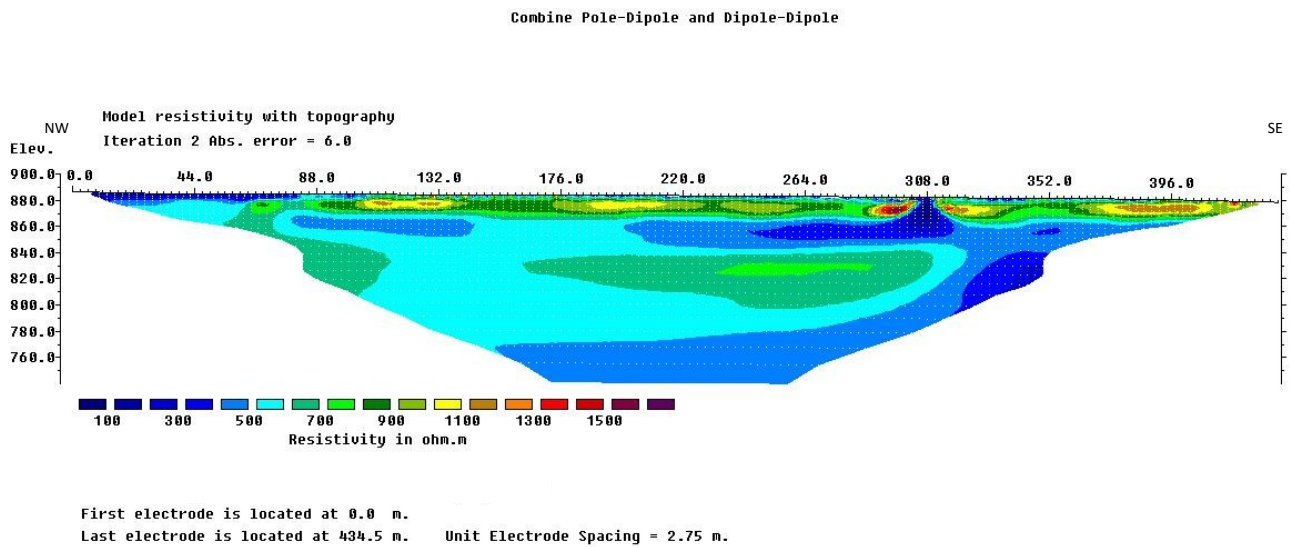


Figure 43: Model showing the inversion result of a combination of two arrays (Pole-Dipole and Dipole-Dipole) for hs01.

10.3. Hs02

Profile hs02, extending perpendicularly to profile hs01, also aimed to discover possible water-bearing horizons as well as the depth of the bedrock. This profile departs from the presumed basin (hs01) in a SW direction, therefore a slightly different subsurface structure could have been expected. The second iteration step already yielded the desired outcome (Figure 44), as the RMS error has already fallen to 2 %, resulting in a statistically good model. The slightly steeper topography is also noticeable, although this merely accounts for a maximum height difference of 20 m at ground level. A conductive area with resistivity values between 400 and 500 Ωm appears in the SW of the profile between profile positions 10 m and 28 m. This may be due to the influence of the runoff/drainage from the Joserbach stream running to the southwest. The profile crosses gravel roads and hiking paths at several points (marked with black circles and improved details in Figure 44), whose exact position have been confirmed by GPS and which is characterized by higher resistivity values than the surrounding area. In the region marked with a black rectangle, significantly higher resistivity values were recorded in comparison to the entire profile. Since this area is situated in the middle of a dense forest, the high resistivities probably arise as a consequence of the extremely dry forest floor. The layered structure, clearly identifiable in the basin (hs01), however, is not as good recognizable in hs02. Most of the lithology (greenish colors) visible in this profile is probably made up of unconsolidated sediments, such as layers of sand and gravel, extending across the entire profile and whose resistivity values (800-1000 Ωm) are roughly comparable to those in profile hs01. The red arrow marks the intersection of the two profiles with

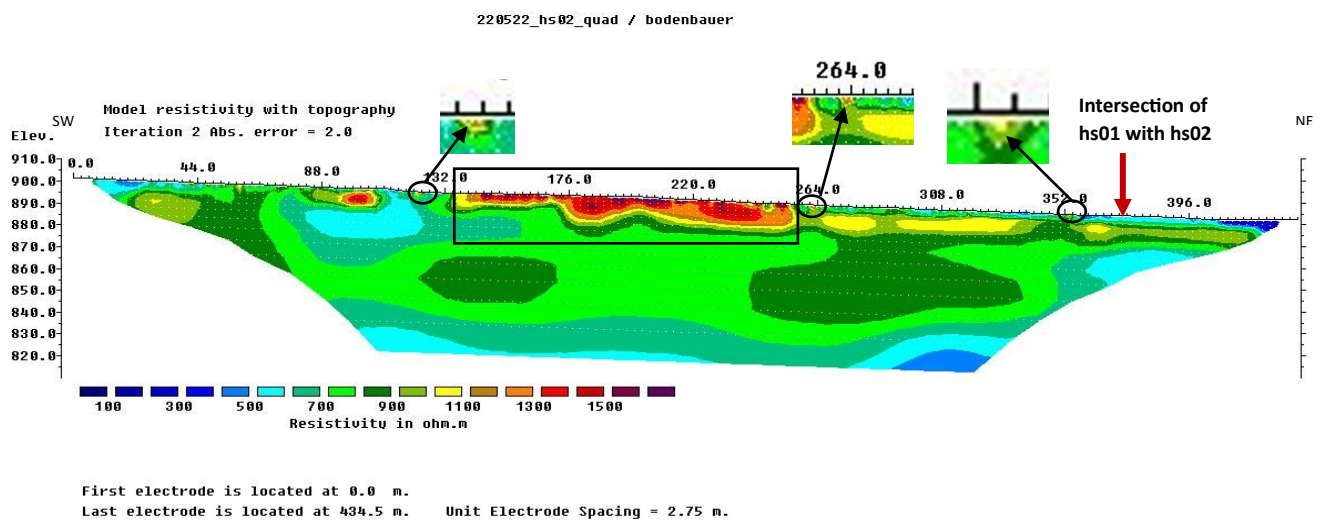


Figure 44: Inversion result of the Dipole-Dipole array for hs02. The black circles represent areas with higher resistivities, indicating gravel paths based on comparisons with orthophotography. The black rectangle highlights a high resistivity zone, characteristic for the dry forest floor.

each other and shows a good correlation of the conductive layer, first detected in hs01 at a depth of 15 to 20 m and which is also present at the same depth in hs02.

A combination of two electrode arrays (Figure 45) was implemented as well for this profile, in order to obtain more depth information. As before, the raw data from the Pole-Dipole and Dipole-Dipole arrays have been linked together. The additional insight gained at depths of more than 60 m shows a possible traceability of the water-bearing gravels at the levels, known from hs01, originating from the NE much further to the SW than previously assumed. The dry gravels ($\geq 700 \Omega\text{m}$) continue to occur from electrode 32 (profile position 176 m) in a SW direction towards the beginning of the profile.

All the gathered inversion results, as well as the comparisons between the measured and calculated models, are shown in Appendix 15.5.

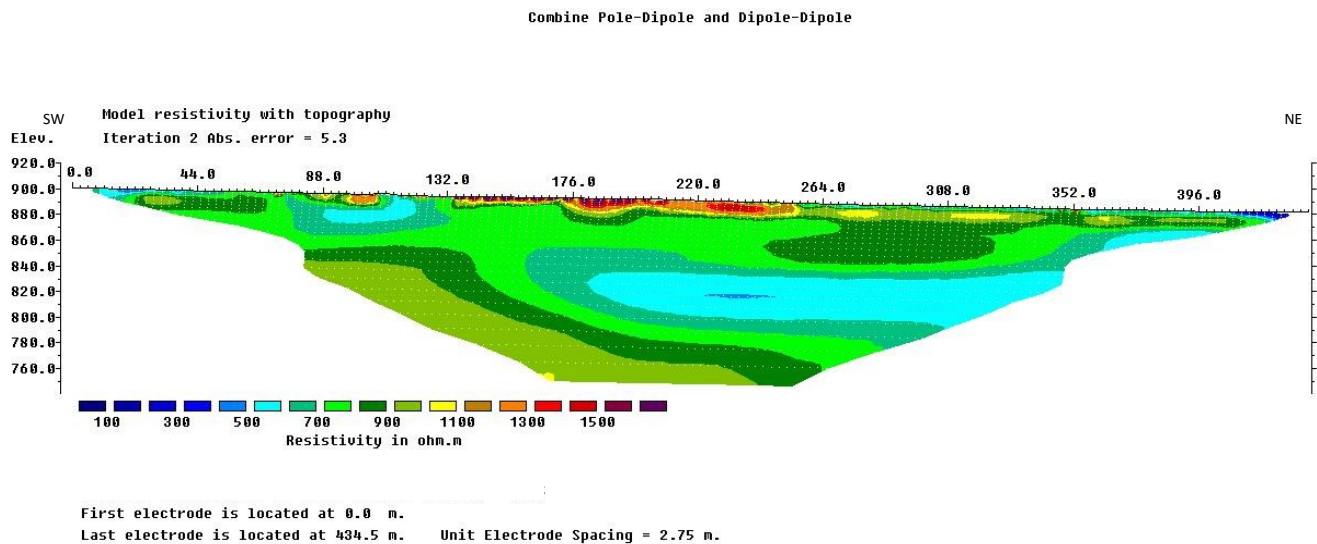


Figure 45: Inversion result after the combination of the Pole-Dipole and Dipole-Dipole array.

Array Comparison

The three electrode arrays Wenner-Alpha (Figure 46a), Dipole-Dipole (Figure 46b) and Multiple Gradient (Figure 46c) are plotted against each other and subsequently, their differences are analyzed. A satisfactory result for all three was obtained from the third iteration step and the inversion was performed based on the robust L1-Norm. Overall, the more accurate and sharper resolution is evident in Figures 46b and 46c, which is one of the advantages of Dipole-Dipole and Multiple Gradient array over Wenner-Alpha. Wenner-Alpha (Figure 46a), on the other hand, as the most robust of the three, produces a less sharp and smoother model, in which individual structures are not so much differentiated. The fault, detected at depth by refraction seismic (Niesner, 1971), can only be recognized as a slimmer structure in the more sensitive arrays, especially in Dipole-

Dipole, but also in Multiple Gradient (outlined in red), yet is completely absent in Wenner-Alpha. The first high-resistivity layer, interpreted as dry unconsolidated sediments, is also clearly more comparable in 46b and 46c and distinguishes between different resistivity ranges. The sharper depth resolution, supposed to be an advantage of Wenner-Alpha, yields similar results in all three images.

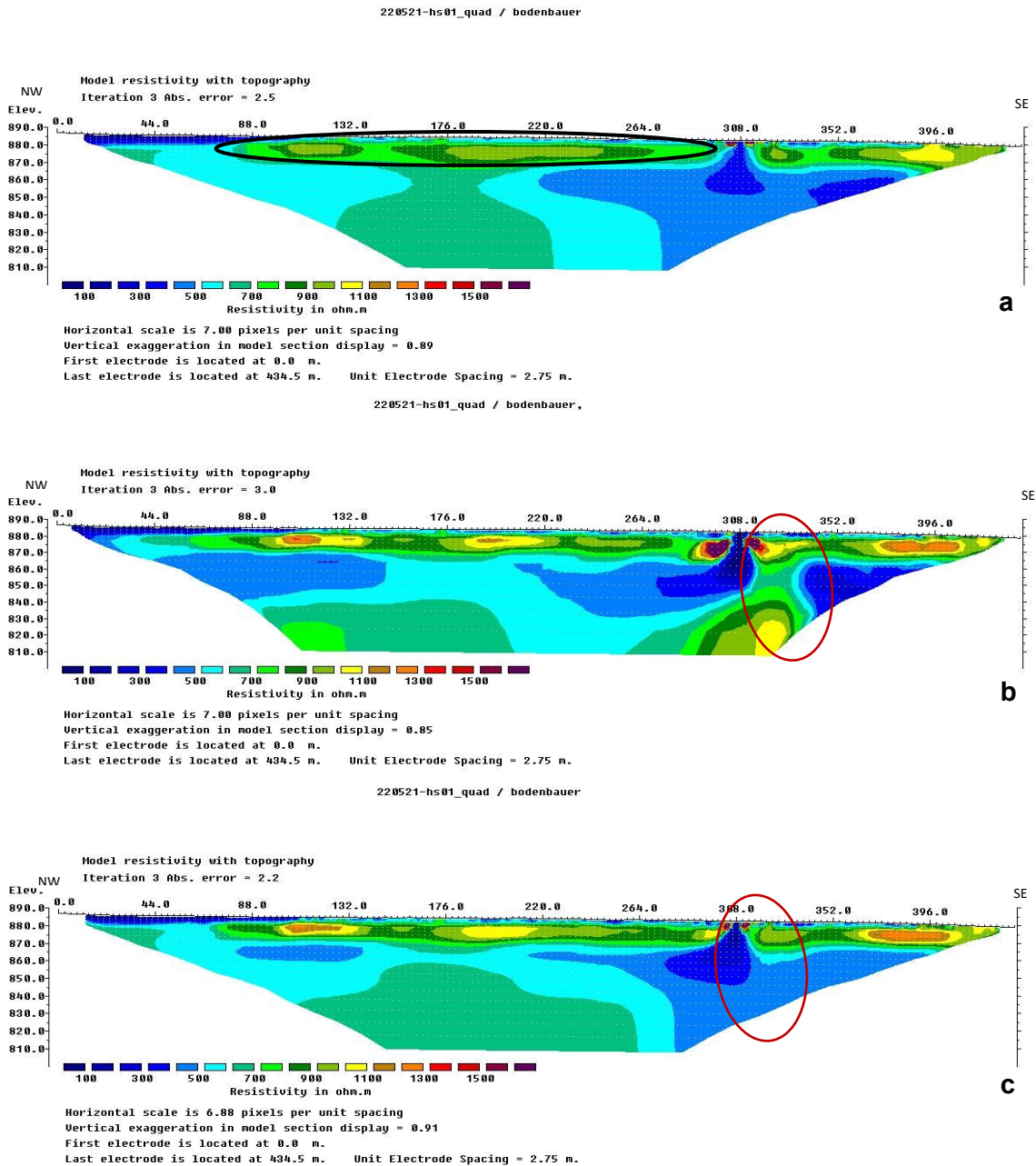


Figure 46: A Comparison of the inversion results of three different arrays. Wenner-Alpha array is the least sensitive configuration and does not reproduce fine differences (black area) as clearly as in the (b) Dipole-Dipole and (c) Multiple Gradient arrays. On the other hand, it is not as sensitive to finer structures, as can be seen in the example of the fault (marked in red). Abbreviations: Elev = Elevation.

10.4. Inversion - VES

17 measurement points with the corresponding apparent resistivities are shown in Figure 47a. The option "no starting model" enables the software to find a solution in which the observed apparent resistivities match the calculated apparent resistivities as closely as possible and in the end uses this information to construct a layered model of the subsurface. The inversion ends when the reduction of the RMS-Error per iteration falls below a predefined threshold value. The fit (Figure 47b), indicated by the low RMS-error, between the observed apparent resistivities (black plus signs) and the calculated apparent resistivities (black continuous line) was very good in the inversion step without a user model, although it predicted many thin layer packages. Based on this first preliminary solution, the input panel marked in red can be individually adapted, enabling a reduction of the number of layer packages determined by the software. Therefore, several smaller packages can be merged into fewer larger ones with similar apparent resistivities.

Schlumberger test
Schlumberger array
Number of datum points is 17
Resistivity

Error in measurements not available.

No.	a Spac.	b Spac.	App. Res.
1	1.00	146.53	
2	1.47	196.02	
3	2.16	270.28	
4	3.16	351.38	
5	4.64	472.74	
6	6.81	581.52	
7	10.00	622.35	
8	14.70	686.22	
9	21.50	712.07	
10	31.60	704.04	
11	46.40	650.21	
12	68.10	589.29	
13	100.00	526.15	
14	147.00	533.92	
15	215.00	634.13	
16	316.00	802.84	
17	423.00	837.64	

User Starting Model Available [Yes/No]
No

a

Enter user model

Enter the parameters of your model here.

Number of layers (2 to 9):

Resistivity and thickness of layers

Layer	Resistivity	Thickness
1	<input type="text"/>	<input type="text"/>
2	<input type="text"/>	<input type="text"/>
3	<input type="text"/>	<input type="text"/>
4	<input type="text"/>	<input type="text"/>
5	<input type="text"/>	<input type="text"/>
6	<input type="text"/>	<input type="text"/>
7	<input type="text"/>	<input type="text"/>
8	<input type="text"/>	<input type="text"/>
8	<input type="text"/>	<input type="text"/>

OK Cancel

You can use the model with many layers on the right obtained by the automatic inversion subroutine as a guide to select the number of model layers, as well as estimate the thickness and resistivity of the layers.

Remember that the depth scale for the depth of the model layers is given on top horizontal line.

b

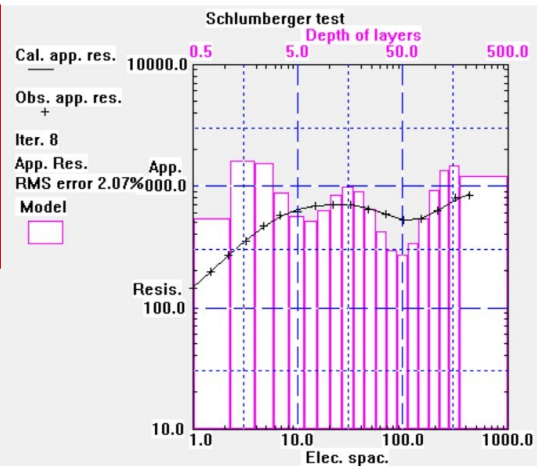


Figure 47: (a) Number of measurement points, $AB/2$ and the apparent resistivity. (b) First inversion result (black rectangle) without a user model and the chance to manually adapt the layer case (red rectangle).

Abbreviations: Calc.app.res. = Calculated apparent resistivities; Obs.app.res = Observed apparent resistivities; Iter. = Iteration; App.Res. = Apparent resistivity; Elec.spac = Electrode spacing.

10.5. Hs01ves

Figure 48 depicts the result of the inversion of profile hs01ves, in which the progressive inversion process was aborted at the 8th iteration step, as the RMS error was already relatively low, and no further improvement could be achieved. The fit between the measured data (black plus signs), and the calculated values (black continuous line), is very good but does not yet allow any conclusions to be drawn about the plausibility of the geological model, as this still needs to be compared with the existing data. A more detailed analysis of the data shows six sets of layers with different resistivities. The uppermost layer with an approximate thickness of 0.5 m and a resistivity of 100 Ωm is a thin cover stratum, which has good conductivity despite the dry weather and is probably the moist uppermost horizon of the pasture (surface soil). In the underlying

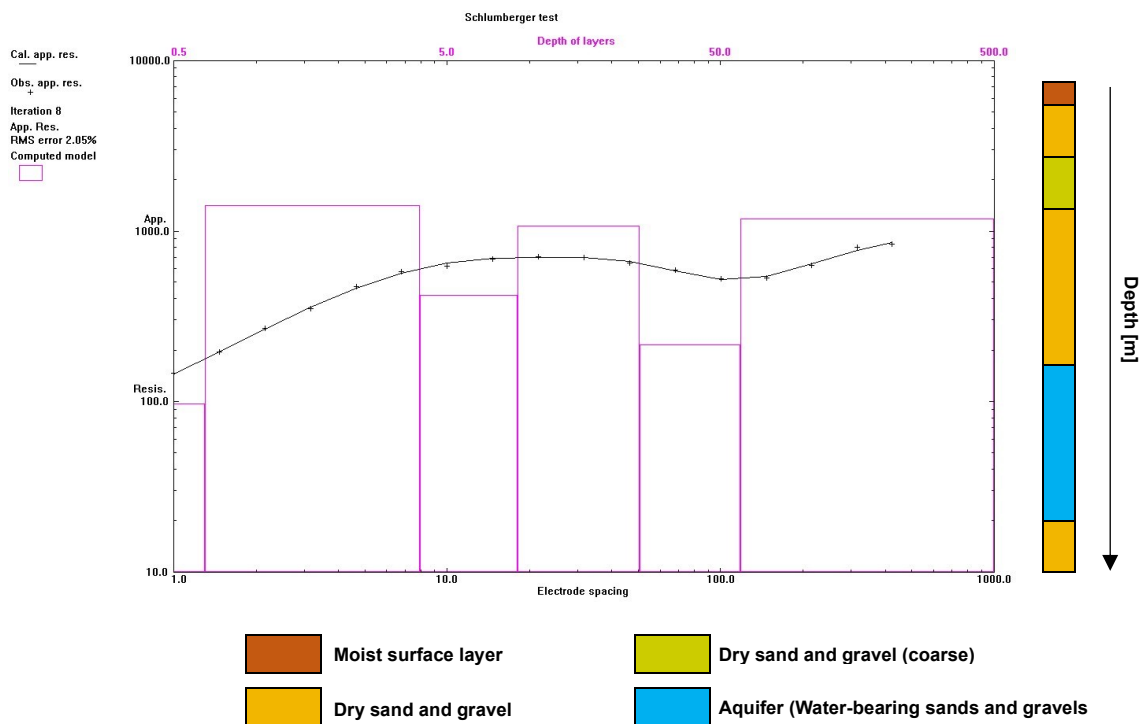


Figure 48: Inversion result of hs01ves. A 6-layer case seems like a good fit, as the calculated apparent resistivities (black continuous line) and the observed apparent resistivities align extremely well. The column profile provides additional visualization of the layered structure.
Abbreviations: Calc.app.res. = Calculated apparent resistivity; Obs.app.res. = Observed apparent resistivity.

horizon, with a thickness of approx. 4.5 m and a resistivity of up to 1200 Ωm , the changing geological structure of the basin fill can be recognized for the first time. This is a shallow insulating formation whose resistivity values can be determined as dry gravel or a dry sandbank (unconsolidated sediments) according to Schmid et al. (1980). Beneath this horizon is another 5 m thick layer with a resistivity of 500 Ωm . Again, the changing character of the basin fill is evident even if the layers are very thin. Presumably, these are still dry sandy or gravelly rocks of different

grain sizes. An insulating layer, 15 m thick, with resistivities of up to 1000 Ωm , probably dry quaternary sediments, overlies the groundwater-bearing body. The latter appears at a depth of approx. 25 m and has significantly lower resistivities (400 Ωm) compared to the layers deposited above. Schmid et al. (1980), as well as Niesner (1971) attribute resistivities in the range of 400-500 Ωm to the water-bearing gravels. The center of the conductive layer is therefore to be expected at an approximate depth of 35 m to 40 m. Underneath, the resistivity increases again and reaches the 1000 Ωm mark. However, it is questionable whether this is the pre-Quaternary basin subsurface, as higher resistivity values would be expected at this point.

10.6. Hs02ves

In the case of the hs02ves profile, as previously mentioned, problems with the straight-line profile continuation in the SW direction, which is essential for a depth sounding, arose. Consequently, the result (Figure 49a) towards the end of the profile (measurement points 15 and 16 marked in red) is not reliable. The fit between measured data and calculated values is too inconsistent to give a plausible estimation of the deeper part of the valley. The inversion of this data set produces a very thick layer with low resistivity, comparable to that of groundwater in the Calcareous Alps, at a depth where the bedrock would be expected due to the known geology. In response to these findings, the last two sounding readings were removed from the file in order to continue the inversion with only the reliable values. Unfortunately, this shortening of the profile also resulted in a reduction of the penetration depth, which made the overall objective of the bedrock detection even more uncertain. The inversion result of the adapted data can be seen in Figure 49b. In contrast to the outcome of profile hs01ves, the RMS error is significantly larger, around 19%, which is evident from the fit comparison between the calculated and observed measurement values. Nevertheless, the interpretation of this sounding profile reflects a relatively simple two-layer case with a 50 m thick layer of constant resistivity (~900-1000 Ωm), presumably composed of unconsolidated sediments such as dry sands and gravels, and an underlying massive layer of high resistivity (>10,000 Ωm), indicative for the bedrock.

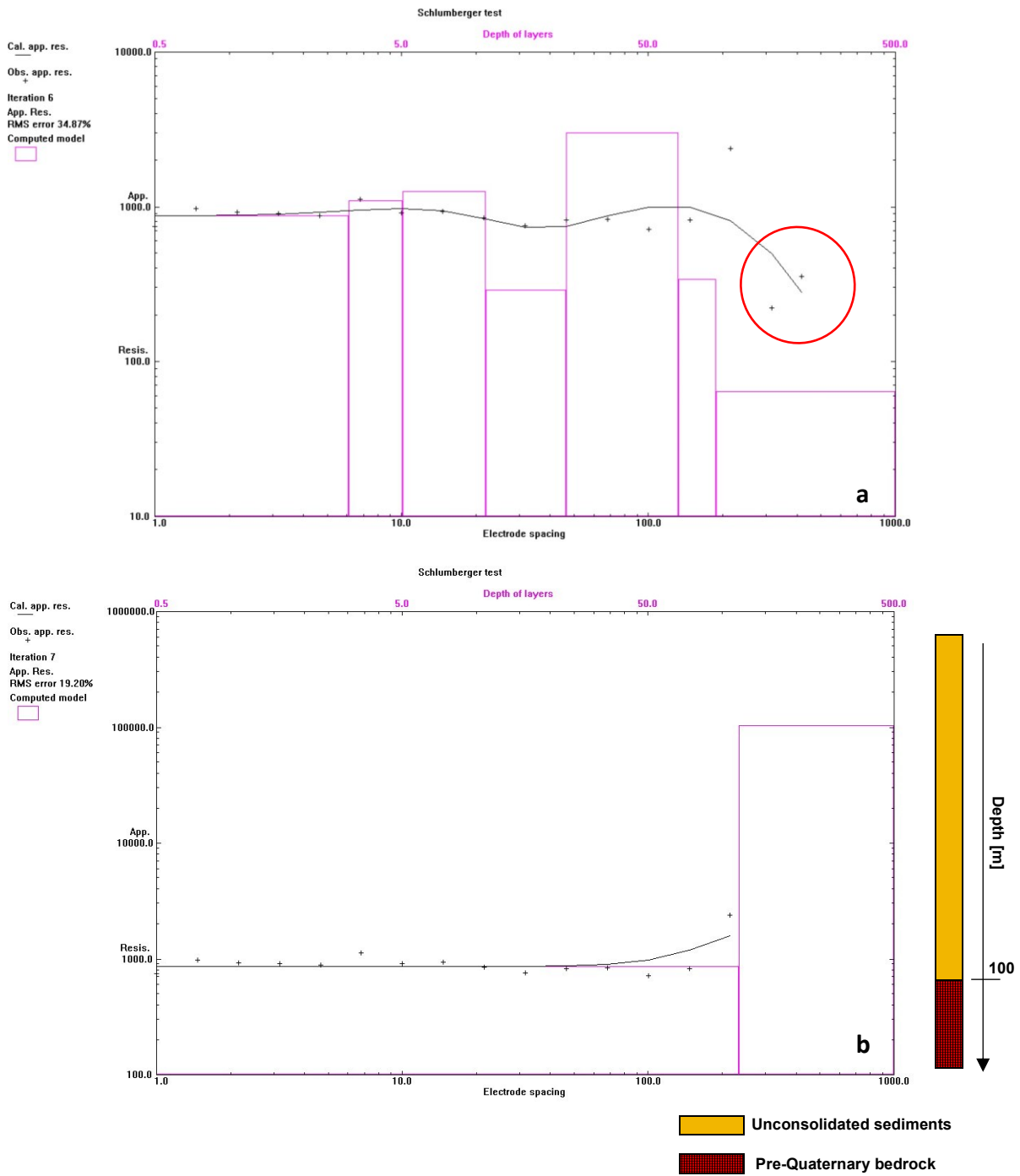


Figure 49: (a) Inversion result of hs02ves with all 17 measurement points (including the measurement points after the kink marked in red). (b) Inversion result after the two clearly misleading measurement points were removed. The two-layer case with the respective lithologies is presented as a column profile to facilitate visualization.
Abbreviations: Calc.app.res. = Calculated apparent resistivity; Obs.app.res. = Observed apparent resistivity.

11. Discussion

The following chapter summarizes the available ERT and VES measurement results of this thesis and compares them with the data acquired by refraction seismic (Niesner, 1971) and the drillings.

11.1. Hs02 and groundwater-related borehole information

Detailed information on water levels from the 1980 studies at BI1, the borehole closest to the two ERT profiles, is not available. The only information provided is that a water level of 70 m (BI1) was measured in 1980 and the borehole would dry out completely in autumn and winter months. The situation is different at BI2 (Figure 50a), where groundwater levels have been detected at a depth of 18-20 m in the comparative period of May and June in the past. Figure 50b visualizes the groundwater level fluctuations from 2008 to 2019. These measurement results correlate well with findings from the seismic survey and the ERT, both of which locate the beginning of the water-

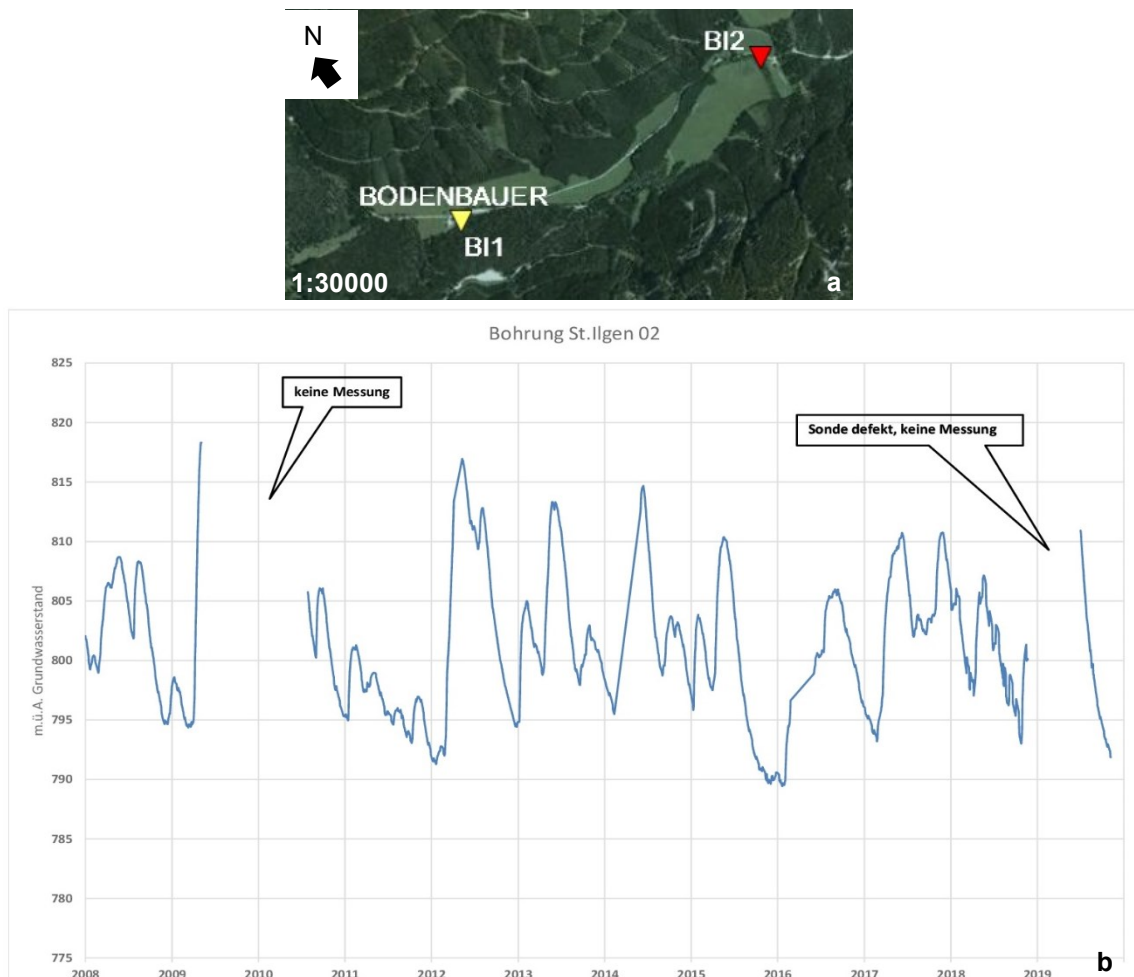


Figure 50: (a) Orthophoto illustrating the distance between the two reference points Bodenbauer restaurant (yellow triangle) and BI2 (red triangle). (b) The diagram shows the groundwater level fluctuations from 2008-2019. Either no measurements were taken, or the equipment was defective for sections where no measured values are available. Modified after <https://www.zwhs.at/wasserhaushalt/hydrographie/st-ilgen/> 16.04.2024.

bearing gravels at a depth of 15-20 m. The correlation of the groundwater table heights between Bodenbauer (Profile hs01) and Moarhof (BI2) indicates that the aquifer is either a continuous one (Figure 39), or that the apparent topographic barrier (Figure 42) between the two aquifers has no significant impact on the water table levels.

11.2. Hs01 (2022) and refraction seismic data (1971)

The profile hs01 was superimposed on the graphical representation of the seismic measurement results in order to facilitate comparison of the similarities and possible inconsistencies (Figure 51). For this juxtaposition, the measurement with the Multi Gradient array was used on the ERT side, as the model obtained after the inversion corresponds very well with the seismic data in many areas. The resemblance is excellent, as the two profiles could be relatively well correlated using prominent points such as the Bodenbauer restaurant from the seismic overview map, as well as the elevations of the relevant shot points noted on this map (Figure 11).

The model (Figure 51) calculated using the ERT shows three different layers (excluding the thin, highly conductive uppermost horizon), which can also be easily differentiated in the seismic analysis based on the different velocities. The approximately 15 m thick layer with resistivities of up to 1200 Ωm determined in the ERT corresponds to the seismic horizon with velocities of up to 500 m/s. These resistivities, once again, indicate dry unconsolidated material, presumably sandy and clay-rich gravels, being in relatively good agreement with the interpretation of the velocities according to Niesner (1971). The second prominent horizon, interpreted in the ERT as water-bearing gravels and thus the aquifer, also matches the seismic results well, as the velocities between 1500-2000 m/s were depicted as water-bearing unconsolidated material. The deepest recognizable horizon in the ERT with resistivities ranging towards 900-1000 Ωm , would indicate dry Quaternary deposits. According to the seismic interpretation, however, Werfen Shale could occur at this depth for the first time. If shot point 11 is followed to depth until the fault emerges in the seismic survey, Figure 51 provides a reasonable agreement between the compared data sets. The fault, according to Niesner (1971), could have been tracked quite far toward the surface. A fault (marked with a red arrow in Figure 51) can be detected in the inversion results of the ERT as a distinctive feature in the subsurface as well, possibly causing the separation into two water-bearing horizons.

The results of the depth sounding hs01ves also confirm the findings of the two interpretations already mentioned, since the water-bearing layers were detected at a depth of around 20-25 m, and the bedrock, the Werfen Shale, has not yet been reached.

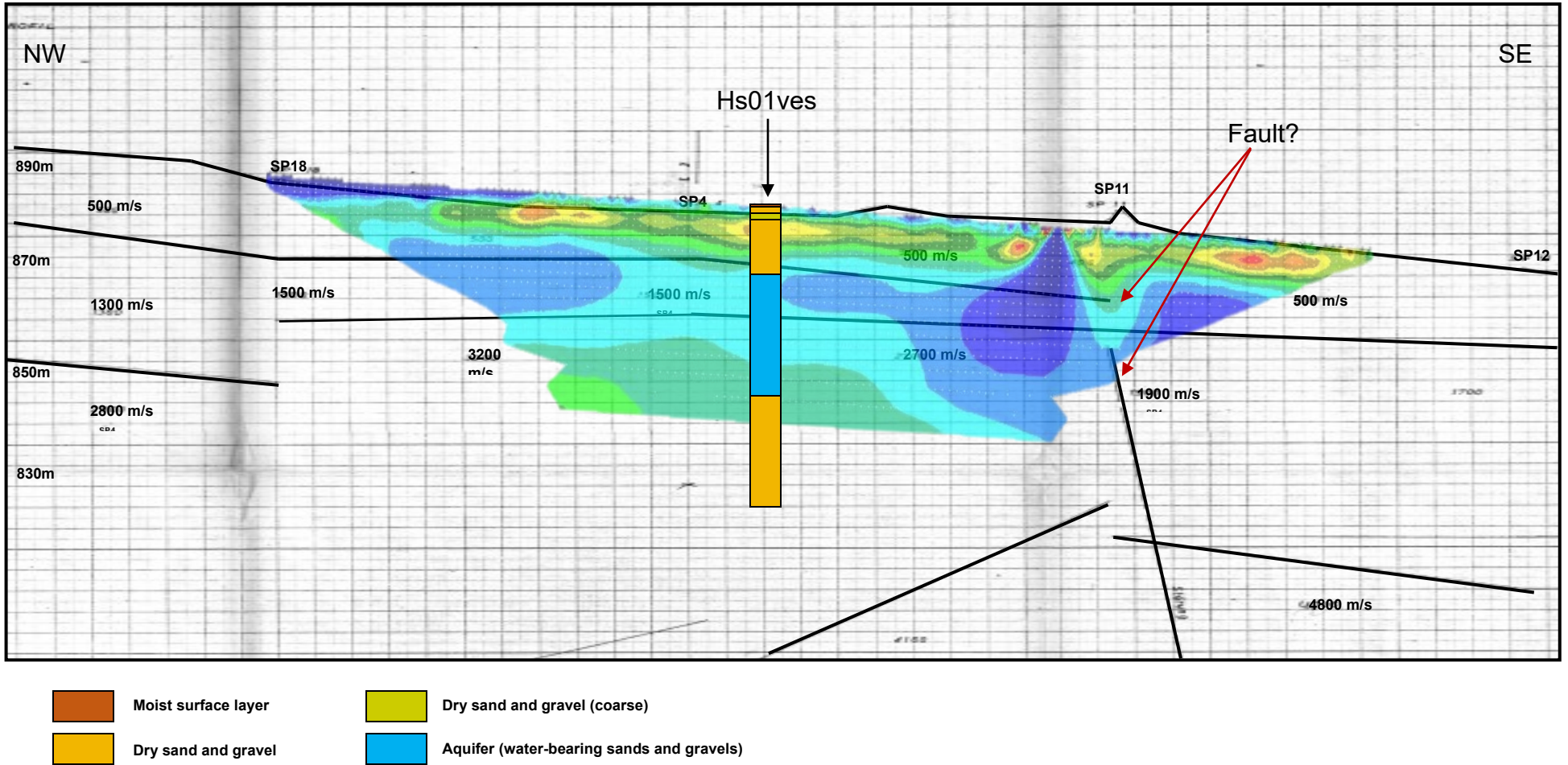


Figure 51: Overlay of the ERT and VES results, with a part of the seismic interpretation. Interesting features, such as the fault and the layered structure are relatively comparable (modified after Niesner, 1971). The black arrow indicates the position of the VES (hs01ves). The red arrows depict the possible position of the fault in the seismic model and in the ERT result. Velocities are in m/s.

11.3. Hs02 (2022) and refraction seismic data (1971)

A comparison (Figure 52) between hs02, hs02ves and the seismic results from 1971 reveals a high degree of positional agreement between the three outcomes. Similar to hs01, the approach for the superposition procedure was almost identical, except that the intersection points of the two seismic profiles and the intersection points of the two ERT profiles, as well as the elevations of the shot points for comparison with the elevations of the electrode positions were taken into account. The only thing necessary was to rotate the seismic profile by 180° along the ordinate to have both profiles start in the SW.

The comparison of the interpretations in Figure 52 is coherent, as the seismic horizons correspond well with the ERT results. A higher situated horizon with velocities around 500 m/s matches the high-resistivity area extremely well. According to the ERT, this layer is underlain by another dry horizon with similar resistivities. In the seismic section, however, the velocities increase up to 1800 m/s. This could now indicate either a water-bearing layer package on the one hand, which would not be apparent in the ERT and in the depth sounding, or on the other hand more solidified sandy-loamy gravels and moraines. Consequently, the interpretation of this horizon, which cannot be precisely differentiated using only the seismic survey, would be based on the comparison of all three measurements. Consequently, the more plausible result would be the dry consolidated sediments.

The outcome of the depth sounding hs02ves, which is not close to the center of the ERT profile compared to the situation of hs01ves, reflects a relatively interesting result, which does not contradict the ERT and seismic models. The position of the central electrode of the VES is marked with a black arrow in Figure 52. The interpreted two-layer case is still feasible given that the depth sounding suggests a high-resistivity horizon at a depth of 100 m. Figure 52 graphically indicates this two-layer case using a column profile at the position of the VES. Due to the given morphology, a sudden appearance of the bedrock is possible.

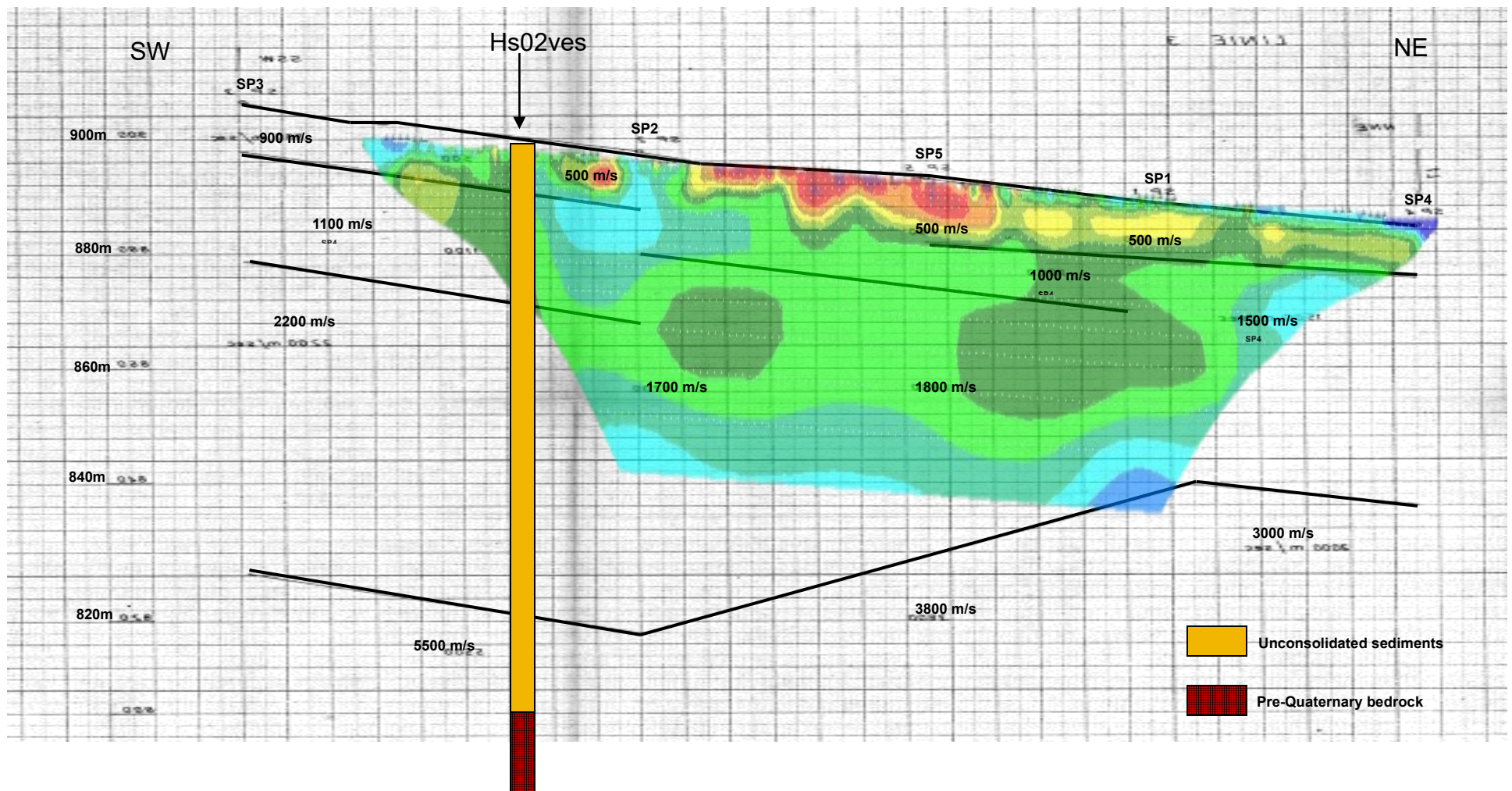


Figure 52: Overlay of the ERT results (hs02) and a part of the seismic interpretation (modified after Niesner, 1971). The black arrow indicates the position of the VES (hs02ves). The velocities are in m/s.

12. Summary and Conclusions

Finally, the measurements provided largely satisfactory results, with some of the questions posed in the thesis being answered, but some of them not fully resolved, meaning the need for further tests remains. The aim of this master's thesis was to gather new data using modern measurement methods in order to compare them with the historical data from the measurement campaigns of the 1970s and 1980s. This data was intended to provide evidence of the presence or absence of water-bearing layers and the height of the groundwater table. Additional information on the overall structure of the basin filling was obtained. The second research question was the detection of the upper edge of the basin floor, which could only be answered in parts.

The layered structure of the basin (hs01) was confirmed both by the results of the ERT and the VES and is consistent with the borehole data (Fabiani, 1980) and the seismic results (Niesner, 1971). For hs02, the multi-layered structure derived from the seismic survey (Niesner, 1971) is not as clearly identifiable, since the results of the VES indicate a two-layer case, which is again also supported by the ERT.

The presence of an aquifer in the Bodenbauer area (hs01) was detected in both the historical seismic data and the borehole data. The elevation of the groundwater-bearing layers, which were initially expected at a depth of 5-7 m in BI 1 in the 1970s and subsequently determined at a depth of 60 m on the basis of the borehole data, does not match the ERT results of this work. However, the seismic findings (Niesner, 1971), which identified an aquifer at a depth of 20 m, can be verified by the ERT and VES data. The aquifer is located below a non-conductive surface layer at a depth of 15 – 20 m according to this thesis.

The possibility for the existence of an aquifer was uncertain for profile hs02, as the results from the seismic survey (Niesner, 1971) could be interpreted both as water-bearing layers or as dry, consolidated sediments. The additional measured values from the ERT data indicate that an aquifer is not present in this area, as the measured resistivities are clearly too high. The shortened VES profile hs02ves confirms these statements, as consistently high resistivities were recorded down to a depth of 100 m.

The ERT results of hs01 and hs02 correlate extremely well, as an aquifer identified in hs01 was found at a comparable depth in the outcrops of hs02 at the intersection of the two profiles.

The depth of the Werfen Shales in profile hs01, forming the impermeable bedrock, could not be precisely determined from the borehole data. Based on the calculated model from the ERT, the bedrock has not yet been reached using this measurement technique. The fault, detected by the

seismic, could possibly be confirmed by the ERT data, which would potentially result in a separation into two aquifer compartments. However, this separation cannot be exclusively verified, as the combined results of Pole-Dipole and Dipole-Dipole arrays do not reveal this theoretical separation.

The detection of the pre-Quaternary basin subsurface at profile hs02 also proves to be very difficult due to the shortened VES measurement lay-out. However, due to the steeply dipping topography on the flanks, the appearance of the bedrock at a depth of 100 m would be possible.

13. Outlook

Overall, the results and interpretations presented in the previous chapters, both new and historical, provide a good overview of the valley filling in the Buchberg-St. Ilgen area at the southern flank of the Hochschwab Massif. Nevertheless, there are still some considerations regarding further measurements and subsequent observations that would be interesting and relevant in this hydrologically important study area.

A first possible step would be to slightly shift the midpoint of the depth sounding for both profiles allowing the full deployment potential to be utilized, even if this could be problematic due to the partially steep flanks. However, in a possible repetition of the survey of hs02ves, the kink in the profile before the last two measurements could be avoided in order to obtain an easily interpretable overall result.

Secondly, considering the availability of geoelectrical measurement results from the 1970s in the Karlschütt spring area and the current results from the Bodenbauer area, it would be of great interest to carry out an ERT around the Moarhof well house (headquarter ZWHS), as these could be correlated relatively well with current water levels. There is also publicly accessible water level and groundwater monitoring data from the 1980s for this area, which would also support comparability over longer periods. Sufficient space for relevant and adequate profile lay-outs would be available as well.

A third interesting point would be the monitoring of the presumed groundwater level or the movement of the water in the aquifer itself. For this purpose, 4D resistivity methods could be used to measure changes in resistivity in space and time. Measurements of the same profiles are repeated at different times, allowing, for example, the effects of heavy rainfall events (thunderstorms) or the annual snowmelt to be observed and documented.

14. References

- Bauer, C., 2010. Der Karst der Steiermark - der Karstformenschatz und seine Interaktion mit dem Menschen. Unpubl. Dissertation, University of Graz, 186 p.
- Bauer, C. and Lieb, G. K., 2011. Wasserwirtschaft, Eiszeit und Naturgefahren zu beiden Seiten des Hochschwab. Unterwegs mit GeoGraz - Ein Exkursionsführer in Fortsetzungen 48, p. 44-52.
- Bauer, H., Schröckenfuchs, T. C. and Decker, K., 2016. Hydrogeological properties of fault zones in a karstified carbonate aquifer (Northern Calcareous Alps, Austria). *Hydrogeology Journal* 24, p. 1147-1170.
- Bryda, G., van Husen, D., Kreuss, O., Koukal, V., Moser, M., Pavlik, W., Schönlaub, H. P. and Wagreich, M., 2013. Erläuterungen zu Blatt 101 Eisenerz. Geologische Bundesanstalt, Wien, 230 p.
- Cheng, K., Simske, S. J., Isaacson, D., Newell J. C., Gisser, D. G., 1990., Errors due to measuring voltage on current-carrying electrodes in electric current computed tomography. *IEEE Transactions on Medical Imaging* 37, p. 60-65.
- Constable, S. C., Parker, R. L. and Constable, C. G., 1987. Occam's inversion: A practical algorithm for generating smooth models from electromagnetic sounding data. *Geophysics* 52, p. 289-300.
- Dahlin, T., Loke, M. H., 1997. Quasi-3D resistivity imaging-mapping of three-dimensional structures using two-dimensional DC resistivity techniques. *Proceedings of the 3rd Meeting of the Environmental and Engineering Geophysical Society*, p. 143-146.
- Dahlin, T. and Zhou, B., 2004. A Numerical Comparison of 2D Resistivity Imaging with Ten Electrode Arrays. *Geophysical Prospecting* 52, p. 379-398.
- Dahlin, T. and Zhou, B., 2006. Multiple-gradient array measurements for multichannel 2D resistivity imaging. *Near Surface Geophysics* 4, p. 113-123.
- Daily, W., Ramirez, A., Binley, A. and LaBrecque, D., 2005. Electrical Resistance Tomography Theory and Practice. In Butler, D. K. (Ed.) *Near-surface geophysics*. Tulsa: Society of Exploration Geophysicists, p. 525-550.
- Decker, K. and Reiter, F., 2001. Strukturgeologische Methoden zur Charakterisierung von Karstgrundwasserwegen im Hochschwabmassiv. - In: Mandl, G. W. (Ed.): *Arbeitstagung der Geologischen Bundesanstalt in Neuberg an der Mürz, 03.-07. Sept. 2001*, Geologische Bundesanstalt, Wien, p. 206-212.
- Dentith, M., Mudge, S., 2014. *Geophysics for the mineral exploration geoscientist*. Cambridge University Press. 516 p.
- Dey, A. and Morrison, H. F., 1979a. Resistivity modelling for arbitrary shaped two-dimensional structures. *Geophysical Prospecting* 27, p. 106-136.
- Ellis, R. G. and Oldenburg, D. W., 1994a. Applied geophysical inversion: *Geophysical Journal International* 116, p. 5-11.
- European Union Agency for the Space Program (EUSPA), 2024. What is GNSS?, <https://www.euspa.europa.eu/european-space/eu-space-programme/what-gnss>, 19.01.2024.

Fabiani, E., 1980. Grund- und Karstwasseruntersuchungen im Hochschwabgebiet - Teil II: Die Untersuchungen: Geschichte - Durchführung - Methodik. Berichte der wasserwirtschaftlichen Rahmenplanung Band 45, Steiermärkische Landesdirektion, Graz, 63 p.

Fabiani, E., Weißensteiner, V. and Wakonigg, H., 1980. Grund- und Karstwasseruntersuchungen im Hochschwabgebiet - Teil I: Naturräumliche Grundlagen: Geologie - Morphologie - Klimatologie. Berichte der wasserwirtschaftlichen Rahmenplanung Band 44, Steiermärkische Landesdirektion, Graz, 147 p.

Flenniken, J. M., Stuglik, S. and Iannone, B. V., 2020. Quantum GIS (QGIS): An introduction to a free alternative to more costly GIS platforms. EDIS 2020, p. 1-7.

Friedrich, C., 2014. Comparison of ArcGIS and QGIS for applications in sustainable spatial planning. Dissertation, University of Vienna.

GF Instruments, 2023. Geophysical Instruments - Resistivity & IP - ARES II. GF Instruments s.r.o. 28.12.2023.

Griffiths, D. H. and Barker R. D., 1993. Two-dimensional resistivity imaging and modelling in areas of complex geology. *Journal of Applied Geophysics*, 29, p. 211-226.

International Federation of Air Traffic Controllers' Associations (IFACTA), 1999. A Beginner's Guide to GNSS in Europe, p. 1-14.

Kemna, A., 2000. Tomographic inversion of complex resistivity—Theory and application. Ph.D. thesis, Bochum University.

Kristan-Tollmann, E. and Tollmann, A., 1962. Die Mürzalpendecke - eine neue hochalpine Großeinheit der östlichen Kalkalpen. *Sitzungsberichte der Österreichischen Akademie der Wissenschaften. Matheamtisch-Naturwissenschaftliche Klasse. Abteilung I*, 171, p. 7-39.

Kuschnig, G., 2009. Forschungsansätze zur Bewältigung kommender Herausforderungen bei der Wasserversorgung von Großstädten (Research approaches and coping strategies for the water supply of major cities). Workshop of the Geological Survey of Austria, Conference Proceedings 2009, p. 199-203.

LaBrecque, D., Miletto, M., Daily, W., Ramirez, A. and Owen, E., 1996. The effects of 'Occam' inversion of resistivity tomography data. *Geophysics* 61, p. 538-548.

Li, Y. G. and Oldenburg, D. W., 1992. Approximative inverse mapping in DC resistivity problems. *Geophysical Journal International* 109, p. 343-362.

Lines, L. R. and Treitel, S., 1984. Tutorial: A review of least-squares inversion and its application to geophysical problems. *Geophysical Prospecting* 32, p. 159-186.

Linzer, H. G., Decker, K., Peresson, H., Dell'Mour, R. and Frisch, W., 2002. Balancing lateral orogenic float of the Eastern Alps. *Tectonophysics* 354, p. 211-237.

Loke, M. H., 2001. Resistivity, IP & SIP - Inversion and forward modeling - Wenner and Schlumberger arrays, p. 1-7.

Loke, M. H., 2021. Tutorial: 2-D and 3-D electrical imaging surveys. Geotomo Software Malaysia. 232 p.

Loke, M. H. and Dahlin, T., 2002. A comparison of the Gauss-Newton and quasi-Newton methods in resistivity imaging inversion. *Journal of Applied Geophysics* 49, p. 149-162.

- Loke, M. H., Acworth, I. and Dahlin, T., 2003. A comparison of smooth and blocky inversion methods in 2-D electrical imaging surveys. *Exploration Geophysics* 34, p. 182-187.
- Maguire, D. J., 1991. An Overview and Definition of GIS. In: Maguire, D. J., Goodchild, M. F. and Rhind, D. W., (Eds.). *Geographical Information Systems: Principles and Applications*. Vol. 1. Hoboken: Wiley, p. 9-20.
- Meidl, C. H., Novak, J. and Wessiak, W., 1980. Untersuchung über die Möglichkeit zur Entnahme von Grundwasser im südlichen Hochschwabgebiet und deren Bewirtschaftung. *Berichte der wasserwirtschaftlichen Rahmenplanung Band 49*, Steiermärkische Landesdirektion, Graz, 94 p.
- Militer, H., Rosler, R., and Losch, W., 1979. Theoretical and experimental investigations for cavity research with geoelectrical resistivity methods. *Geophysical Prospecting* 27, p. 640-652.
- Missoni, S. and Gawlick, H. J., 2011a. Jurassic Mountain building and Mesozoic-Cenozoic geodynamic evolution of the Northern Calcareous Alps as proven in the Berchtesgaden Alps (Germany), *Facies* 57/1, p. 137-186.
- Nachtnebel, H. P., Senoner, T., and Stanzel, P., 2012. Climate change and impacts on water supply. WP4 Water Resour Rep, Institute of Water Management, Hydrology and Hydraulic Engineering (IWHW), University of Natural Resources and Life sciences Vienna. EGU General Assembly 2012.
- Niesner, E., 1971. Bericht über die refraktionsseismischen Messungen des Jahres 1971 im Hochschwabgebiet (Bodenbauer - St. Ilgen), Amt der steiermärkischen Landesdirektion, Graz, p. 1-17.
- Oldenburg, D. W. and Li, Y. G., 1999. Estimating depth of investigation in DC resistivity and IP surveys. *Geophysics* 64, p. 403-416.
- Plan, L. and Decker, K., 2006. Quantitative karst morphology of the Hochschwab plateau, Eastern Alps, Austria. *Zeitung Geomorphologie* 147, p. 29-56.
- Pous, J., Queralt, P. and Chavez, R., 1996. Lateral and topographic effects in geoelectric soundings. *Journal of Applied Geophysics* 35, p. 237-248.
- Revil, A., Karaoulis, M., Johnson, T. and Kemna, A., 2012. Review: Some Low-Frequency Electrical Methods for Subsurface Characterization and Monitoring in Hydrogeology. *Hydrogeological Journal* 20, p. 617-658.
- Robinson, E. S. and Coruh, C., 1988. *Basic Exploration Geophysics*. Wiley, New York, 562 p.
- Sasaki, Y., 1994. 3-D resistivity inversion using the finite-element method. *Geophysics* 59, p. 1839-1848.
- Schmid, C., Zojer, H., Krainer, H., Ertl, H. and Ott, R., 1980. Grund- und Karstwasseruntersuchungen im Hochschwabgebiet Teil III: Geophysik-Isotopenuntersuchungen-Hydrochemie. *Berichte der wasserwirtschaftlichen Rahmenplanung Band 46*, Steiermärkische Landesdirektion, Graz, 134 p.
- Schmid, S. M., Fügenschuh, B., Kissling, E. and Schuster, R., 2004. Tectonic map and overall architecture of the Alpine orogen. - *Eclogae Geologicae Helvetiae* 97, p. 93-117.
- Silvester, P. P. and Ferrari, R. L., 1990. *Finite elements for electrical engineers* (2nd. ed.). Cambridge University Press.

Stadler, H. and Benischke, R., 2009. Die Hydrogeologie des Hochschwabgebietes - Forschungsergebnisse im Überblick. Arbeitstagung der Geologischen Bundesanstalt 2009, p. 122-142.

Stadt Wien, 2023. Der Weg des Wiener Wassers von den Alpen in die Stadt https://www.geschichtewiki.wien.gv.at/Zweite_Hochquellenleitung. 28.12.2023.

Suluguru, A., Surana, S. and Guharay A., 2019. Experimental Investigations on Building Derived Materials in Chemically Aggressive Environment as a Partial Replacement of Soil in Geotechnical Applications. Geotechnical and Geological Engineering 37, p 947-963.

Zentral-Wasserversorgung Hochschwab Süd Ges.m.b.H, 2024. Hydrographie - Thörl/St.Ilgen [ZWHS - Thörl / St. Ilgnertal 16.04.2024](#)

Zhou B. and Dahlin T., 2003. Properties and effects of measurement errors on 2D resistivity imaging. Near Surface Geophysics 1, p. 105- 117.

Zonge, K., Wynn, J., and Urquhart, S., 2005. Resistivity induced polarization and complex resistivity. In Butler, D. K. (Ed.) Near-surface geophysics. Tulsa: Society of Exploration Geophysicists, p. 265-300.

15. Appendix

15.1. Refraction seismic

15.1.1. Line 1

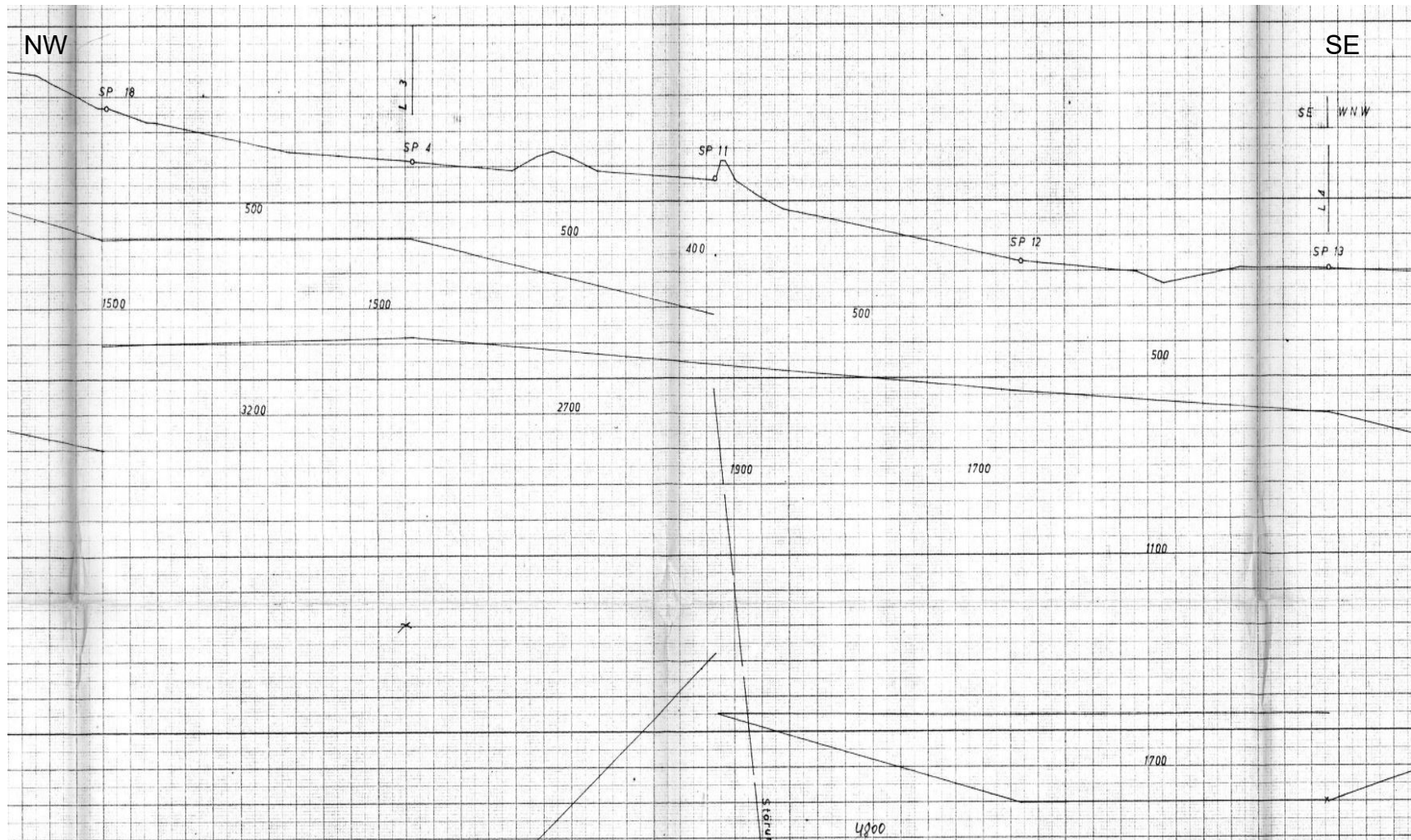


Figure 53: Relevant section from Line 1 of the seismic (modified after Niesner, 1971).

15.1.2. Line 3

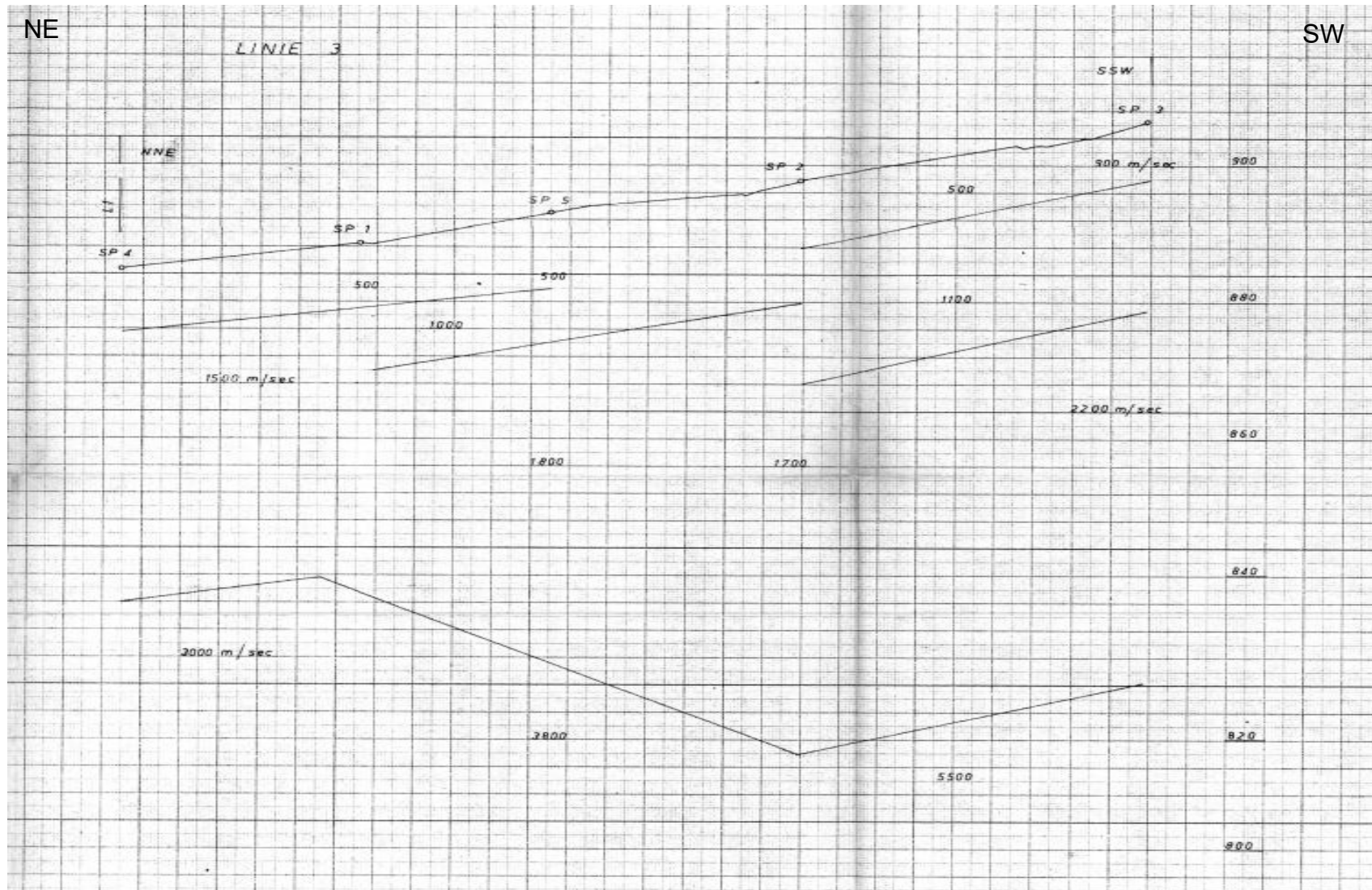


Figure 54: Relevant section from Line 3 of the seismic (modified after Niesner, 1971).

15.2. ERT

15.2.1. Apparent resistivity histograms

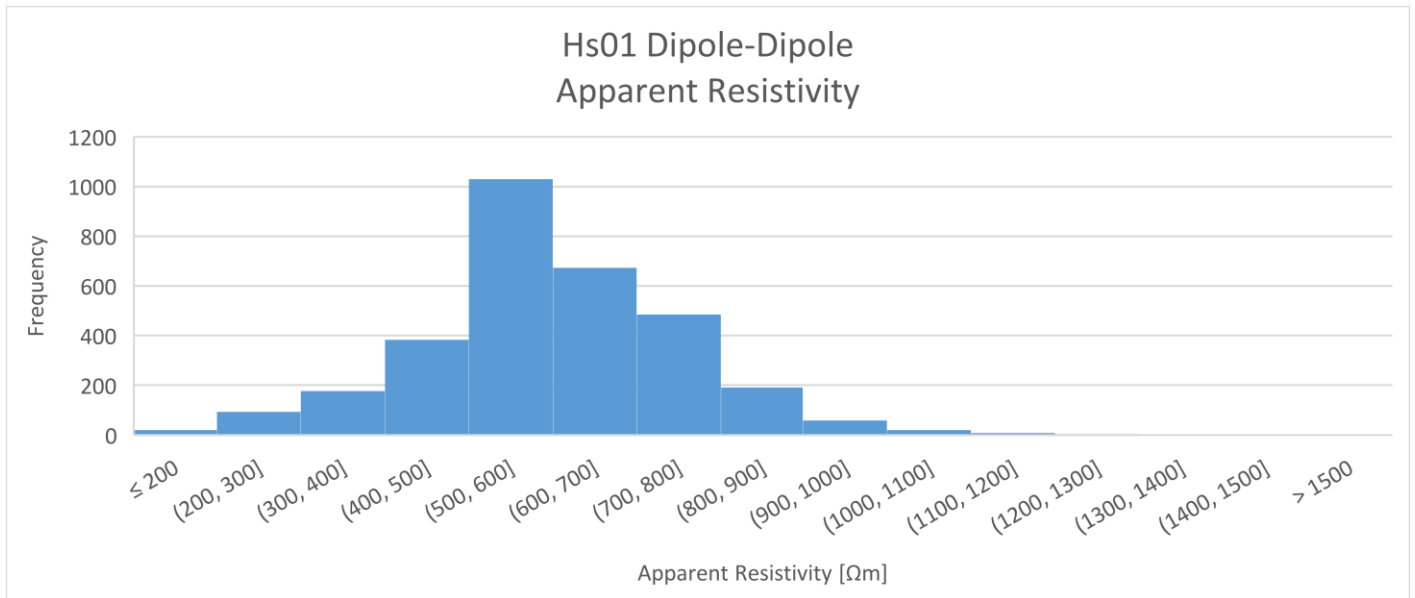


Figure 55: Histogram showing the frequencies of the apparent resistivities of hs01 using the Dipole-Dipole array.

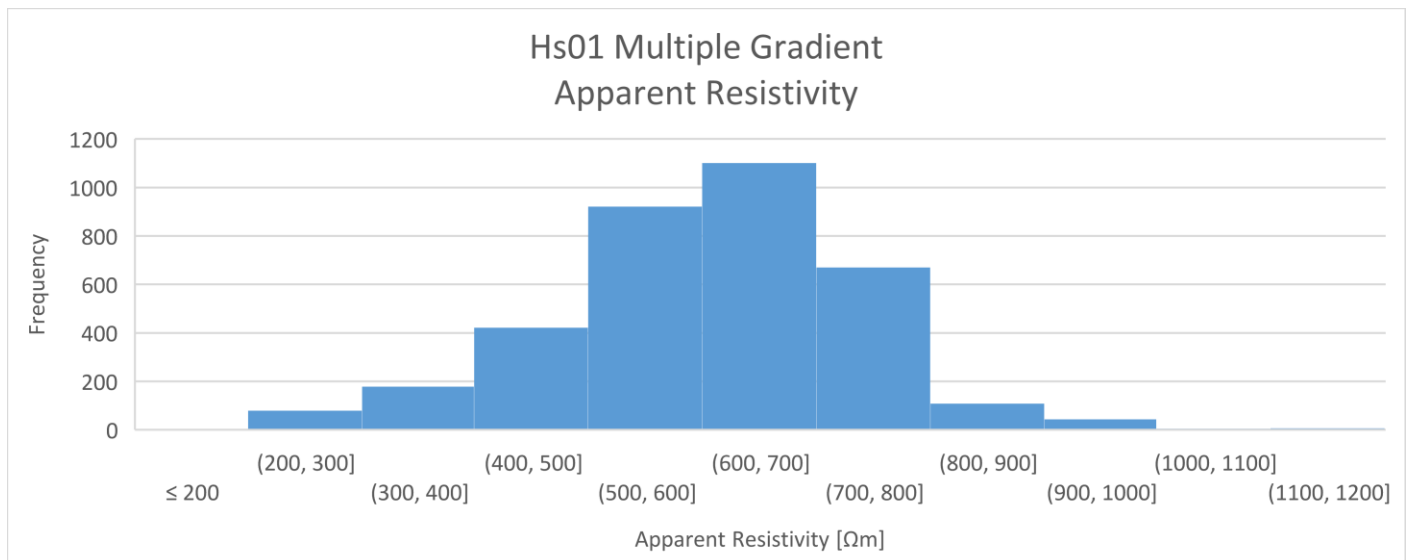


Figure 56: Histogram showing the frequencies of the apparent resistivities of hs01 using the Multiple Gradient array.

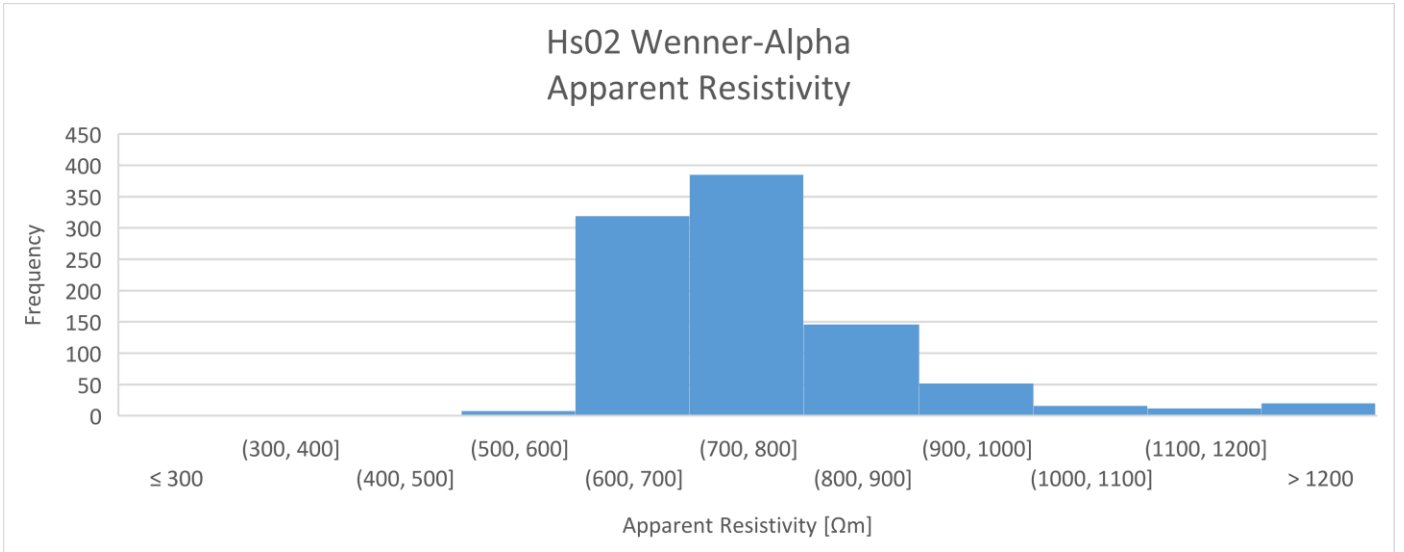


Figure 57: Histogram showing the frequencies of the apparent resistivities of hs02 using the Wenner-Alpha array.

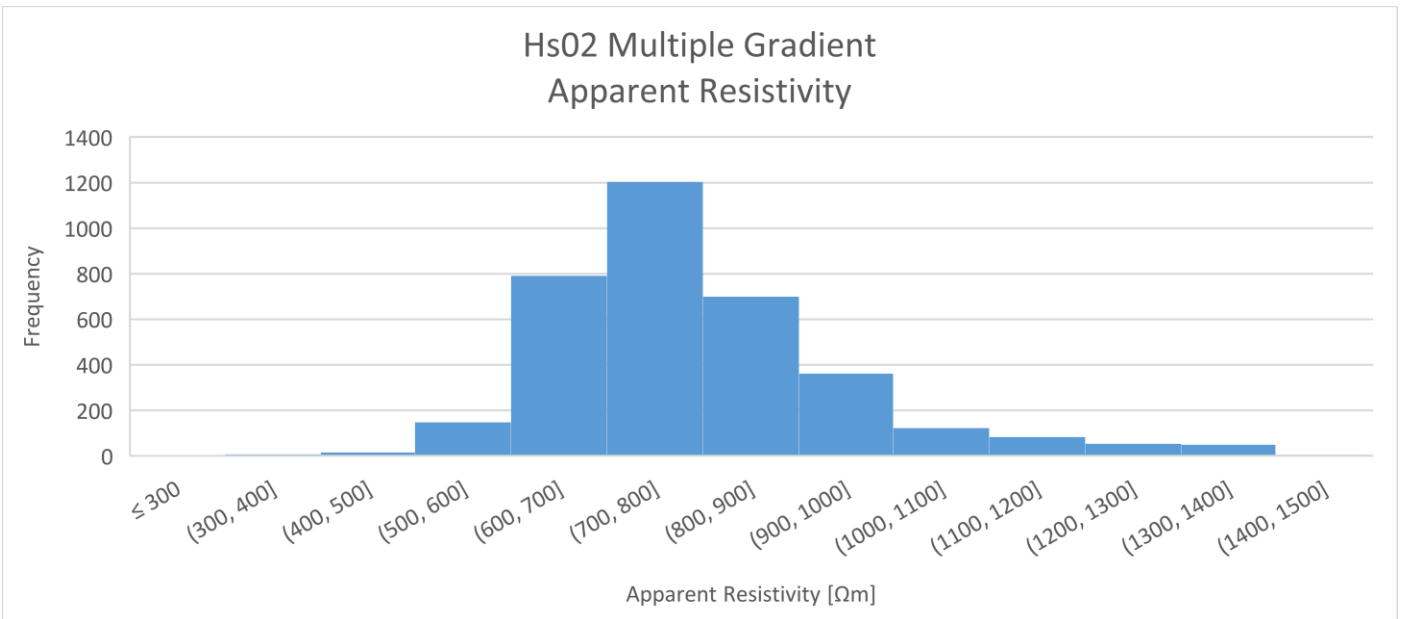


Figure 58: Histogram showing the frequencies of the apparent resistivities of hs02 using the Multiple Gradient array.

15.3. Vertical Electrical Sounding

15.3.1. Hs01ves

Table 6: An overview of the measured values derived from the VES for profile hs01ves.

AB/2 [m]	MN/2 [m]	I (mA)	R [Ohm]	GF	ρ_a (Ωm)
1	0,15	100	14,31	10,2	146,53
1,47	0,15	100	8,755	22,4	196,02
2,16	0,15	100	5,559	48,6	270,28
3,16	0,15	100	3,368	104,3	351,38
3,16	0,5	100	10,72	30,6	327,92
4,64	0,5	100	6,635	66,9	443,55
4,64	0,15	100	2,099	225,2	472,74
6,81	0,15	100	1,198	485,4	581,52
6,81	0,5	100	3,783	144,9	548,19
10	0,5	100	1,986	313,4	622,35
10	1,5	100	6,302	102,4	645,07
14,7	1,5	100	3,182	223,9	712,55
14,7	0,5	100	1,012	678,1	686,22
21,5	0,5	100	0,4906	1451,4	712,07
21,5	1,5	100	1,54	481,7	741,83
31,6	1,5	100	0,6748	1043,3	704,04
31,6	5	100	2,168	305,9	663,08
46,4	5	100	0,9145	668,5	611,36
46,4	1,5	100	0,2887	2252,2	650,21
68,1	1,5	100	0,1214	4854,1	589,29
68,1	5	100	0,3829	1449,1	554,86
100	5	100	0,1679	3133,7	526,15
100	15	100	0,5174	1023,6	529,61
147	15	100	0,2441	2239,3	546,61
147	5	100	0,07874	6780,8	533,92
215	5	100	0,04369	14514,2	634,13
215	15	100	0,1293	4817,1	622,85
316	15	100	0,07695	10433,3	802,84
316	50	100	0,237	3058,5	724,86
423	50	100	0,1497	5542,7	829,74
423	15	100	0,04476	18714,0	837,64

Abbreviations: A,B = Current electrodes; M,N = Potential electrodes; I = Current; R = Resistance; GF = Geometrical factor; ρ_a = Apparent resistivity.

15.3.2. Hs02ves

Table 7: An overview of the measured values derived from the VES for profile hs02ves.

AB/2 [m]	MN/2 [m]	I (mA)	R [Ohm]	GF	ρ_a (Ωm)
1	0,15	50	72,87	10,2	746,19
1,47	0,15	50	43,42	22,4	972,17
2,16	0,15	50	19,12	48,6	929,61
3,16	0,15	100	8,714	104,3	909,13
3,16	0,5	50	25,06	30,6	766,59
4,64	0,5	20	11,19	66,9	748,05
4,64	0,15	20	3,915	225,2	881,74
6,81	0,15	20	2,316	485,4	1124,21
6,81	0,5	20	5,756	144,9	834,10
10	0,5	20	2,92	313,4	915,04
10	1,5	20	7,813	102,4	799,74
14,7	1,5	50	3,686	223,9	825,41
14,7	0,5	50	1,375	678,1	932,36
21,5	0,5	20	0,5833	1451,4	846,61
21,5	1,5	20	1,609	481,7	775,07
31,6	1,5	50	0,7221	1043,3	753,39
31,6	5	50	2,308	305,9	705,90
46,4	5	20	1,081	668,5	722,67
46,4	1,5	20	0,3648	2252,2	821,60
68,1	1,5	50	0,1717	4854,1	833,45
68,1	5	50	0,5126	1449,1	742,81
100	5	50	0,2279	3133,7	714,17
100	15	50	0,6768	1023,6	692,77
147	15	20	0,2802	2239,3	627,45
147	5	20	0,122	6780,8	827,26
215	5	10	0,1636	14514,2	2374,52
215	15	10	0,2481	4817,1	1195,12
316	15	50	0,02141	10433,3	223,38
316	50	50	0,171	3058,5	523,00
418	50	20	0,07416	5410,6	401,25
418	15	20	0,01937	18273,0	353,95

Abbreviations: A,B = Current electrodes; M,N = Potential electrodes; I = Current; R = Resistance; GF = Geometrical factor; ρ_a = Apparent resistivity.

15.4. Orthophotography

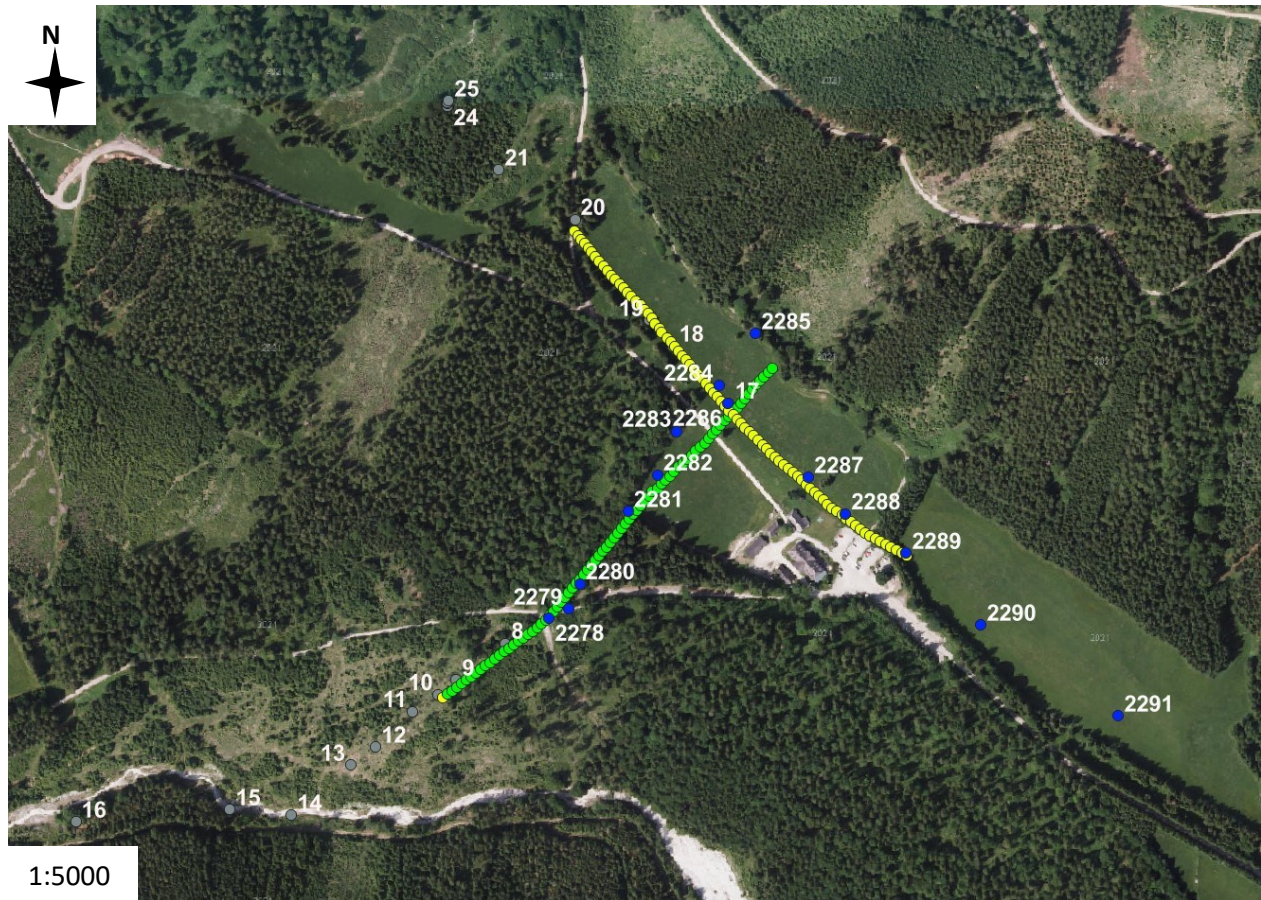


Figure 59: Position of the ERT profiles (hs01 in yellow and hs02 in green) and the VES profiles (hs01ves in gre 17-25, blue 2286-2291 and hs02ves in grey 8-16, blue 2278-2285).

15.5. ERT Results

15.5.1. Dipole-Dipole array for hs01

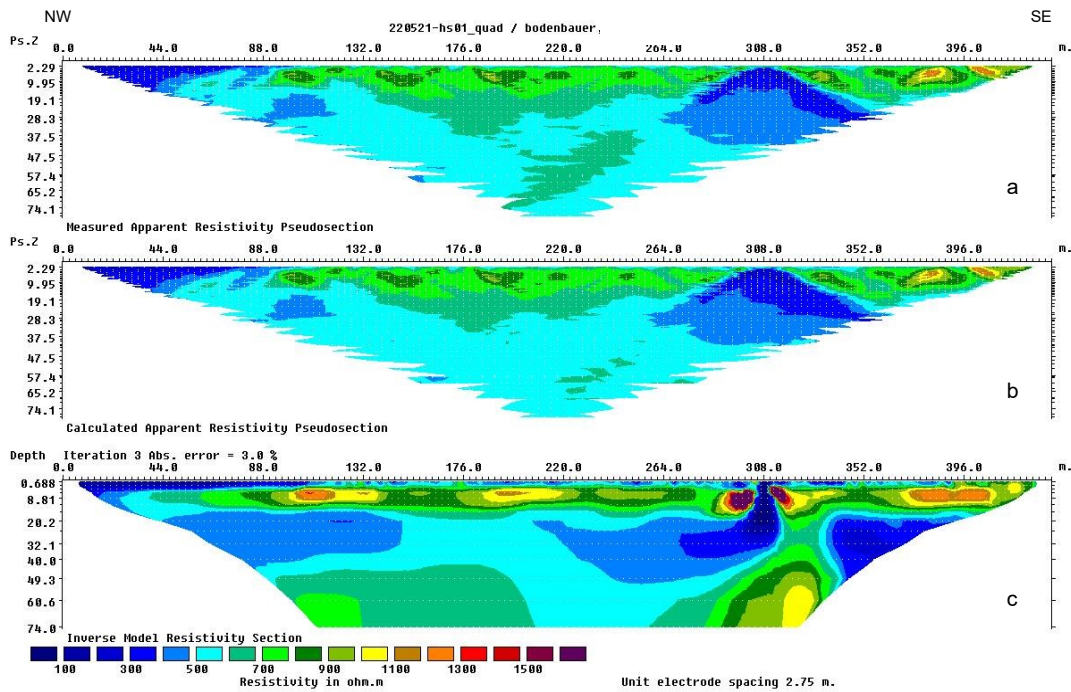


Figure 60: The measured apparent resistivities (a) compared to the calculated apparent resistivities for the Multiple Gradient array of hs01. (c) The inversion result represents a geological model derived from the data sets.

15.5.2. Dipole-Dipole array for hs01 with the implementation of a fixed resistivity region

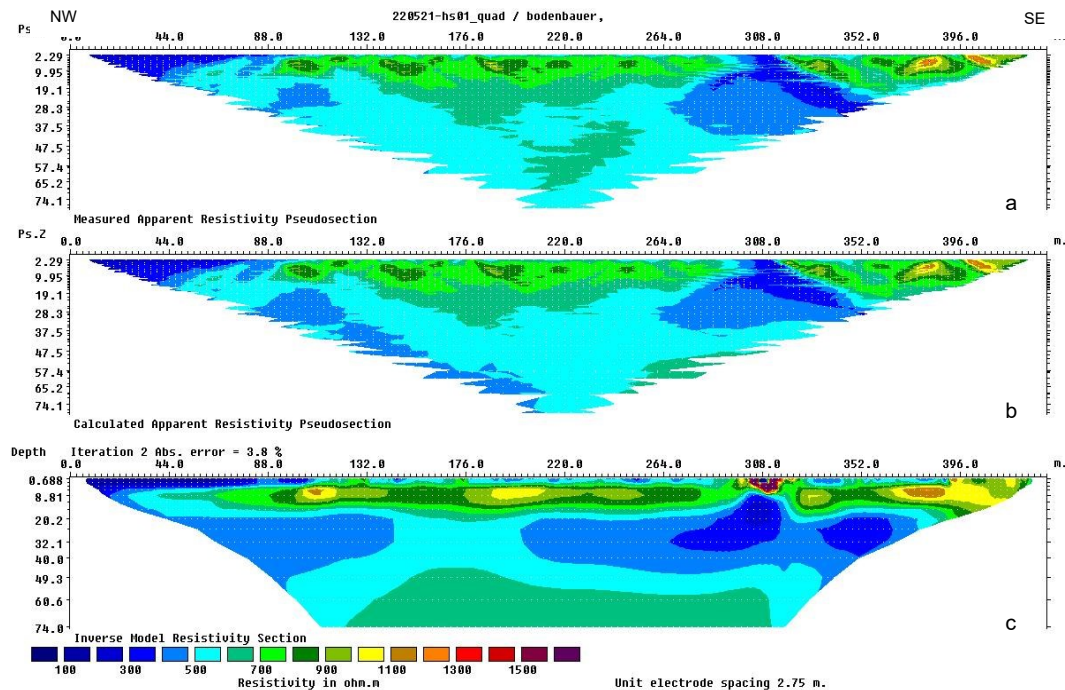


Figure 61: The measured apparent resistivities (a) compared to the calculated apparent resistivities for the Dipole-Dipole array of hs01 with a fixed resistivity at a predefined location. (c) The inversion result represents a geological model derived from the data sets.

15.5.3. Multiple Gradient array for hs01

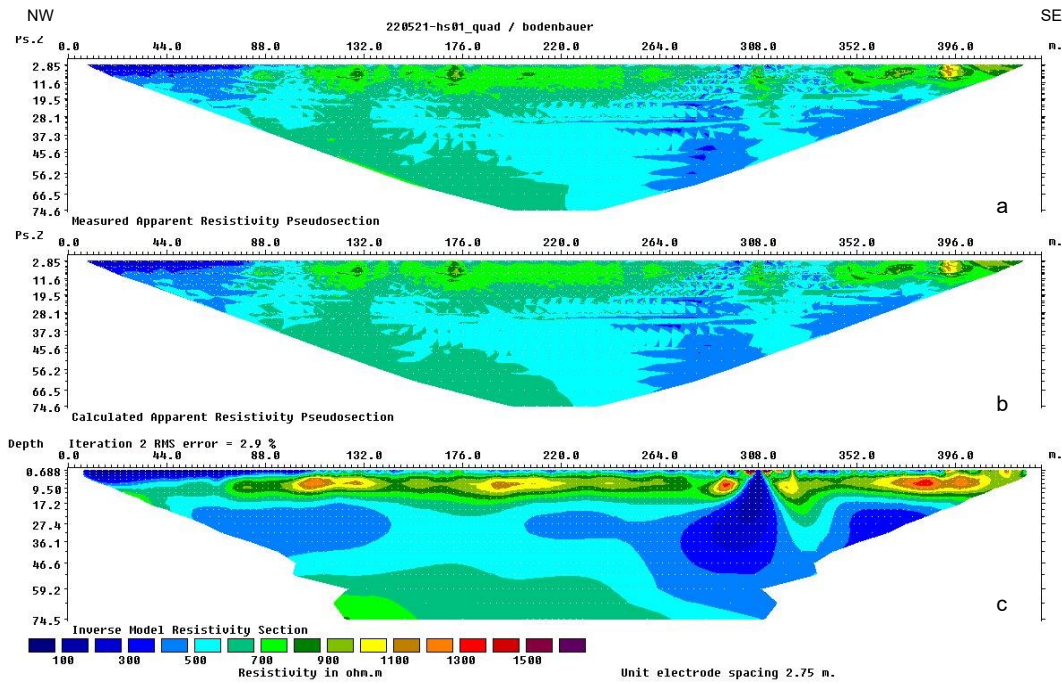


Figure 62: The measured apparent resistivities (a) compared to the calculated apparent resistivities for the Dipole-Dipole array of hs01. (c) The inversion result represents a geological model derived from the data sets.

15.5.4. Dipole-Dipole array for hs02

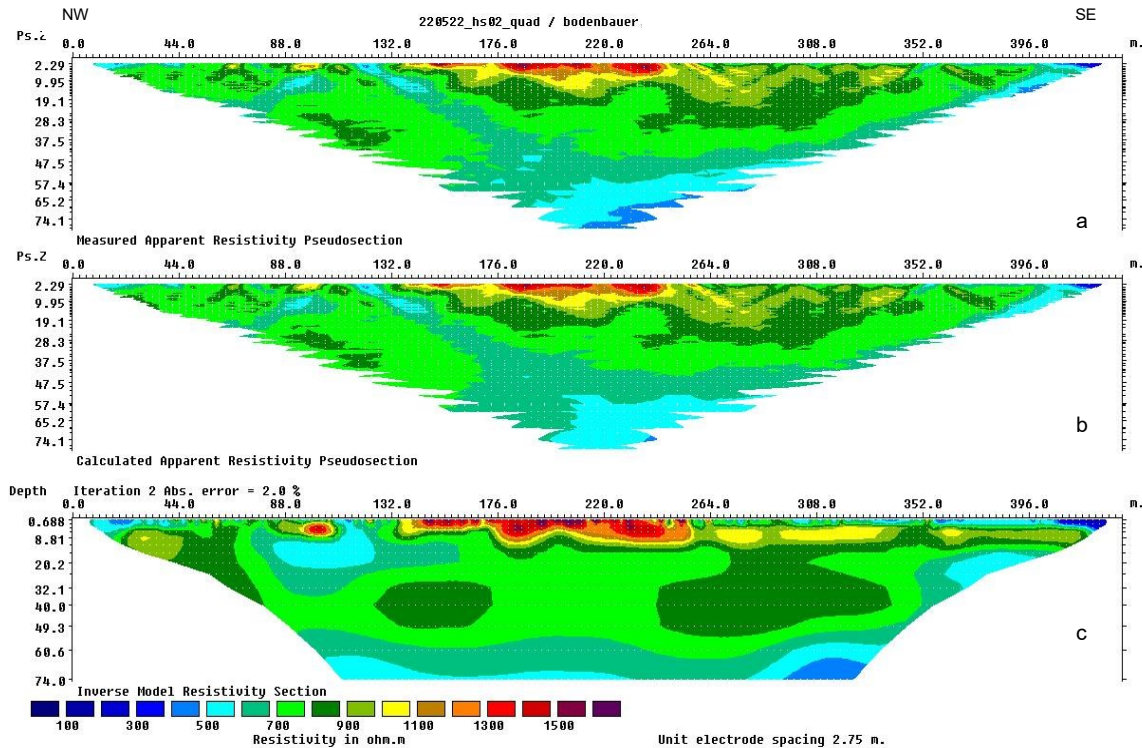


Figure 63: The measured apparent resistivities (a) compared to the calculated apparent resistivities for the combination of the Dipole-Dipole array and the Pole-Dipole array of hs01. (c) The inversion result represents a geological model derived from the data sets.

15.5.5. Combination of Dipole-Dipole and Pole-Dipole for hs01

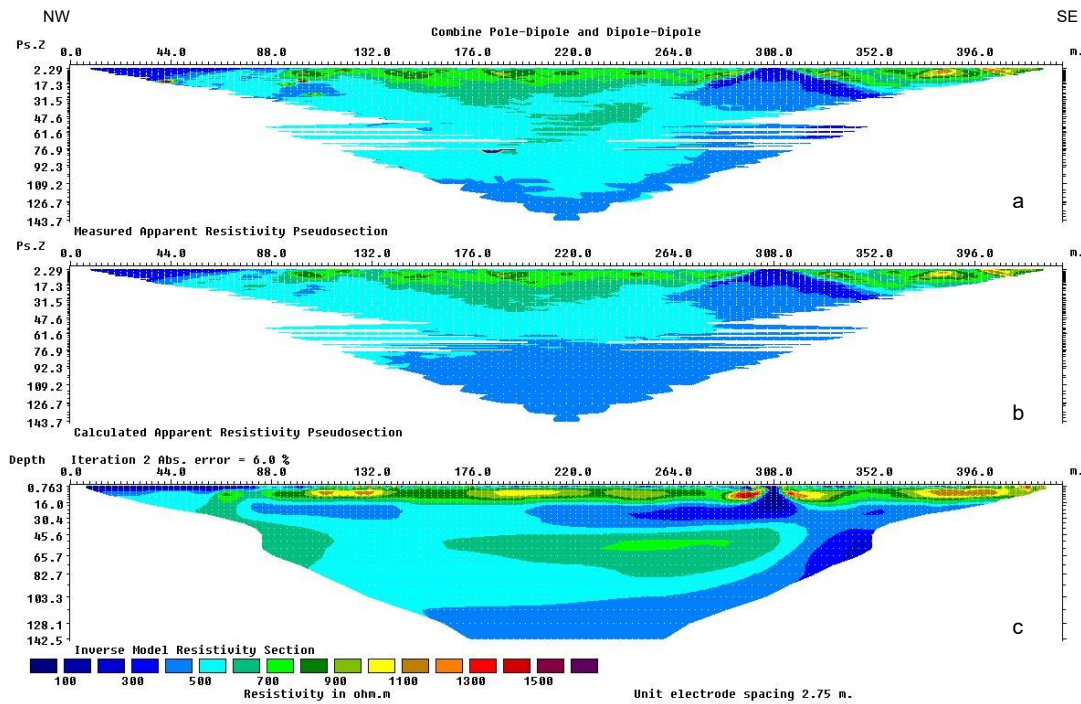


Figure 64: The measured apparent resistivities (a) compared to the calculated apparent resistivities for the Dipole-Dipole array of hs02. (c) The inversion result represents a geological model derived from the data sets.

15.5.6. Combination of Dipole-Dipole and Pole-Dipole for hs02

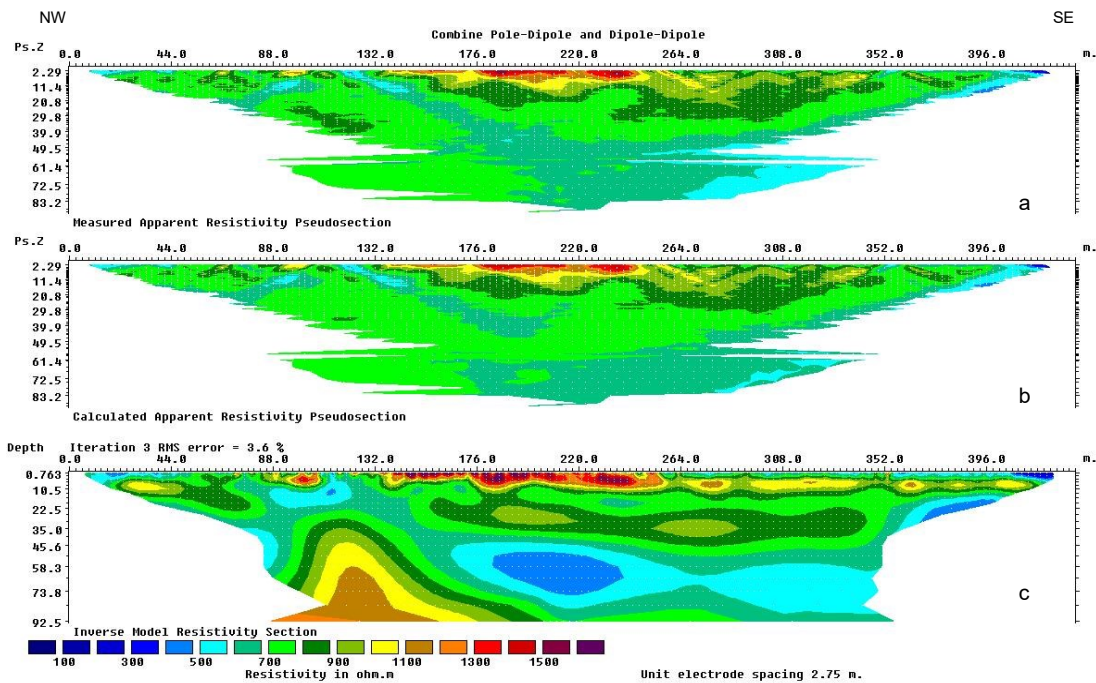


Figure 65: The measured apparent resistivities (a) compared to the calculated apparent resistivities for the combination of the Dipole-Dipole array and the Pole-Dipole array of hs02. (c) The inversion result represents a geological model derived from the data sets.